

EXPLORATIONS INTO THE INERTIAL AND
INTEGRAL SCALES OF HOMOGENEOUS
AXISYMMETRIC TURBULENCE

A Dissertation

Presented to the Faculty of the Graduate School
of Cornell University

in Partial Fulfillment of the Requirements for the Degree of
Doctor of Philosophy

by

Kelken Chang

January 2012

© 2012 Kelken Chang
ALL RIGHTS RESERVED

EXPLORATIONS INTO THE INERTIAL AND INTEGRAL SCALES OF HOMOGENEOUS AXISYMMETRIC TURBULENCE

Kelken Chang, Ph.D.

Cornell University 2012

A flow generator is described in which homogeneous axisymmetric turbulent air flows with varying and fully controllable degrees of anisotropy, including the much studied isotropic case, are generated by the combined agitations produced by 32 acoustic mixers focusing at the center of the system. The axisymmetric turbulence in a central volume of the size of the inertial scale is shown to have negligible mean and shear. The Taylor Reynolds number is about 480.

The influence of large scale anisotropy on the turbulence is examined from three aspects, namely the velocity structure functions, the velocity correlation functions, and the integral lengths. The directional dependence of two different second order transverse structure functions, in which one of them has separations stretched along the axis of symmetry of the turbulence and the other one normal to it, is studied. It is shown that the inertial range scaling exponents, determined using the extended-self-similarity procedure, and the Kolmogorov constants of the two structure functions are unaffected by the direction in which the structure functions are measured.

As an extension, because of its relevance to the study of intermittency, the directional dependence of transverse structure functions of the fourth to the sixth order is studied. Despite some issues with measurement noise and statistical convergence, some indications are found that anisotropy in the velocity field

intensifies the asymmetry of the probability density of the velocity increments. In addition, some evidence is found that the inertial range scaling exponents of the fourth, fifth, and sixth order are independent of the anisotropy.

Finally, it is found that, except in the isotropic case, the second order transverse velocity correlation functions deviate from each other at the large scale with increasing anisotropy. A self-similarity argument similar to one found in the study of critical phenomena is proposed. It is shown that the argument leads to a power-law relationship between the large scale velocity fluctuation and the correlation length, with an exponent that depends on the inertial range scaling exponent of the turbulence. The data collapse predicted by the self-similarity hypothesis is verified. It is demonstrated that the value of the power-law exponent is consistent with the value of the inertial range scaling exponent.

BIOGRAPHICAL SKETCH

Kelken Chang was born in Muar, Malaysia in September, 1978, the fourth child of five of Chia-Ming and Kim-Leu Chang. Chia-Ming Chang was a laboratory technician who was working in the Lee Rubber Company in Medan, Indonesia at the time his second son was born. In fact the original family name had been Teo, the family being ethnic Chinese from Fujian, China, but Chia-Ming Teo had changed his name to Chia-Ming Chang in 1965 when he took up Singaporean citizenship. Kelken's mother was the fifth child of eight of a well-to-do Chinese trader and she was ten years younger than her husband. Kelken was educated at Muar High School, a former Government English School established in 1902 by the British government during the colonization period. He went on to tertiary education at the National University of Singapore (NUS) and earned a Bachelor of Science degree in Physics with first class honors in 2003. He spent the first half of his graduate career at Cornell in Ithaca, New York, from 2003 to 2006, and afterwards at the Max-Planck-Institut für Dynamik und Selbstorganisation in Göttingen, Germany. In his spare time, he enjoys swimming in the lakes, reading poetry, and if he finds a good victim, playing practical jokes.

To my family and friends.

ACKNOWLEDGEMENTS

Many outstanding individuals have made my graduate experience one of the highlights of my life so far. I thank my advisor Eberhard Bodenschatz, the intrepid explorer whose undiminishable energy and contagious enthusiasm for science has provided much of the impetus for this dissertation. Eberhard provided me the freedom to grow as an independent thinker. He is also very kind and understanding when experiments did not go as well as planned.

I am beholden to my co-worker Greg Bewley for sharing with me his technical expertise and numerous invaluable ideas. His work attitude is very instructive and decisive every time in pushing the project a step forward. I appreciate the patience and rigor shown by both Greg and Eberhard in weeding out the waffle of my thoughts.

I am grateful to Erich Mueller and Itai Cohen for agreeing to sit on my special committee and for providing the many levels of administrative support throughout the entire stage of my studies. Outside of classroom, Erich has taught me the value of scientific collaboration, a value that has also been reprised by many Cornell professors. I thank David Cassel, Veit Elser, Henry Tye, and Michelle Wang for the advice they have given me at various stages of my graduate studies.

I am indebted to Sned for teaching me the rudiments of machining and for running a superb student machine shop; Andreas Kopp, Dr. Artur Kubitzek, Ortwin Kurre, Gerhard Nolte, and Andreas Renner for their invaluable technical assistance; Angela Meister for her meticulous handling of administrative issues at the institute; and Katharina Schneider for understandingly hearing out my many grouses – our daily banter at the lunch table has been a bulwark against the monotony of laboratory work.

I owe a debt of gratitude to my inspiring office mates from Cornell: Albert, Amgad, Dario, and Haitao; and from the Max Planck Institute for Dynamics and Self-Organization: Azam, Christian, Eva, Ewe Wei, Fabio, Gabriel A., Gabriel S., Haitao, Hengdong, Holger, Jens, Marco, Mathieu, Matthias, Mireia, Noriko, Robert, Shinji, Stephan, Toni, Vladimir, and Walter. Foremost among them, I wish to express my gratitude to Mathieu Gibert for graciously making his apartment available at critical stages of the writing of this thesis. I enjoyed the genuine camaraderie of these wonderful individuals, with whom I have had some of the most engaging conversations, sometimes discussing far into the night in some pub in Göttingen and finally thinking that we had solved our respective problems with alcoholically induced elation.

I have received financial support from the National Science Foundation, through grants PHY-9988755 and PHY-0216406, for my studies at Cornell and from the Max Planck Society and Deutsche Forschungsgemeinschaft (German Science Foundation), through the grant XU91/3-1, for my studies in Göttingen, Germany.

I thank my family for their unfaltering support that has carried me through the ups and downs of graduate school, and my friends for riding with me through thick and thin wood.

TABLE OF CONTENTS

Biographical Sketch	iii
Dedication	iv
Acknowledgements	v
Table of Contents	vii
List of Tables	ix
List of Figures	xii
1 Introduction	1
1.1 Kolmogorov theory	2
1.2 Verification of Kolmogorov theory	12
1.3 Relation to other inertial-range constants	19
1.4 Higher-order structure functions	23
1.5 Anomalous transverse scaling exponents	26
1.6 Anisotropic turbulence	31
1.7 Overview	36
2 The flow apparatus and the measurement technique	38
2.1 The flow apparatus	38
2.1.1 The chamber	38
2.1.2 The loudspeaker	41
2.1.3 The driving algorithm	44
2.1.4 The distribution of amplitudes	48
2.1.5 The amplifier	50
2.2 Laser Doppler Velocimetry	50
2.2.1 The Doppler model	54
2.2.2 The fringe model	56
2.2.3 The Bragg cell	58
2.2.4 Data processing	61
2.2.5 Limitations of the LDV technique	65
3 The experimental procedure	69
3.1 The coordinate system	69
3.2 The measurement protocol	72
3.3 Methods	73
4 The flows	74
4.1 Anisotropy of the fluctuations	74
4.2 Axisymmetry of the fluctuations	75
4.3 Homogeneity of the fluctuations	79
4.4 Anisotropy of the mean flow	81
4.5 Reflectional symmetry	81
4.6 Reynolds shear stresses	84
4.7 Conclusions	87

5	Universality in the structure functions	89
5.1	Isotropy of the structure functions	89
5.2	Equality of transverse ESS scaling exponents	91
5.3	Scalar-valuedness of the Kolmogorov constant	97
5.4	Conclusions	104
6	Higher order statistics	105
6.1	Higher order structure functions	106
6.2	Kurtosis and hyperkurtosis of structure functions	113
6.3	Higher order scaling exponents	117
6.4	Anomalous scaling	118
6.5	Conclusions	121
7	The integral scales of turbulence	123
7.1	The integral scale and correlation function	124
7.2	Scaling and self-similarity	127
7.3	Integral length scaling	129
7.4	Correlation functions collapse	137
7.5	Conclusions	137
8	Summary and Outlook	139
A	Evaluating the dimensionless integral A_γ	142
B	Statistical tools	145
C	Generating exponentially correlated colored noise	147
D	Calculating statistics with inter-arrival time weighting	149
E	Resampling LDV velocity signals	151
F	Calculating velocity autocorrelation	153
G	Calculating least-squares fit coefficients	155
	Bibliography	158

LIST OF TABLES

1.1	The inertial range scaling exponents of the longitudinal and transverse structure functions. The first two rows are the longitudinal scaling exponents, ζ_p^L , predicted by Kolmogorov (1941a) (see equation 1.49) and She and Leveque (1994) (see equation 1.54). The third and fourth rows show the longitudinal and transverse exponents measured by Dhruva et al. (1997) using the ESS method (see section 1.4) in atmospheric turbulence at R_λ between 10^4 and 1.5×10^4	27
1.2	The equality between longitudinal and transverse scaling exponents for sheared and unsheared turbulence and their trends with Reynolds number. The acronym TH denotes the use of Taylor’s hypothesis in the experiments.	29
1.3	The landscape of anisotropy for geophysical flows. Anisotropy refers to the ratio of streamwise to spanwise to vertical, streamwise to vertical, or zonal to meridional RMS velocity fluctuations, depending on the context. In Sullivan et al. (2000) the RMS velocity fluctuation data are unavailable. The anisotropy quoted is for the mean wind speed.	32
1.4	A bird’s eye view of the anisotropy observed in laboratory flows. The symbol d refers to distance between grid center lines, cylinder diameter, pipe diameter, jet nozzle diameter, tunnel width, jet width, or the boundary layer thickness, depending on the context. u'/v' refers to the ratio of streamwise to spanwise, vertical to horizontal, or radial to axial RMS velocity fluctuations, depending on the context. Shy et al. (1997) did not specify the Reynolds number, it is estimated from equation 1.7.	34
2.1	The chamber geometry and flow statistics from various speaker-driven flow chambers. The symbols from top to bottom are: energy dissipation rate (ϵ), Kolmogorov length scale (η), Kolmogorov time scale (τ_η), Taylor micro-scale Reynolds number (R_λ). For each study, only the case that gave the highest Reynolds number is reported.	43
4.1	For forcing anisotropy ratios (A) ranging from 0.33 to 2.5, the table shows the velocity fluctuation ratio according to the two limits discussed in the text (equations 4.1 and 4.2).	78

4.2	The table shows the turbulence parameters, for loudspeaker RMS amplitude ratios (A) ranging from 0.33 to 2.5. K is the turbulent kinetic energy, $\frac{1}{2}(u_z'^2 + 2u_{r_2}'^2)$, and $ U $ is $(U_z^2 + 2U_{r_2}^2)^{1/2}$. $\tilde{\tau}_{r_1r_2}$ and $\tilde{\tau}_{zr_2}$ are the average normalized Reynolds stresses measured along and normal to the axis of symmetry, respectively (see section 4.6). ϵ is the energy dissipation rate estimated according to the procedure prescribed in section 5.1. η and τ_η are the Kolmogorov length and time scales, respectively. λ is the Taylor length (see section 5.3) and R_λ is the Taylor scale Reynolds number. Data were collected at the center of the soccer ball when the axis of symmetry of the forcing is horizontal. Similar results (not shown) were obtained when the axis of symmetry is vertical.	88
5.1	The numerical data for radial scaling exponents ($\zeta_2^{(r)}$), axial scaling exponents ($\zeta_2^{(z)}$), and the ratio between the two.	95
5.2	The value of the scaling exponent of transverse second order structure functions, ζ_2 , measured using the ESS method for various laboratory flows.	95
5.3	The numerical data for the ratio of the Kolmogorov constant for transverse structure functions measured in nearly orthogonal directions, computed from averaging the ratio $D_{zz}(r_1)/D_{r_2r_2}(z)$ over a range of scales between 7 and 70 mm (second column), as well as from taking the ratio between the maxima of appropriately compensated structure functions, $\max(D_{zz}/r_1^{2/3})/\max(D_{r_2r_2}/z^{2/3})$ (fourth column). The values in the third and the last columns are the corresponding estimated error.	103
6.1	The numerical integral of the PDF and its moments from the second to the sixth order of an isotropically forced turbulent flow, shown in figure 6.4. The isotropy ratio was $u_z'/u_r' = 0.94$ and the Reynolds number was $R_\lambda = 480$ (see table 4.2).	107
6.2	The numerical integral of the PDF and its moments from the second to the sixth order of figure 6.5. The flow anisotropy was $u_z'/u_r' = 0.60$ at $R_\lambda = 536$ (see table 4.2).	113
6.3	The values of the fourth order radial and axial scaling exponents, $\zeta_4^{(r)}$ and $\zeta_4^{(z)}$, measured in our experiment using ESS. The last column shows the ratio between the two.	118
6.4	The numerical data for the fifth order radial and axial scaling exponents, $\zeta_5^{(r)}$, $\zeta_5^{(z)}$, and the ratio between the two.	118
6.5	The numerical data for the sixth order radial and axial scaling exponents, $\zeta_6^{(r)}$, $\zeta_6^{(z)}$, and the ratio between the two.	119

6.6	The inertial range transverse scaling exponents, ζ_p , measured in the current experiment using the ESS method and those measured by Shen and Warhaft (2002), denoted as S&W (2002) above, in an unsheared wind tunnel homogeneous and isotropic turbulent flow at two different R_λ of 134 and 863.	122
7.1	The numerical data for axial integral lengths (L_z), radial integral lengths (L_r), and the ratio between the two.	136

LIST OF FIGURES

1.1	The figure shows the range of eddy sizes ℓ from the largest (L_0) to the smallest (η) at very high Reynolds number. The meaning of each length scale is explained in the text.	7
1.2	The second-order longitudinal ($D_{11}(r)$) and transverse ($D_{22}(r)$ and $D_{33}(r)$) velocity structure functions measured in a turbulent boundary layer with $R_\lambda = 1450$. When compensated appropriately, the structure functions within the inertial range of scales are a measure of the value of the Kolmogorov constant. Reprinted with permission from Saddoughi and Veeravalli (1994): <i>J. Fluid Mech.</i> , 268:333-372, Copyright (1994) with permission from Cambridge University Press.	16
2.1	The ‘soccer ball’ chamber. Also shown is the layout of the Laser Doppler velocimetry probes in the experiment. A two-component probe aligned along the x_1 -axis measured the components of velocity in the x_2 and x_3 directions, and an additional one-component probe aligned along the x_2 axis measured velocities in the x_3 direction.	39
2.2	An overview of the experiment showing the ‘soccer ball’, the amplifier unit, and the measurement apparatus. The amplifier received signals from the multichannel high-speed voltage output device on the computer through a BNC connector block, and sent the signals to the loudspeaker array on the soccer ball. A laser Doppler velocimetry (LDV) system collected velocity signals and saved the data on a computer (not shown).	40
2.3	A loudspeaker with a conical nozzle.	42
2.4	(a) A 40-second time series of the voltage applied to the loudspeakers. (b) A part of the time series, zoomed in to reveal the 50 Hz carrier wave.	46
2.5	The spectrum of the voltage applied to the loudspeakers (a) before filtering and (b) after filtering. The solid line in (b) is proportional to a power law with an exponent of -2	47
2.6	A sketch showing the assignment of RMS amplitude for a given loudspeaker. The vector pointing from the center of a sphere, O , to the center of a loudspeaker, S_i , intersects an inscribed ellipsoid at E_i . The distance of E_i from the center of the sphere sets the RMS amplitude b_i for the given loudspeaker.	49
2.7	The figure shows (a) a truncated time series of one component of the fluid velocities in response to the forcing and (b) its spectrum calculated using the Lomb algorithm for unequally spaced data.	51
2.8	The Raveland amplifier.	52
2.9	The amplifier unit.	53

2.10	A schematic of a laser Doppler velocimeter.	54
2.11	The figure illustrates the change in received frequency caused by the motion of the particle in a single-beam scattering process. . .	54
2.12	The figure illustrates the dual-beam scattering process.	55
2.13	A schematic of a Bragg cell. A transducer generates an acoustic wave, resulting in a moving periodic refractive index grating that diffracts the incident light similar to in Bragg diffraction. The arrow points in the direction of travel of the acoustic wave. .	58
2.14	An overview of a TSI LDV system. Figure adapted from TSI LDV/PDPA system installation manual, page 73.	60
2.15	The effect of temporal binning on the value of the velocity correlation, $g(r)$, near zero separation. The values in the legend are the separations in millimeters.	63
2.16	The structure function as a function of temporal bin width. For legend, see previous figure.	63
2.17	The number of samples yielding the velocity correlation as a function of temporal bin width. For legend, see figure 2.15. . . .	64
2.18	The schematic shows the LDV probe volume dimensions.	68
3.1	The schematic shows the coordinate system in the laboratory frame. x_3 was aligned with the vertical. The axis of symmetry of the forcing lay along either x'_1 or x'_3 , depending on the configuration. Our measurements were made at points lay along x_1 . . .	70
3.2	The figure shows the orientations of the body coordinate system (in red) of the forcing (ellipsoidal surface in yellow) with respect to the laboratory frame (gray), and the conventions we used: (a) when the axis of symmetry of the forcing lay close to the x_3 axis of the laboratory frame, and (b) when the axis of symmetry lay close to x_1 axis of the laboratory frame. The coordinate system (x_1, x_2, x_3) was fixed in the laboratory frame, and the coordinate system (r_1, r_2, z) was fixed with respect to the symmetry of the forcing.	71
3.3	The figure shows the orientations of the measured velocity components with respect to the forcing coordinate system when the separation vector lay (a) along the axis of symmetry, or (b) perpendicular to the axis of symmetry.	72

4.1	The velocity fluctuation ratios as a function of the forcing anisotropy, A . The circular symbols (\circ) are $\sqrt{\langle u_z'^2(0) \rangle / \langle u_{r_1}'^2(0) \rangle}$ and the triangular symbols (\triangle) are $\sqrt{\langle u_z'^2(0) \rangle / \langle u_{r_2}'^2(0) \rangle}$. Symbols in the region shaded in blue have oblate shape asymmetry, whereas those in the region shaded in red have prolate shape asymmetry. Spherical symmetry lies at the intersection of the two regions. Data are collected with the axis of symmetry lying along x'_3 . We obtained similar results (not shown) when the axis of symmetry lay along x'_1	75
4.2	For three values of the anisotropy measured at the centre of the ball, $\sqrt{\langle u_z'^2(0) \rangle / \langle u_r'^2(0) \rangle}$, we plot (a) the ratio of the two radial components of the velocity fluctuations $\sqrt{\langle u_{r_2}'^2(0, 0, z) \rangle / \langle u_{r_1}'^2(0, 0, z) \rangle}$ and (b) the ratio of the axial fluctuations to the radial fluctuations, $\sqrt{\langle u_z'^2(r_1, 0, 0) \rangle / \langle u_{r_2}'^2(r_1, 0, 0) \rangle}$ at various points moving away from the center of the ball. The values in these legends, and in all others in this thesis, are those of the data in (b) for $r_1 = 0$	76
4.3	The comparison of fluctuations at various distances from the center of the soccer ball to those in the middle. (a) Radial fluctuations along axial separations, $\sqrt{\langle u_{r_2}'^2(0, 0, z) \rangle / \langle u_{r_2}'^2(0, 0, 0) \rangle}$, for anisotropy ratios, $\sqrt{\langle u_z'^2(0) \rangle / \langle u_r'^2(0) \rangle}$, ranging from 0.59 to 1.71. (b) Axial fluctuations along radial separations, $\sqrt{\langle u_z'^2(r_1, 0, 0) \rangle / \langle u_z'^2(0, 0, 0) \rangle}$, for the same range of anisotropy. The anisotropy ratios in the legend are measured at the center of the soccer ball.	80
4.4	The mean flow as a fraction of the fluctuating velocity (a) $\langle U_{r_2}(0, 0, z) \rangle / \sqrt{\langle u_{r_2}'^2(0, 0, z) \rangle}$, and (b) $\langle U_z(r_1, 0, 0) \rangle / \sqrt{\langle u_z'^2(r_1, 0, 0) \rangle}$ for axial-to-radial velocity fluctuation ratios ranging from 0.59 to 1.71. The values in the legend are the anisotropy measured at the centre of the soccer ball.	82
4.5	The cross correlations of orthogonal velocity components at various distances from the center of the soccer ball (a) along the axis of symmetry, and (b) along an axis perpendicular to the axis of symmetry of the forcing. The values in the color bar are the anisotropy measured at the center of the soccer ball for various values of the anisotropy of the forcing.	83
4.6	The figure shows the normalized Reynolds stress of orthogonal velocity components at various locations (a) along the axis of symmetry of the forcing, and (b) perpendicular to it. The values in the color bar are the anisotropy measured at the center of the soccer ball for various values of the anisotropy of the forcing.	86

5.1	The figure shows the (a) axial structure functions, $D_{r_2 r_2}(z)$, and (b) radial structure functions, $D_{zz}(r_1)$. In both cases, the structure functions are divided by the inertial range scaling predicted by Kolmogorov. The error bars are smaller than the symbols. The values in the legends are the anisotropy measured at the center of the soccer ball for various values of the anisotropy of the forcing.	90
5.2	The ratios between structure functions in different directions but in the same flow, $D_{zz}(r)/D_{r_2 r_2}(z)$, approach the isotropic value of one when the separation distance, $r_1 = z$, decreases. Results for data taken at other values of the large-scale anisotropy are consistent with those shown here. The values in the legends are the anisotropy measured at the center of the soccer ball.	91
5.3	The third-order structure functions with separations in the direction (a) along the axis of symmetry, and (b) perpendicular to the axis of symmetry. The values in the color bar are the anisotropy measured at the center of the soccer ball.	93
5.4	The third-order moments of the absolute values of the velocity increments with separations in the direction (a) along the axis of symmetry, and (b) perpendicular to the axis of symmetry. The dashed lines are proportional to a power law with exponent 1.17. The values in the color bar are the anisotropy measured at the center of the soccer ball.	94
5.5	The extended-self-similarity plots for the second-order transverse structure functions. The dashed lines are proportional to the power laws obtained from least squares fits to data. The values in the color bar are the anisotropy measured at the center of the soccer ball for various values of the anisotropy of the forcing. The error bars are smaller than the symbols.	96
5.6	The scaling exponents for the transverse structure functions measured using the extended-self-similarity method. The \circ symbols are the scaling exponents for $D_{r_2 r_2}(z)$ and the \square symbols are for $D_{zz}(r_1)$. The last two points in the radial data set have large uncertainties due to spatial resolution. They are marked in gray to show the general trend of the exponents.	97
5.7	The figure shows $\zeta_2^{(r)}/\zeta_2^{(z)}$, the ratio between the scaling exponents of the radial structure functions and those of the axial structure functions. The last two points with large uncertainties due to spatial resolution are marked in gray.	98

5.8	The figure shows the ratio between structure functions in different directions in the same flow, $D_{zz}(r_1)/D_{r_2r_2}(z)$, for all values of the anisotropy of the forcing. The data are the same as in figure 5.2. They are plotted separately to display individual trends. The two vertical dashed lines demarcate the range of scales between 7 and 70 mm where the compensated structure functions displayed a reasonable plateau. The values in the color bar are the fluctuations anisotropy measured at the center of the soccer ball for various values of the anisotropy of the forcing.	99
5.9	The compensated axial and radial transverse structure functions for all values of anisotropy. Only the data in the range of scales between 2 and 50 mm are used in the determination of the ratio of the Kolmogorov constant. Solid lines are the second-order, least-square, linear-log polynomial fits to the structure function data. Solid symbols are the maxima of the fitted curves. The error bars are smaller than the symbols. The values in the color bar are the anisotropy measured at the center of the soccer ball for various values of the anisotropy of the forcing.	101
5.10	The ratio between Kolmogorov constants measured in different directions $C_2^{(r)}/C_2^{(z)}$. The open circular symbols (\circ) are the ratio between the maximum values of the compensated radial and axial structure functions. The open square symbols (\square) are $\langle D_{zz}(r_1)/D_{r_2r_2}(z) \rangle$, the ratio of radial to axial structure functions averaged over a range of scales $7 < r < 70$ mm.	102
6.1	The extended-self-similarity plots for the fourth-order transverse structure functions. Dashed lines are proportional to power laws obtained from least squares fits to data. The values in the color bar are the anisotropy measured at the center of the soccer ball.	108
6.2	The extended-self-similarity plots for the fifth-order transverse structure functions. Dashed lines are proportional to power laws obtained from least squares fits to data. For legend, see figure 6.1.	109
6.3	The extended-self-similarity plots for the sixth-order transverse structure functions. Dashed lines are proportional to power laws obtained from least squares fits to data. For legend, see figure 6.1.	110
6.4	The probability density of velocity increments, $\delta u_{r_2}(z)$, and their moments for an inertial range separation $z/\eta \approx 130$ and spherically symmetric forcing, $u'_z/u'_r = 0.94$, at $R_\lambda = 480$ (see table 4.2). Here $x = \delta u_{r_2}(z)/\langle \delta u_{r_2}(z) ^2 \rangle^{1/2}$	111
6.5	The probability density of velocity increments, $\delta u_{r_2}(z)$, and their moments for an inertial range separation $z/\eta \approx 130$ and oblate shape forcing, $u'_z/u'_r = 0.60$, at $R_\lambda = 536$ (see table 4.2). Here $x = \delta u_{r_2}(z)/\langle \delta u_{r_2}(z) ^2 \rangle^{1/2}$	112

6.6	The kurtoses as a function of separations. (a) The axial kurtoses, $K_4(z) = \langle \delta u_{r_2}(z) ^4 \rangle / \langle \delta u_{r_2}(z) ^2 \rangle^2$, and (b) the radial kurtoses $K_4(r_1) = \langle \delta u_z(r_1) ^4 \rangle / \langle \delta u_z(r_1) ^2 \rangle^2$. The dashed lines are at the gaussian value of 3. The values in the color bar are the anisotropy measured at the center of the soccer ball. Error bars (not shown) are smaller than the symbols.	115
6.7	The hyper-kurtoses as a function of separations. (a) shows $K_6(z) = \langle \delta u_{r_2}(z) ^6 \rangle / \langle \delta u_{r_2}(z) ^2 \rangle^3$ and (b) shows $K_6(r_1) = \langle \delta u_z(r_1) ^6 \rangle / \langle \delta u_z(r_1) ^2 \rangle^3$. The dashed lines are at the gaussian value of 15. The values in the color bar are the anisotropy measured at the center of the soccer ball. Error bars (not shown) are smaller than the symbols.	116
6.8	The figure shows $\zeta_4^{(r)} / \zeta_4^{(z)}$, the ratio between the fourth-order scaling exponents of the radial structure functions and those of the axial structure functions. The last two points with large uncertainties due to spatial resolution are marked in gray.	119
6.9	The figure shows $\zeta_5^{(r)} / \zeta_5^{(z)}$, the ratio between the fifth-order scaling exponents of the radial structure functions and those of the axial structure functions. The last two points with large uncertainties due to spatial resolution are marked in gray.	120
6.10	The circular symbols (\circ) are our measurements of the inertial range scaling exponents, ζ_p , of the transverse structure functions using ESS method. The triangular symbols (\triangle) are the exponents measured by Shen and Warhaft (2002) in an unsheared wind tunnel homogeneous and isotropic turbulent flow at an R_λ of 134, and the square symbols (\square) are those measured by them at an R_λ of 863. The dashed line is the Kolmogorov prediction (equation 1.49). The solid line is the She-Leveque prediction (equation 1.54).	121
7.1	The figure shows the 8 pairs of transverse correlation functions obtained in 8 different flows with varying degree of large scale anisotropy. Circles (\circ) are for $g_{r_2 r_2}(z)$ and crosses (\times) are $g_{zz}(r_1)$. The error bars are smaller than the symbols. The values in the color bar are the fluctuations anisotropy measured at the center of the soccer ball for various values of the anisotropy of the forcing.	130
7.2	The extrapolation of the partially measured correlation function. The blue circular symbols (\circ) are the experimental data. The dashed line is the exponential extrapolated from the data. The area in the region shaded in blue is numerically integrated and the area in the region shaded in pink is analytically calculated. The sum of the two yields the integral length.	133

7.3	The sum of squares of residuals in the determination of x_{\max} that yields the exponential from a least squares fit of an exponential tail to the correlation function data.	134
7.4	The variation in the value of the exponent with the maximum separation in the least squares fit of exponential tails to the data.	135
7.5	The main figure shows the ratio of integral scales, L_z/L_r , as a function of the anisotropy in the fluctuating velocities, u'_z/u'_r . The solid line is the least squares fit to the data and the dashed line is the power law with exponent -3 predicted by the Kolmogorov inertial range scaling argument. The inset shows the same data on a logarithmic scale. The straight line in the inset has a slope of -2.56	136
7.6	The figure shows the same correlation functions from figure 7.1 plotted against the reduced variables, $r_1 u_z'^{-2/\zeta}$ and $z u_{r_2}'^{-2/\zeta}$. Here, $\zeta = 0.73$. Circles (\circ) are for $g_{r_2 r_2}(z)$ and crosses (\times) are for $g_{zz}(r_1)$. The values in the color bar are the fluctuations anisotropy measured at the center of the soccer ball.	138
A.1	Contour for the integral A.5. The pole at zero has been avoided by following the small circular quadrant near the origin. The integrals over the two circular quadrants tend to zero as $R \rightarrow \infty$ and $\delta \rightarrow 0$. Only the integrals over the line segments contribute to the integral A.5.	143

CHAPTER 1

INTRODUCTION

Homogeneous and axisymmetric turbulence, a simple and unique class of anisotropic turbulence, has eluded detailed investigations due to the lack of theoretical descriptions and flow generators whose large scale forcing can be tuned systematically. The intent of the present experimental study is to expound on some ideas for making quantitative measurements of homogeneous and axisymmetric turbulent flows, in hopes that a better way of characterizing such a flow may be found in the future. In his valuable review article on experimental methods in turbulence research for the *Handbuch der Physik*, Corrsin (1963b) states that

As in other areas of science, the goals of experiment are, loosely, of two kinds, *a)* exploratory and *b)* to confirm or disprove theories. The former puts a premium on imagination, with accuracy often secondary; the latter requires accuracies at least sufficient to distinguish among competing theories. In exploratory measurements of statistical properties of turbulent flows 20% accuracy is sometimes satisfactory. The more permanent crucial data, especially where signal-to-noise ratio is large, are taken with perhaps 2 to 10% uncertainty.

It is in this spirit that we would like to invite the reader to join in our exploration of this fascinating field of anisotropic turbulence. As a prelude to the experimental study, let us begin with a short theoretical description of turbulence.

1.1 Kolmogorov theory

The equation of motion of an unforced incompressible fluid, the Navier-Stokes equation (in nondimensional form)

$$\frac{\partial \mathbf{u}}{\partial t} + \mathbf{u} \cdot \nabla \mathbf{u} = -\nabla p + \frac{1}{\text{Re}} \nabla^2 \mathbf{u}, \quad (1.1)$$

is a nonlinear partial differential equation. Here, $\mathbf{u}(\mathbf{x}, t)$ and $p(\mathbf{x}, t)$ are the dimensionless fluid velocity and pressure, respectively, which are functions of space, \mathbf{x} , and time, t . The dimensionless parameter Re is the Reynolds number. Suppose the fluid has a well-defined characteristic length scale, \mathcal{L} , and a characteristic velocity scale, \mathcal{U} , the Reynolds number is defined as

$$\text{Re} = \frac{\mathcal{U} \mathcal{L}}{\nu}, \quad (1.2)$$

where ν is the kinematic viscosity of the fluid. At low Reynolds numbers, the inertial forces (the terms on the left hand side of the equation of motion) are negligible and solutions to the Navier-Stokes equation exist. The flows are smooth and laminar, like honey flowing down a plate. At high Reynolds numbers, the flows become turbulent and no analytical solution satisfying realistic boundary and initial conditions has yet been found. A complete process in solving a physical problem usually involves finding the right governing equations, followed by finding the solutions to these equations. In turbulence, we have only the equations and the solutions are still missing. Nelkin (1992), Warhaft (2002), and chapter 41 of Feynman et al. (1963) give concise introductions to the turbulence problem. For a slightly idiosyncratic review of the milestones of turbulence, the reader could refer to Lumley and Yaglom (2001).

For simplicity, research in turbulence has focused on idealized turbulent flows detached from the influence of externally imposed boundary. As a re-

sult, there are no apparent velocity and length scales with which one could use to define the Reynolds number. For this reason, the Reynolds number is constructed from the statistics of the turbulence. The characteristic velocity scale is taken as the root-mean-square (RMS) of the velocity fluctuations

$$u' = \left[\frac{1}{3} \sum_{i=1}^3 u_i^2 \right]^{1/2}, \quad (1.3)$$

and the characteristic length scale is taken as the integral length, L , which is the integral of the velocity autocorrelation function (see section 7.1). This yields a Reynolds number

$$\text{Re}_L = \frac{u' L}{\nu}, \quad (1.4)$$

intrinsic to the turbulence and independent of the external geometry of the flow. More frequently, the Taylor scale Reynolds number (Taylor, 1935)

$$R_\lambda = \frac{u' \lambda}{\nu}, \quad (1.5)$$

based on a different intrinsic length scale is chosen to describe the turbulence level. The Taylor scale, λ , is the separation at which the parabolic expansion of the velocity autocorrelation function near the origin becomes zero, and, in the case of isotropic turbulence (to be described shortly), is given by (Taylor, 1935)

$$\lambda = \sqrt{\frac{15 \nu u'^2}{\epsilon}}, \quad (1.6)$$

where ϵ is the energy dissipation rate per unit mass of the fluid. The Taylor scale Reynolds number is related to Re_L by (Taylor, 1935)

$$R_\lambda \approx (15 \text{Re}_L)^{1/2}. \quad (1.7)$$

It is routinely employed in the literature and is useful for comparison to the plethora of theoretical, numerical, and experimental results.

Taking the divergence of equation 1.1 and using the incompressibility condition, $\nabla \cdot \mathbf{u} = 0$, yields a Poisson equation for the pressure field

$$\nabla^2 p = -\nabla \cdot (\mathbf{u} \cdot \nabla) \mathbf{u}. \quad (1.8)$$

Equation 1.8 shows two features of the pressure field. Firstly, the pressure term in the Navier-Stokes equation is a nonlinear term of the same order as the advective term, $(\mathbf{u} \cdot \nabla) \mathbf{u}$. Secondly, the pressure at a given point is determined by the velocity field everywhere in space at the same time. Equation 1.8 thus highlights the crux of the turbulence problem – the Navier-Stokes equation is nonlinear, spatially nonlocal, and contains no small parameter in the theory (Warhaft, 2002). Any small perturbative expansion around the linear part of the equation will be amplified by the nonlinear terms and eventually diverge.

To make progress, we turn away from the equation of motion and construct phenomenological models based on physical assumptions. A recurring theme in many branches of physics is the search for universality. Physical systems exhibiting universality display macroscopic phenomena that are independent of the microscopic details of the systems. The emergence of simple continuum laws, like the Navier-Stokes equation, from complex underlying microscopic interactions would not have been possible had the fluid motions depended in great detail on the atomic interactions in the fluid molecules. In turbulence, there is an additional layer to the universality of the physical phenomena we are seeking. The universality must not only be unaffected by the quantum-mechanical properties of the fluid, but it must also be impervious to the influence of the initial and boundary conditions of the flow. This is the vision of the forerunners of turbulence theorists (see Taylor, 1935; Kolmogorov, 1941a; Prandtl, 1945; Heisenberg, 1948; Weizsäcker, 1948; Onsager, 1949). These related works, built upon Richardson's idea of the energy cascade (Richardson,

1922), consider localized turbulent motions (eddies) as the putative mediators of energy. Turbulence is viewed as a hierarchy of eddies spanning over a wide range of length scales. Each eddy of size ℓ has a characteristic velocity $u(\ell)$ and timescale $\tau(\ell)$. Larger eddies may contain smaller eddies. The largest eddies, of typical size L_0 , are vigorously created by the forcing mechanisms of turbulence. Feeding on the energy they received from the forcing, they become unstable and break up into successively smaller unstable eddies. As the cascade proceeds, energy is being passed from the larger eddies to the smaller ones, until the effect of viscosity on eddies of a particular size becomes significant, and energy is dissipated as heat.

Kolmogorov (1941a), building on the foundation of statistically homogeneous isotropic turbulence laid down by Taylor (1935), is credited for quantifying Richardson's energy cascade and for introducing the concept of universality in turbulence. The tenets of homogeneous isotropic turbulence put forth by Kolmogorov (1941a) can be summarized as follows. The presentation has been abridged from Pope (2000).

- (a) For very high Reynolds number turbulent flows, the small-scale¹ turbulent motions are statistically isotropic.

This hypothesis is usually referred to as the postulate of local isotropy. A turbulent flow is locally isotropic if it is locally homogeneous and if it is invariant with respect to rotations and reflections of the coordinate axes.

- (b) The statistical properties of the small scales ($\ell \ll L_0$) is governed universally by the energy dissipation rate per unit mass, ϵ , and the fluid viscosity, ν .

¹In the language of turbulence, the term 'scale' is suggestive of a characteristic length scale for the size of an eddy.

The range of scales $\ell \ll L_0$ is known as the universal equilibrium range, see figure 1.1. The motion of eddies in the energy-containing range, $\ell \sim L_0$, is shaped by the initial and boundary conditions, and is therefore anisotropic and non-universal.

Kolmogorov gave a prescription for calculating the length, time, and velocity scales of the smallest eddies

$$\eta = \nu^{3/4} \epsilon^{-1/4}, \quad (1.9)$$

$$\tau_\eta = \nu^{1/2} \epsilon^{-1/2}, \quad (1.10)$$

$$u_\eta = \nu^{1/4} \epsilon^{1/4}. \quad (1.11)$$

They are appropriately referred to as the Kolmogorov length, time, and velocity scales. The Reynolds number formed by these scales $u_\eta \eta / \nu$ is unity, the smallness of which indicates that the motion of eddies at scales $\ell < \eta$ is laminar.

- (c) The statistical properties of those scales in the inertial range is determined by ϵ only.

The universal equilibrium range is split into the inertial range ($\eta \ll \ell \ll L_0$) and the dissipation range ($\ell < \eta$), see figure 1.1. Eddy motion in the inertial range is neither affected by molecular viscosity nor the forcing mechanism.

Recasting this hypothesis in the cascade picture, this means that the rate of energy input (ϵ) received by the largest eddies is equal to the rate of energy transferred in succession from the largest eddies to the smallest eddies. This rate, in turn, is equal to the energy dissipated by the smallest eddies. An implicit assumption in this premise is that ϵ is independent of ν . Experimental evidence for this assumption has been collected by

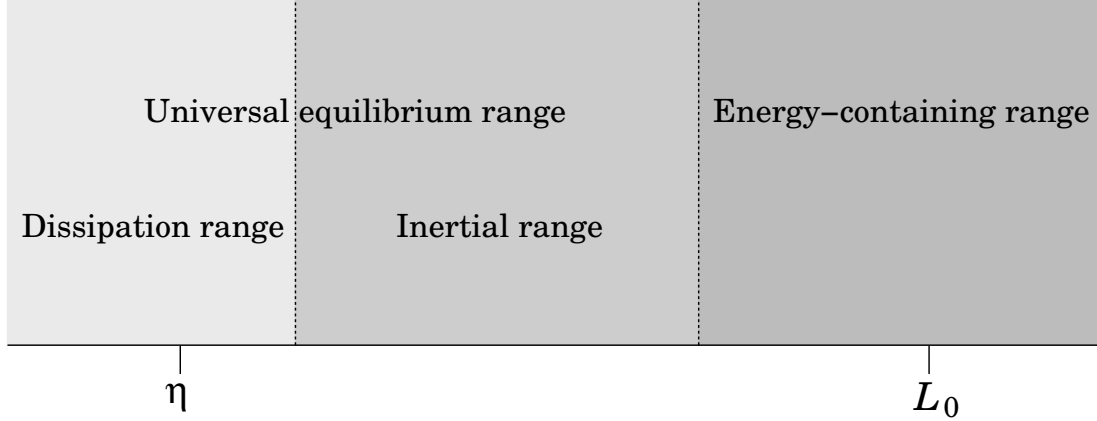


Figure 1.1: The figure shows the range of eddy sizes ℓ from the largest (L_0) to the smallest (η) at very high Reynolds number. The meaning of each length scale is explained in the text.

Sreenivasan (1984) and, more recently, by Pearson et al. (2002).

The validity of Kolmogorov's hypotheses is constantly under debate (e.g. Frisch, 1995). Its limitation to describing only theoretically ideal homogeneous and isotropic turbulence has not only very little relevance to anisotropic and non-infinite Reynolds number turbulence occurring in geophysical environment and in the laboratory, but the practical aspect of these hypotheses is also in question. For example, it is not clear to which statistical quantities they can be applied (see Nelkin, 1994). There is, however, considerable predictive power in them and a myriad of the existing work on turbulence rests on them. As an illustration, consider the second order velocity structure function

$$D_{ij}(\mathbf{r}) = \langle \delta u_i(\mathbf{r}, \mathbf{x}) \delta u_j(\mathbf{r}, \mathbf{x}) \rangle. \quad (1.12)$$

$\delta u_i(\mathbf{r}, \mathbf{x})$ is the velocity increment

$$\delta u_i(\mathbf{r}, \mathbf{x}) = u'_i(\mathbf{r} + \mathbf{x}) - u'_i(\mathbf{x}), \quad (1.13)$$

where u'_i is the fluctuation in the i -th velocity component. \mathbf{r} is the spatial increment and \mathbf{x} is an arbitrary reference point in space. The symbol $\langle \dots \rangle$ is an

ensemble average in theoretical analysis, and a time average in experiment. The commonly studied one-dimensional structure functions are the projections onto Cartesian \boldsymbol{r} -axes of $D_{ij}(\boldsymbol{r})$. These functions are important because they are experimentally measurable. For simplicity, the coordinate system is chosen such that the separation \boldsymbol{r} is in the x_1 direction. The two other mutually orthogonal directions x_2 and x_3 are then normal to \boldsymbol{r} . For homogeneous and isotropic turbulence, $D_{ij}(\boldsymbol{r})$ is related to the longitudinal structure function

$$D_{11}(r) = \langle (u'_1(r, 0, 0) - u'_1(0, 0, 0))^2 \rangle, \quad (1.14)$$

and the transverse structure functions

$$D_{22}(r) = \langle (u'_2(r, 0, 0) - u'_2(0, 0, 0))^2 \rangle, \quad (1.15)$$

$$D_{33}(r) = \langle (u'_3(r, 0, 0) - u'_3(0, 0, 0))^2 \rangle, \quad (1.16)$$

by the equation

$$D_{ij}(\boldsymbol{r}) = D_{22}(r) \delta_{ij} + [D_{11}(r) - D_{22}(r)] \frac{r_i r_j}{r^2}, \quad (1.17)$$

where $D_{22}(r) = D_{33}(r)$ by symmetry. See e.g. Pope (2000) for a derivation.

For an incompressible fluid, the transverse structure functions are related to the longitudinal structure function

$$D_{22}(r) = D_{33}(r) = \left(1 + \frac{r}{2} \frac{\partial}{\partial r}\right) D_{11}(r), \quad (1.18)$$

so that only one scalar function, either $D_{11}(r)$ or $D_{22}(r)$, is needed for describing structure functions with distances measured along arbitrary direction.

In the inertial range, $\eta \ll r \ll L_0$, an application of dimensional analysis and the universality hypothesis leads to the scaling for the structure functions

at sufficiently high Reynolds numbers (Kolmogorov, 1941a)

$$D_{11}(r) = C_2 (\epsilon r)^{2/3}, \quad (1.19)$$

$$D_{22}(r) = D_{33}(r) = \frac{4}{3} C_2 (\epsilon r)^{2/3}, \quad (1.20)$$

where C_2 is presumed to be a universal scaling constant, known as the Kolmogorov constant. These power laws are the first nontrivial predictions of Kolmogorov's theory². (See, however, Frisch (1995), chapter 6, for a modern derivation assuming only the symmetries of the Navier-Stokes equation, i.e. time and space invariances, rotational invariance, Galilean invariance, and scale invariance.)

The power-law behavior (equations 1.19 and 1.20) has its Fourier space counterpart. This can be seen by applying the Wiener-Khinchin theorem (e.g. equation 4.52 of Frisch (1995)), which states that the correlation function

$$R_{ij}(\mathbf{r}) = \langle u'_i(\mathbf{r} + \mathbf{x}) u'_j(\mathbf{x}) \rangle, \quad (1.21)$$

and the three-dimensional velocity spectrum tensor

$$\Phi_{ij}(\mathbf{k}) = \langle \tilde{u}_i(\mathbf{k}) \tilde{u}_j^*(\mathbf{k}) \rangle, \quad (1.22)$$

are Fourier transforms of each other

$$R_{ij}(\mathbf{r}) = \oint d\mathbf{k} \Phi_{ij}(\mathbf{k}) e^{i\mathbf{k} \cdot \mathbf{r}}, \quad (1.23)$$

$$\Phi_{ij}(\mathbf{k}) = \frac{1}{(2\pi)^3} \oint d\mathbf{r} R_{ij}(\mathbf{r}) e^{-i\mathbf{k} \cdot \mathbf{r}}. \quad (1.24)$$

Here, the Fourier representation of $\tilde{u}_i(\mathbf{k})$ was introduced to turbulence theory by Heisenberg (1948) and it is written as

$$\tilde{u}_i(\mathbf{k}) = \frac{1}{(2\pi)^3} \oint d\mathbf{r} u'_i(\mathbf{r}) e^{-i\mathbf{k} \cdot \mathbf{r}}. \quad (1.25)$$

²An experimental discovery of the law of pair dispersion by Richardson (1926) predates Kolmogorov's theoretical discovery.

The asterisk in $\tilde{u}_i^*(\mathbf{k})$ denotes complex conjugate and reality of $u'_i(\mathbf{r})$ implies $\tilde{u}_i^*(\mathbf{k}) = \tilde{u}_i(-\mathbf{k})$.

Just as with the structure function $D_{ij}(r)$, $\Phi_{ij}(\mathbf{k})$ is usually projected onto Cartesian \mathbf{k} -axes to yield the experimentally accessible one-dimensional spectra

$$E_{ij}(k_1) = 2 \int_{-\infty}^{\infty} dk_2 \int_{-\infty}^{\infty} dk_3 \Phi_{ij}(\mathbf{k}). \quad (1.26)$$

Using the Wiener-Khinchin theorem, Taylor (1938) showed that the one-dimensional spectra and the correlation functions form a Fourier transform pair

$$E_{ij}(k_1) = \frac{1}{\pi} \int_{-\infty}^{\infty} R_{ij}(r) e^{-ik_1 r} dr \quad (1.27)$$

$$R_{ij}(r) = \frac{1}{2} \int_{-\infty}^{\infty} E_{ij}(k_1) e^{ik_1 r} dk_1. \quad (1.28)$$

In the above, \mathbf{r} is taken as $r \mathbf{e}_1$. The normalization factor is chosen so that when $r = 0$, equation 1.28 gives, for example when $i = j = 1$

$$R_{11}(0) = \langle u_1'^2 \rangle = \int_0^{\infty} E_{11}(k_1) dk_1. \quad (1.29)$$

Here, $E_{11}(k_1)$ is extended to negative frequencies by $E_{11}(-k_1) = E_{11}(k_1)$. If the turbulence is locally isotropic³, the correlation function $R_{ij}(r)$ is then linked to the structure function $D_{ij}(r)$ by

$$D_{ij}(r) = 2 (R_{ij}(0) - R_{ij}(r)), \quad (1.30)$$

which, when equation 1.28 is substituted into the above, yields

$$D_{ij}(r) = \int_{-\infty}^{\infty} (1 - e^{ik_1 r}) E_{ij}(k_1) dk_1. \quad (1.31)$$

In two short notes that predated his prediction for the structure function, Kolmogorov presented relevant mathematical description for turbulence energy

³If the turbulence is locally isotropic, then $\langle u'_i(\mathbf{r}) u'_j(\mathbf{r}) \rangle = \langle u'_i(0) u'_j(0) \rangle = R_{ij}(0)$, and also $R_{ij}(-\mathbf{r}) = R_{ij}(\mathbf{r})$

spectra and their connection to structure functions (see Kolmogorov, 1940a,b). He considered the case when the spectra follow a power law, taking the longitudinal case, $i = j = 1$, as an example

$$E_{11}(k_1) = B |k_1|^{-(\gamma+1)}, \quad (1.32)$$

where B is a positive constant. A substitution of the above into equation 1.31 with a change of variables, $x = k_1 r$, yields the following power law for the longitudinal structure function

$$D_{11}(r) = B A_\gamma |r|^\gamma, \quad (1.33)$$

with the dimensionless integral

$$A_\gamma = \int_{-\infty}^{\infty} (1 - e^{ix}) |x|^{-(\gamma+1)} dx. \quad (1.34)$$

Convergence of the structure function limits the value of γ to $0 < \gamma < 2$ (see e.g. page 90 of Monin and Yaglom (1975)), in which case the integral can be evaluated analytically to give (for a derivation, see appendix A)

$$A_\gamma = \frac{\pi}{\Gamma(\gamma + 1) \sin(\gamma \pi/2)}, \quad (0 < \gamma < 2). \quad (1.35)$$

Here, $\Gamma(x)$ is the gamma function. The conclusion to be drawn from this analysis is that if the spectrum exhibits a power-law behavior $E_{11}(k_1) = B |k_1|^{-(\gamma+1)}$, then there is a corresponding power-law behavior $D_{11}(r) = B A_\gamma |r|^\gamma$ for the structure function.

Kolmogorov (1941a) and Obukhov (1941a,b) made the first attempt at determining the spectral power-law exponent by assuming that the energy spectrum $E_{11}(k_1)$ has a universal form uniquely determined by the energy dissipation rate ϵ . A straightforward dimensional analysis yields

$$E_{11}(k_1) = C_k \epsilon^{2/3} k_1^{-5/3}, \quad (1.36)$$

where C_k is a dimensionless universal constant. It is related to the Kolmogorov constant, C_2 , through (equation 21.25 of Monin and Yaglom (1975))

$$\frac{C_2}{C_k} = A_{2/3} = \frac{3}{2} \Gamma\left(\frac{1}{3}\right) \approx 4. \quad (1.37)$$

Just as in the case with the transverse structure functions, the transverse spectra are also related to $E_{11}(k_1)$ through

$$E_{22}(k_1) = E_{33}(k_1) = \frac{1}{2} \left(1 - k_1 \frac{\partial}{\partial k_1}\right) E_{11}(k_1) = \frac{4}{3} C_k \epsilon^{2/3} k_1^{-5/3}. \quad (1.38)$$

Equations 1.36 and 1.38 are the famous one-dimensional Kolmogorov $-\frac{5}{3}$ spectra.

1.2 Verification of Kolmogorov theory

As a preliminary to the investigation of their angular dependence in chapter 5, we review, in the following, efforts made in establishing the exact value of the scaling exponents, the Kolmogorov constants, C_2 and C_k , and their Reynolds number trends.

Work on verification of the two-thirds law, equations 1.19 and 1.20, as well as estimation of C_2 , up to the early 1970s has been reviewed by Monin and Yaglom (1975) (see page 461). Kolmogorov made the first attempt to compare his theoretical prediction for the structure functions to the data obtained by Dryden et al. (1937) with hot-wire anemometry, in which Taylor's frozen-turbulence hypothesis (Taylor, 1938) has been invoked to surrogate temporal velocity fluctuations for spatial velocity fluctuations (see the sidebar Taylor's Hypothesis). The measurements were obtained from a wind tunnel grid turbulence, whose Reynolds numbers (R_λ) we estimated to be in the range from 15 to 140.

TAYLOR'S HYPOTHESIS: When studying a multiple-scale problem like turbulence, it is difficult to obtain an instantaneous snapshot of all the eddies formed within the turbulence. It is easier, and cheaper, to make measurements at one point over a long period of time. To study the turbulence from a continuous record of measurements from a single point, we need to assume that the advective velocity, $\langle U \rangle$, is uniform and the turbulence intensity, $u'/\langle U \rangle$, is low. In other words, the turbulence is frozen, or evolves on a time scale much larger than the advective one, so that the conversion from time to space, $x = \langle U \rangle t$, can be made. For a reference on Taylor's hypothesis, see Frisch (1995), page 58.

Kolmogorov suggested that $C_2 = 3/2$ (Kolmogorov, 1941b). (See Kolmogorov (1991) for an English translation of this work.) Shortly thereafter, a study carried out in the atmospheric surface layer by means of hot-wire anemometry was undertaken by Obukhov (1942), but the study was halted by World War II. Obukhov later resumed the study using the hot wire anemometer data of Gödecke (Obukhov, 1949a; Gödecke, 1935). Around the same time, many atmospheric surface layer studies employing hot wire anemometry were initiated in different parts of the world; for example Townsend (1948) in the UK; MacCready (1953) and Cramer (1959) in the USA; Shiotani (1955) in Japan; and Taylor (1955) in Australia; after Kolmogorov's work received significant exposure due to Batchelor (1946b, 1947). The 1970s saw the emergence of precise hot-wire measurements. Measurements of Van Atta and Chen (1970) in the atmospheric boundary layer over the ocean showed that both $r^{2/3}$ and $r^{0.722}$ power laws fit well to their second order structure functions data, and that the value of C_2 is 2.3 (error not reported). Comte-Bellot and Corrsin (1971) measured longitudinal

and transverse velocity autocorrelations but did not report on measurements of the structure functions. Anselmet et al. (1984) investigated structure functions up to the 18th order on the axis of turbulent jets, at R_λ ranging from 536 to 852, and in a turbulent duct flow, at $R_\lambda = 515$. They found that $C_2 = 2.2$ and $D_{11}(r) \sim r^{0.71}$ in the inertial range. An experimental study by Saddoughi and Veeravalli (1994), which later became a benchmark experiment in the field, was performed on the test-section ceiling of the 80×120 foot wind tunnel at NASA Ames Research Center. The flows are boundary layer flows at R_λ ranging from 500 to 1450. The Reynolds numbers achieved in this experiment are superior to those in many laboratory flows. It has only been surpassed by a few flows generated in high-Reynolds-number facilities, including the ONERA wind tunnel with $R_\lambda = 3374$ (e.g. Gledzer et al., 1996), the Princeton University turbulent pipe (e.g. Zagarola and Smits, 1998) with a R_λ of 2.3×10^4 (estimated from equation 1.7 where Re_L is based on the average velocity and the pipe diameter), and the wind tunnel of the Central Aerohydrodynamic Institute in Moscow, Russia, with a R_λ of 3200 (Praskovsky and Oncley, 1994). Saddoughi and Veeravalli (1994) observed approximately one decade of $r^{2/3}$ scaling (reproduced in figure 1.2). The value of the Kolmogorov constant reported is 2.0 ± 0.1 . Subsequent measurements of the Kolmogorov constant by Anfossi et al. (2000) in the atmospheric surface layer ($C_2 = 1.7$), Degrazia et al. (2008) and Welter et al. (2009) in the wind tunnel and atmospheric boundary layers ($C_2 = 2.47 \pm 0.30$) at R_λ in the range between 373 and 2×10^4 are marginally consistent with the value reported by Saddoughi and Veeravalli (1994). The discrepancy between the values of the Kolmogorov constant measured in the laboratory and in the atmosphere may arise due to the uncertainty in atmospheric flow conditions, for example variability of wind speed and direction. We note that measurements

from the controlled laboratory studies in Degrazia et al. (2008) and Welter et al. (2009) give $C_2 = 2.34 \pm 0.26$, in closer agreement with the value reported by Saddoughi and Veeravalli (1994).

Many of the past studies however, have been devoted to verifying the spectra (equations 1.36 and 1.38). Experimental studies prior to the early 1970s have been reviewed by Monin and Yaglom (1975) (see page 467), and subsequent studies up to the early 1990s have been extensively reviewed by Sreenivasan (1995). Data from numerical simulations have been collected by Yeung and Zhou (1997). We review in the following a few milestone experiments and supplement the list with several recent ones.

In a pioneering tidal-channel experiment at R_λ ranging from 3000 to 18000, Grant et al. (1962)⁴ observed more than two decades of $-5/3$ scaling and measured a value of 0.47 ± 0.02 for C_k from data obtained with hot-film anemometry, which uses the same principle as hot-wire anemometry but the probe is less likely to be contaminated by dirt in water⁵. The hot-wire measurements of Saddoughi and Veeravalli (1994) show slightly less than a decade of $-5/3$ scaling, and in that range, $C_k = 0.49$. The reduced scaling range in this study might be an effect of the Reynolds number; we note that their Reynolds number is an order of magnitude smaller than that of Grant et al. (1962). The data of over 100 spectra, mostly collected with hot-wire technique, from various geophysical and laboratory flows collected in Sreenivasan (1995) support a universal value of C_k , approximately 0.53 ± 0.055 , beyond R_λ of about 50, as can also be inferred from recent experiments of Welter et al. (2009). Similar conclusions can

⁴These estimates for the Reynolds numbers were obtained by Sreenivasan (1995). See the footnote therein for details.

⁵Kraichnan (1966) has analyzed the same data and observed that the estimate would be higher by more than 10% if one looked, instead, for flat region in plots of $\epsilon^{-2/3} k_1^{5/3} E_{11}(k_1)$ vs k_1 .

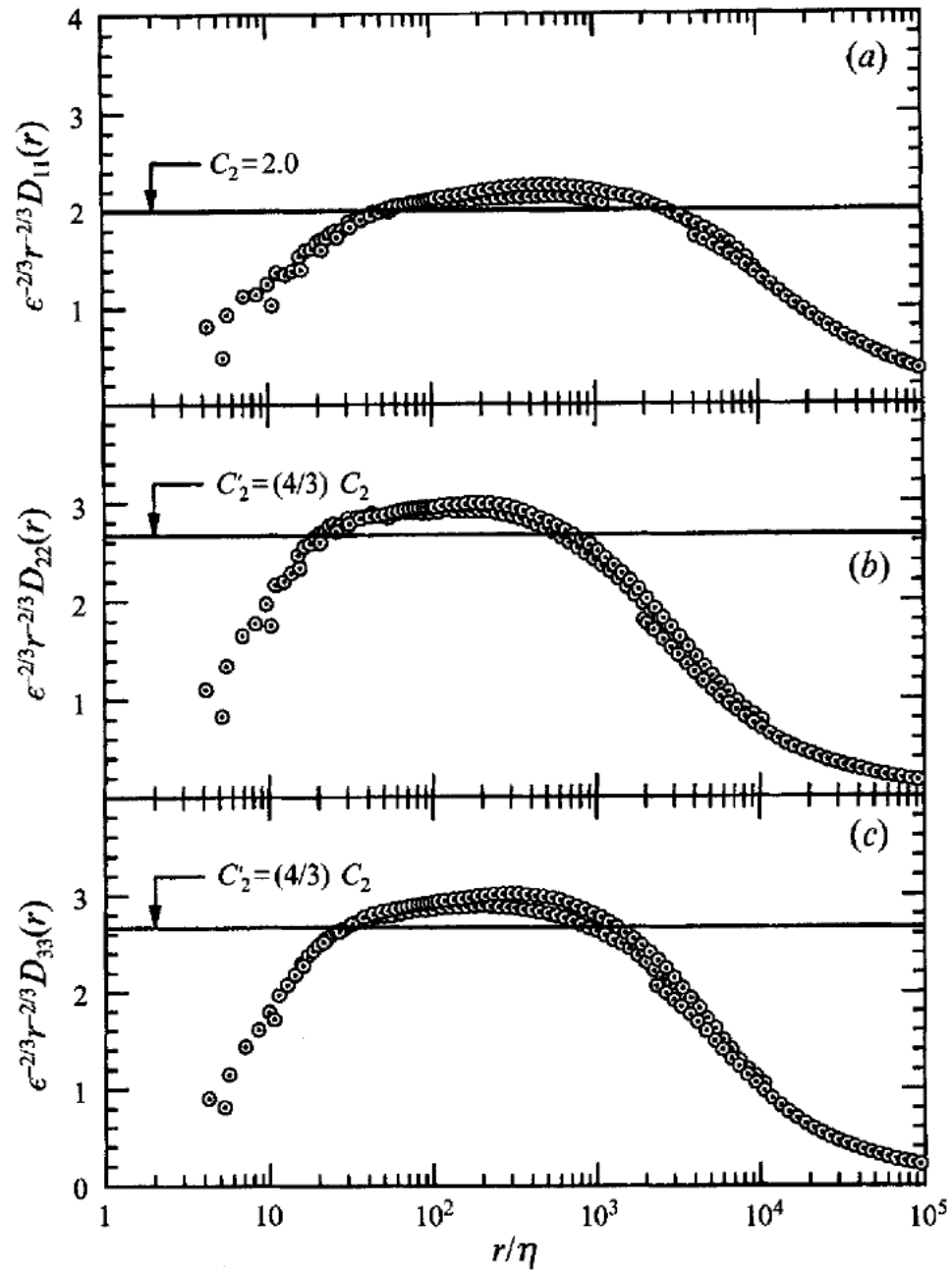


Figure 1.2: The second-order longitudinal ($D_{11}(r)$) and transverse ($D_{22}(r)$ and $D_{33}(r)$) velocity structure functions measured in a turbulent boundary layer with $R_\lambda = 1450$. When compensated appropriately, the structure functions within the inertial range of scales are a measure of the value of the Kolmogorov constant. Reprinted with permission from Saddoughi and Veeravalli (1994): *J. Fluid Mech.*, 268:333-372, Copyright (1994) with permission from Cambridge University Press.

be drawn from numerical simulation studies (e.g. Yeung and Zhou, 1997; Gotoh et al., 2002; Kaneda et al., 2003). On the other hand, these findings seem to be at odds with the outcome uncovered in a few experiments, which suggest C_k follows a power law of the form $C_k \propto R_\lambda^{-\mu}$. The value of the exponent, μ , is 0.094 ± 0.004 in the atmospheric surface layer (Praskovsky and Oncley, 1994), $2/3$ in a wind tunnel with specially designed active grid (Mydlarski and Warhaft, 1998), and 0.16 in a hydrodynamic simulation forced by Taylor-Green vortex (Mininni et al., 2008); whereas theory predicts $C_k \propto (\ln R_\lambda)^{-1}$ (Barenblatt and Goldenfeld, 1995).

These conflicts seem to have been resolved in a recent study by Donzis and Sreenivasan (2010). The apparent Reynolds-number dependence is ascribable to inconsistent procedures followed in the estimation of C_k . A typical procedure for estimating C_k is to plot the compensated spectrum, $\epsilon^{-2/3} k_1^{5/3} E_{11}(k_1)$, and seek a plateau, whose height in the inertial range is taken as C_k . This procedure is, however, complicated by the absence of a distinct plateau in the inertial range, and the existence of a spectral bump at the high-wavenumber end (the near-dissipation range), known as the bottleneck, whose effect is most prominent in the three-dimensional spectrum. The occurrence of the spectral bump was first captured in an analysis of Qian (1984). The physical mechanism leading to its appearance has been attempted by various workers (e.g. Yakhot and Zakharov, 1993; Falkovich, 1994; Martinez et al., 1997; Kurien et al., 2004; Verma and Donzis, 2007; Bershadskii, 2008; Frisch et al., 2008). Donzis and Sreenivasan (2010) showed that the height of this bump in the three-dimensional spectrum varies as $R_\lambda^{-0.04}$, while the height and the location of the local minimum preceding the bump remain practically constant. Donzis and Sreenivasan (2010) suggest evaluating C_k from the height of the local minimum before the bump,

as this leads to a Kolmogorov constant independent of R_λ . It remains for future investigations to elucidate the underlying mechanism of this operation.

Since the spectra are uniquely related to the structure functions, one may expect that the bottleneck effect in wavenumber space will have its physical space correspondence near the transition between the dissipation and the inertial ranges. Dobler et al. (2003) argued that localized features in wavenumber space will become sufficiently non-local in physical space that they are practically undetectable. Lohse and Müller-Groeling (1995), on the other hand, argued that a rapid transition between these ranges in the physical space is the manifestation of the spectral bump. The findings of Donzis and Sreenivasan (2010) confirm this belief. To assess the effect of the Reynolds number on the transition region, they studied the Batchelor interpolation formula (Batchelor, 1951)

$$\frac{D(r)}{u_\eta^2} = K \frac{(r/\eta)^2}{[1 + (c_B r/\eta)^q]^{(2-\zeta_2)/q}}, \quad (1.39)$$

with $K = 1/15$ for the longitudinal and $2/15$ for the transverse structure functions, u_η is the Kolmogorov velocity (see equation 1.11), and $\zeta_2 = 0.67$ is the inertial range scaling exponent. c_B and q are fit parameters. They found $c_B = 0.076$ and 0.102 for longitudinal and transverse structure functions, independent of R_λ , and the power laws $q \propto R_\lambda^{-1.06}$ and $q \propto R_\lambda^{-0.92}$ for the longitudinal and transverse structure functions, respectively. The decrease of q with R_λ confirms the belief that the transition at high Reynolds numbers is smoother, which is the manifestation of a flatter spectral bump. Such a subtle Reynolds number dependence is currently beyond the resolution limit of experiments and may have escaped definitive detection. Notwithstanding this subtle effect, at least the contamination by a 'physical' bump in the determination of C_2 can be obvi-

ated in the physical space⁶. Between the approach in spectral space and that in physical space, the approach in physical space remains the better one.

1.3 Relation to other inertial-range constants

The following discussion is intended to illustrate the interrelations between the Kolmogorov constant and the scaling constants of the Lagrangian structure functions, the Richardson-Obukhov constant for turbulent relative dispersion, and the Obukhov-Corrsin constant for passive scalar structure function. The scalar-valuedness of the Kolmogorov constant to be established in chapter 5 may be taken as a constraint on the angular dependence of the various constants.

It is often the case that analyzing the same physical problem from a different perspective may reveal unexpected results and advance our understanding of the problem. The structure functions introduced in the previous section are functions of separations fixed in space. Analyzing fluid motion at fixed spatial locations is known as the Eulerian description. To inspect the turbulence problem in a different way, researchers have devised the Lagrangian description, where an observer moves along with the flow (e.g. Toschi and Bodenschatz, 2009). The basic tools in the Lagrangian description of turbulence are the Lagrangian structure functions, defined as

$$D_p^L(\tau) = \langle \delta u_i(\tau) \delta u_j(\tau) \rangle, \quad (1.40)$$

where the velocity increments, $\delta u_i(\tau) = u'_i(t + \tau) - u'_i(t)$, are taken along the

⁶The typical procedure in physical space is to plot, for example, $(\epsilon r)^{-2/3} D_{11}(r)$ vs r and seek a plateau whose height is taken as the value of C_2 .

trajectory of an individual fluid particle.

Obukhov and Landau ⁷ applied Kolmogorov's theory to derive scaling forms for the Lagrangian velocity structure functions valid in the inertial range

$$\langle \delta u_i(\tau) \delta u_j(\tau) \rangle = C_0 \epsilon \tau \delta_{ij}, \quad (1.41)$$

where i is any Cartesian component x , y , or z ; ϵ is the energy dissipation rate per unit mass; and δ_{ij} is the Kronecker delta. See e.g. Monin and Yaglom (1975), page 358 for a derivation. The constant C_0 , presumed to be universal, is known as the Lagrangian velocity structure function constant. It is an important parameter in stochastic models of turbulent transport and dispersion (e.g. Rodean, 1991; Sawford, 1991; Weinman and Klimenko, 2000). Quality measurements of C_0 are scarce and its value is very uncertain, partly because Lagrangian experiments, where the trajectories of fluid particles are followed in both time and space (e.g. La Porta et al., 2000), have historically been very difficult. Reported values of C_0 range from 1.0 to 7.0 (Poggi et al., 2008). Inoue (1951) applied the Kolmogorov theory to the Lagrangian velocity spectrum $\phi_{ij}^L(\omega)$, defined as the Fourier transform of the Lagrangian velocity autocorrelation tensor, and obtained $\phi_{ij}(\omega) = B \epsilon \omega^{-2} \delta_{ij}$, where ω is the angular frequency. B and C_0 are simply related by $C_0/B = A_1 = \pi$, see e.g. Monin and Yaglom (1975), page 361. Under the assumption that the velocity fluctuations integrated from Eulerian and Lagrangian spectra are equal (Lumley, 1957, 1962), Corrsin (1963a) approximated the Eulerian and Lagrangian spectra by their inertial-range forms between appropriate wave number and frequency limits and obtained $B/C_k^{3/2} = \text{constant}$, where B is the scaling constant of the Lagrangian velocity spectrum. The same power law has recently been derived by Franzese

⁷The scaling form for the Lagrangian velocity structure function was independently obtained by Obukhov and Landau shortly after the publication of Kolmogorov's 1941 paper. See Monin and Yaglom (1975), page 359, for a historical account.

and Cassiani (2007) based on a statistical diffusion theory of relative dispersion of fluid particles.

The Lagrangian velocity structure function constant is, quite astonishingly, also related to the Richardson-Obukhov constant governing the turbulent relative dispersion from a point source in isotropic turbulence. Obukhov (1941b), refining the empirical finding of Richardson (1926), applied Kolmogorov's dimensional reasoning to the mean square separation distance between two particles $\langle \mathbf{r}^2(t) \rangle$ and derived an expression valid in the inertial range of scales

$$\langle \mathbf{r}^2(t) \rangle = g \epsilon t^3, \quad (1.42)$$

where ϵ is the energy dissipation rate. The scaling constant g is known as the Richardson-Obukhov constant. See e.g. Ouellette et al. (2006) for a modern derivation. Experimental and numerical studies seem to be converging on a value in the range $0.5 \leq g \leq 0.6$ (Salazar and Collins, 2009). The interest in the law of two-particle dispersion is immense because of its utility in describing transport and mixing processes in environmental and engineering problems. Several investigators (see Lin, 1960; Novikov, 1963; Ivanov and Stratonovich, 1963) exploited the assumption that the accelerations of fluid particles are uncorrelated at high Reynolds number to connect two-particle statistics with Lagrangian one-particle statistics. All their analyses yield the result $g = 2 C_0$. Borgas and Sawford (1991) showed that taking into account the two-particle acceleration correlation provides a value of g smaller than $2 C_0$. The recent work of Franzese and Cassiani (2007) based on a statistical diffusion theory of relative dispersion provides an estimate $g \approx C_0/11$.

The relative motion between particles is, remarkably, connected to the concentration profile of a substance, the so-called passive scalar. The substance

could be a contaminant, like smoke dispersing in air; it could also be odor, like the smell of perfume traveling in air; or heat, as in the case when a weakly heated object is cooled in the flow. In his seminal paper on turbulent relative dispersion, Richardson (1926) introduced the distance-neighbor function $q(\mathbf{r}, t)$, which is the equal-time probability density function for the separation \mathbf{r} between fluid particle pairs randomly chosen from a scalar field $\theta'(\mathbf{r}, t)$ passively advected by the turbulence. They are related by (e.g. Ott and Mann, 2000)

$$q(\mathbf{r}, t) = \int \langle \theta'(\mathbf{x}, t) \theta'(\mathbf{x} + \mathbf{r}, t) \rangle d\mathbf{x} . \quad (1.43)$$

Assuming homogeneity, isotropy, and stationarity, we also have by definition

$$\langle \mathbf{r}^2(t) \rangle = \int_0^\infty 4 \pi s^4 q(s, t) ds . \quad (1.44)$$

Equations 1.43 and 1.44 provide a formal link between the mean square separation distance between particle pairs and the autocorrelation of the passive scalar fluctuations. Assuming the classical inertial range scaling for q , Thomson (1996) showed that the connection between the scalar dissipation rate and relative dispersion is given by

$$\frac{\partial \langle \theta'^2 \rangle}{\partial t} = -\frac{3}{2} \langle \theta'^2 \rangle \frac{\partial \ln \langle \mathbf{r}^2 \rangle}{\partial t} . \quad (1.45)$$

Obukhov (1949b) and Corrsin (1951) independently extended Kolmogorov's theory to the passive scalar and derived for the second order structure function of scalar increments

$$\langle (\theta'(\mathbf{r}, t) - \theta'(0, t))^2 \rangle = C_\theta \epsilon_\theta \epsilon^{-1/3} r^{2/3} , \quad (1.46)$$

where ϵ is the energy dissipation rate, $\epsilon_\theta = 2 \kappa \langle (\nabla \theta')^2 \rangle$ is the rate of dissipation of concentration fluctuations, and κ is the diffusivity. C_θ is known as the Obukhov-Corrsin constant. Experimental values of C_θ lie mostly in the

range $1.21 \leq C_\theta \leq 2.01$ (Sreenivasan, 1996). Thomson (1996), applying the two-particle statistical theory of Batchelor (1952), obtained a result relating the Obukhov-Corrsin constant to the Richardson-Obukhov constant

$$g = \frac{64}{243} \alpha_1^3 C_\theta^{-3}, \quad (1.47)$$

for some constant α_1 that shapes the spreading of the Richardson (1926) distance-neighbor function.

While many of the inertial range constants still elude precise theoretical modeling and experimental quantification, we believe that a complete theory of turbulence should and must unveil the interrelations between them. Here, we make no attempt at seeking such a fundamental relation, but we verify in chapter 5 the scalar invariance of C_2 , which is inherently implied in all theoretical investigations that invoked the local isotropy hypothesis, as well as in many single-point measurements that assumed Taylor's hypothesis.

1.4 Higher-order structure functions

In preparation for the examination of the influence of anisotropy on the scaling exponents of structure functions of order greater than 2 in chapter 6, we introduce in the following the higher-order structure functions and their role in the study of intermittency.

According to Landau and Lifshitz (1959), the arguments leading to Kolmogorov's prediction presented in the preceding sections do not take into account the possible 'bursty' nature of the energy dissipation rate. A distinctive feature of turbulence is its abrupt and extremely intense fluctuations in the ob-

servables. Landau's main objection is that the ϵ in Kolmogorov's theory is a mean taken over time. He argued that since ϵ fluctuates in time, $\langle \epsilon^n \rangle \neq \langle \epsilon \rangle^n$, except when $n = 1$, and therefore the mean rate of energy $\langle \epsilon \rangle$ is insufficient to describe turbulence. This phenomenon is known as intermittency. (See Frisch (1995), 6.4, for a historical account of Landau's objection.)

It has now become common in studies of intermittency to look at higher-order velocity structure functions. Kolmogorov's arguments can be naturally extended to moments of velocity increments, $\delta u(r) = u'(x+r) - u'(x)$, to order higher than two. For example, the p th-order longitudinal structure function, $D_p^L(r) = \langle (\delta u_L(r))^p \rangle$, where the subscript L indicates that the direction of velocity is along the separation vector, scales in the inertial range as

$$D_p^L(r) = C_p (\epsilon r)^{\zeta_p^L}, \quad (1.48)$$

with universal scaling exponents given by the Kolmogorov prediction

$$\zeta_p^L = p/3. \quad (1.49)$$

The values of ζ_p^L given by the above equation for order 1 to 6 are listed in table 1.1. The constants C_p s are presumed to be universal. To date, there exist no measurements that display unambiguous inertial range scaling over an enormously wide scaling range (Sreenivasan and Dhruva, 1998). Thus, several self-consistent procedures have been devised for better estimation of the scaling exponents. The Batchelor interpolation formula (equation 1.39), based on matched asymptotics, is useful but involves a very elaborate nonlinear fitting procedure (see e.g. Kurien and Sreenivasan, 2000). Another simple and intriguing procedure has been proposed by Benzi et al. (1993). They observed that structure functions plotted against any other structure function of a given order, rather than against the separation, generally yields a measurably improved

inertial scaling range at low Reynolds numbers. This procedure is known as the extended-self-similarity (ESS) method. The reason for its success in Navier-Stokes turbulence is unclear, but recent progress in Burgers turbulence explains this transformation of variables from physical to structure function space as a method to deplete the subdominant inertial and dissipative range contributions that mask power-law scaling (Chakraborty et al., 2010).

In practice, the third-order longitudinal structure function, $\langle(\delta u_L(r))^3\rangle$, is chosen as the surrogate for separation. The foundation for this choice lies in an exact result obtained by Kolmogorov (1941b) from the Navier-Stokes equation for freely decaying isotropic turbulence, and it remains the only exact result derived from the equations of motion. Starting with the Kármán-Harwarth equation (Kármán and Howarth, 1938), Kolmogorov rigorously showed that

$$D_3^L(r) = -\frac{4}{5}\epsilon r + 6\nu \frac{dD_2^L(r)}{dr}. \quad (1.50)$$

In the inertial range, this reduces to the celebrated Kolmogorov's four-fifths law (Kolmogorov, 1941b)

$$D_3^L(r) = -\frac{4}{5}\epsilon r. \quad (1.51)$$

Thus, relating the above to equation 1.48, the results $C_3 = -4/5$ and $\zeta_3^L = 1$ are both exact and nontrivial. To be precise, ESS can only be used to determine relative scaling exponents. Since ζ_3^L is exactly 1, the relative scaling exponents may be directly related to the true scaling exponents.

Another variant of ESS, which gives even better scaling, modifies structure functions of order p by taking the moments of the absolute values of the velocity increments, $\langle|\delta u_L|^p\rangle$, the so-called generalized structure functions (Vainshtein et al., 1994). Strictly speaking, the four-fifths law only applies to $\langle(\delta u_L)^3\rangle$, with no absolute value. Sreenivasan et al. (1996) have found small differences

in the scaling of $\langle(\delta u)^p\rangle$ and $\langle|\delta u|^p\rangle$. The difference is small, however, and is very difficult to observe experimentally. One then replaces the scaling laws in equation 1.48 by

$$\langle|\delta u_L|^p\rangle \propto \langle|\delta u_L|^3\rangle^{\zeta_p^L}. \quad (1.52)$$

Plotting the structure functions relative to $\langle|\delta u_L|^3\rangle$ shows cleaner inertial range scaling behavior than plotting them against the separations. Because of its utility in the longitudinal structure functions, the ESS technique has been extended to the transverse case. The transverse ESS scaling laws

$$\langle|\delta u_T|^p\rangle \propto \langle|\delta u_T|^3\rangle^{\zeta_p^T}, \quad (1.53)$$

where the subscript T denotes velocity direction perpendicular to the separation vector, and $\zeta_p^T = p/3$ is the inertial range scaling exponent given by the Kolmogorov prediction, $D_p^T(r) = C_p (\epsilon r)^{\zeta_p^T}$. This version of ESS is less justified, but is widely in use (e.g. Herweijer and Van de Water, 1995; Camussi et al., 1996; Kahalerras et al., 1996; Noullez et al., 1997; Van de Water and Herweijer, 1999; Zhou and Antonia, 2000; Pearson and Antonia, 2001; Zhou et al., 2001), although defining the transverse structure functions in this way always yields values for the odd moments, even when they do not exist for homogeneous isotropic turbulence (Shen and Warhaft, 2002). We will see in chapter 5 that at moderate Reynolds numbers, the inertial range is too narrow to fit a power law in r , and we will make use of ESS to determine ζ_p .

1.5 Anomalous transverse scaling exponents

As we have seen in the previous section, in order to verify the Kolmogorov prediction for the higher-order scaling exponents (equation 1.49), we naturally

ζ_p	Source	Order p					
		1	2	3	4	5	6
ζ_p^L	Kolmogorov (1941a)	0.333	0.667	1	1.333	1.667	2
	She and Leveque (1994)	0.364	0.696	1	1.280	1.538	1.778
	Dhruva et al. (1997)	0.366	0.700	1	1.266	1.493	1.692
ζ_p^T	Dhruva et al. (1997)	0.359	0.680	0.960	1.200	1.402	1.567

Table 1.1: The inertial range scaling exponents of the longitudinal and transverse structure functions. The first two rows are the longitudinal scaling exponents, ζ_p^L , predicted by Kolmogorov (1941a) (see equation 1.49) and She and Leveque (1994) (see equation 1.54). The third and fourth rows show the longitudinal and transverse exponents measured by Dhruva et al. (1997) using the ESS method (see section 1.4) in atmospheric turbulence at R_λ between 10^4 and 1.5×10^4 .

need to measure the higher-order structure functions. Measurements of the longitudinal structure functions up to the fourth order were first obtained by Van Atta and Chen (1970), and subsequently, up to the 18th order, by Anselmet et al. (1984). The longitudinal scaling exponents, ζ_p^L , from both measurements show departure from the expression 1.49 (the difference is less than 5% at fourth order, and increases monotonically up to 30% at 12th order), a phenomenon known as anomalous scaling, but it is well predicted by the She-Leveque model (She and Leveque, 1994) using a hierarchical model for the energy dissipation rate, which gives for the scaling exponent

$$\zeta_p^L = \frac{p}{9} + 2 \left[1 - \left(\frac{2}{3} \right)^{p/3} \right]. \quad (1.54)$$

The values of ζ_p^L given by the above equation for p up to the sixth order are listed in table 1.1.

It was thought that the transverse scaling exponent, ζ_p^T (defined in equa-

tion 1.53), is equal to ζ_p^L . This is true only for $p = 2$ because of the incompressibility condition (see equation 1.18). For $p \neq 2$, the transverse and longitudinal scaling exponents are not related by any constraint. In fact, measurements of Herweijer and Van de Water (1995) in shear flows at $R_\lambda = 340 - 810$ did suggest that the difference $\zeta_p^T - p/3$ is larger than $\zeta_p^L - p/3$ for $p \geq 4$, implying that $\zeta_p^T < \zeta_p^L$ for $p \geq 4$. The difference persists even at R_λ up to 10^4 , as shown by the hot-wire measurements of Dhruva et al. (1997) in the atmospheric surface layer, reproduced in table 1.1. The same result is found in other experiments (Camussi and Benzi, 1997; Antonia and Pearson, 1999; Zhou and Antonia, 2000; Romano and Antonia, 2001; Hao et al., 2008) and numerical simulations (Chen et al., 1997; Boratav and Pelz, 1997; Grossmann et al., 1997; Gotoh et al., 2002). A number of experiments, however, suggest that the two exponents are equal (Camussi et al., 1996; Noullez et al., 1997; Kahalerras et al., 1998; He et al., 1999). A few authors (Pearson and Antonia, 2001; Zhou et al., 2001; Antonia et al., 2002; Shen and Warhaft, 2002; Zhou et al., 2005) report both $\zeta_p^T \sim \zeta_p^L$ and $\zeta_p^T < \zeta_p^L$ in their experiments.

Table 1.2 is an assessment of the issue. We would like to caution the reader of a too simplistic interpretation of table 1.2. The flow conditions, measurement techniques, and the definitions of ζ_p^L and ζ_p^T vary from experiment to experiment. We note that in most experiments, Taylor's hypothesis has been invoked to surrogate temporal series of measurements for spatial ones (see the sidebar Taylor's Hypothesis in section 1.2). On the other hand, Lin (1953) has shown that the hypothesis breaks down in the case of flows containing high shear. Correction to Taylor's hypothesis based on spectral information gathered in only one direction and on a local derivative in the remaining direction has been proposed by del Álamo and Jiménez (2009). We note that in some cases

Flow	TH	R_λ	Scaling exponent	Source
Shearless	No	100 – 300	$\zeta_p^T \lesssim \zeta_p^L$	Zhou et al. (2005)
Shearless	No	863	$\zeta_p^T \sim \zeta_p^L$	Shen and Warhaft (2002)
Shearless	Yes	100 – 300	$\zeta_p^T < \zeta_p^L$	Zhou et al. (2005)
Shearless	Yes	863	$\zeta_p^T < \zeta_p^L$	Shen and Warhaft (2002)
Shearless	Yes	$10^4 - 1.5 \times 10^4$	$\zeta_p^T \lesssim \zeta_p^L$	Dhruva et al. (1997)
Sheared	No	254	$\zeta_p^T < \zeta_p^L$	Shen and Warhaft (2002)
Sheared	No	875	$\zeta_p^T \sim \zeta_p^L$	Shen and Warhaft (2002)
Sheared	Yes	254	ESS not applicable	Shen and Warhaft (2002)
Sheared	Yes	875	$\zeta_p^T < \zeta_p^L$	Shen and Warhaft (2002)

Table 1.2: The equality between longitudinal and transverse scaling exponents for sheared and unsheared turbulence and their trends with Reynolds number. The acronym TH denotes the use of Taylor’s hypothesis in the experiments.

when the scaling exponents do agree, Taylor’s hypothesis has not been invoked (e.g. Noullez et al., 1997; Shen and Warhaft, 2002; Zhou et al., 2005) or a modified version based on the instantaneous velocity $u(t)$, instead of the mean velocity $\langle U \rangle$, has been used to obtain the spatial separation $\Delta r = u(t) \Delta t$ (e.g. Kahalerras et al., 1998). Because many authors report only structure functions constructed from single-point measurements of the velocity signals, we have deliberately limited the scope of comparison in table 1.2 to those that report two-point measurements that truly scan the physical space.

Our second observation is that there is no consensus among researchers on the choice of the third order structure function for the ESS method. While all researchers agree on using the ESS scaling $\langle |\delta u_L|^p \rangle \propto \langle |\delta u_L|^3 \rangle \zeta_p^L$ for ζ_p^L , the ESS scalings $\langle |\delta u_T|^p \rangle \propto \langle |\delta u_L|^3 \rangle \zeta_p^T$ and $\langle |\delta u_T|^p \rangle \propto \langle |\delta u_T|^3 \rangle \zeta_p^T$ have been proposed for

ζ_p^T . We observe in the data of Pearson and Antonia (2001); Zhou et al. (2001, 2005) that ESS scaling based on $\langle |\delta u_L|^3 \rangle$ tends to produce a wider scatter and a value for ζ_p^T that is smaller than the one obtained with $\langle |\delta u_T|^3 \rangle$. We think that the uncertainty in the reported values of ζ_p^T partly stems from the inconsistency in the procedure used in obtaining the transverse scaling exponent and our attempt here is to test the directional dependence of $\langle |\delta u_T|^p \rangle \propto \langle |\delta u_T|^3 \rangle^{\zeta_p^T}$.

The difference between the longitudinal and transverse scaling exponents remains one of the unresolved issues of turbulence. The reasons for this inequality have been proposed by various authors. For example, Romano and Antonia (2001) and Zhou et al. (2001) list the following as plausible explanations: *a)* the anisotropy of the large scale, *b)* the Reynolds number effect, *c)* the differences in initial and boundary conditions, *d)* different intermittency. *e)* the effect of Taylor's hypothesis. Among these possible causes, which may be related, Romano and Antonia (2001) have singled out the anisotropy of the flow as the most likely source for the observed inequality.

A complementary approach has been developed to extract the anisotropic contributions to the scaling of structure functions (Biferale and Procaccia, 2005). This approach uses the irreducible representation of the SO(3) symmetry group. Instead of projecting the structure functions onto the longitudinal and transverse components in the traditional way, we expand the structure functions in terms of spherical harmonics⁸, Y_ℓ^m , sidestepping the questions about the differences between longitudinal and transverse scaling exponents. Because the isotropic ($\ell = 0$) and anisotropic parts ($\ell = 1, 2, \dots$) of the structure functions are naturally decoupled in this representation, one could ask how does the value

⁸Following the usual convention, the orbital angular momentum is represented by ℓ . Its projection onto the z axis is represented by m .

of the anisotropic scaling exponent compare to that of the isotropic one? The first-order anisotropic scaling exponent has been calculated using perturbation theory (Grossmann et al., 1994; Falkovich and L'vov, 1995) and is found to be higher than the isotropic one. Borrowing results from passive scalar turbulence (Fairhall et al., 1996), it is then conjectured that all higher order anisotropic scaling exponents are positive, greater than the isotropic scaling exponent, and increase with increasing order (L'vov and Procaccia, 1996). If this is true, then these nondecreasing anisotropic exponents would neatly explain the diminishing anisotropic scaling contributions with decreasing scale. Initial tests have been conducted in atmospheric boundary layer flows (Arad et al., 1998; Kurien et al., 2000; Kurien and Sreenivasan, 2000) and the results suggest a hierarchy of increasingly larger anisotropic scaling exponents with increasing order. Succeeding measurements in laboratory homogeneous shear flows (Warhaft and Shen, 2002), however, have cast doubt on the conclusion reached by the above authors and more refined experimental analyses have found the results to depend on the geometrical configuration of the measurement probes (Staicu et al., 2003). The $SO(3)$ decomposition is in its infancy. The technique clearly awaits a more impartial analysis and more refined experimental techniques⁹.

1.6 Anisotropic turbulence

As discussed in section 1.1, Kolmogorov's theory presumes that, at sufficiently high Reynolds numbers, the small scales of the turbulence are statistically homogeneous, isotropic, and free of externally imposed boundary. Few geophys-

⁹The well-crafted argument that the method might improve at higher Reynolds numbers is problematic because it is precisely at moderate Reynolds numbers that the method makes many of its claims (e.g. Arad et al., 1999; Biferale and Toschi, 2001).

Flow	Anisotropy	Direction	Source
Urban surface layer	1.9 : 1.5 : 1	streamwise/spanwise/vertical	Roth (2000)
Rural surface layer	2 : 1.5 : 1	streamwise/spanwise/vertical	Counihan (1975)
Marine surface layer	1.83 : 2.6 : 1	streamwise/spanwise/vertical	Friehe et al. (1991)
Mixing layer	1.3	streamwise/vertical	Finnigan (2000)
Canopy	1.7	streamwise/vertical	Finnigan (2000)
Sea surface current	0.44 – 2.18	zonal/meridional	Ducet et al. (2000)
Martian boundary layer	1.06	zonal/meridional	Sullivan et al. (2000)

Table 1.3: The landscape of anisotropy for geophysical flows. Anisotropy refers to the ratio of streamwise to spanwise to vertical, streamwise to vertical, or zonal to meridional RMS velocity fluctuations, depending on the context. In Sullivan et al. (2000) the RMS velocity fluctuation data are unavailable. The anisotropy quoted is for the mean wind speed.

ical and laboratory flows fulfill these requirements. Field measurements in the atmospheric boundary layer show that atmospheric flows attain the highest ever Reynolds number (R_λ) achievable on Earth, typically of the order 10^4 (e.g. Dhruva et al., 1997). Complex terrestrial terrain and planetary dynamics, however, may influence the energy-containing scales of turbulent motion. Consequently, one would expect motion at these scales to be anisotropic. Table 1.3 offers a few glimpses of the degree of anisotropy in nature. And how does man-made turbulence compare with nature? Our reaction to table 1.4 is one of amazement. Despite the moderate Reynolds number, laboratory flows created under different conditions possess approximately the same degree of anisotropy as nature.

What causes this anisotropy in the energy-containing scales of turbulence? Is it a reflection of the asymmetry in the mechanism that agitates the fluid? There is ample evidence to support a causal relationship between asymmetry

and anisotropy, but the relationship has not been tested experimentally. This evidence includes flows where asymmetry and anisotropy are present at the same time, such as in turbulent pipe flows (Pearson and Antonia, 2001), turbulent jets (e.g. Romano and Antonia, 2001), counter-rotating von Kármán flows (e.g. Voth et al., 2002), and wind tunnels with specially designed shear generators (e.g. Shen and Warhaft, 2000; Isaza et al., 2009). Turbulence produced by computer simulation can also be forced in an asymmetric way, and Yeung and Brasseur (1991) studied the influence of this asymmetry. One exception is the turbulence produced by a grid in a wind tunnel with a specially designed contraction, where the axis of the tunnel introduces a clear asymmetry, yet the turbulence produced is nearly locally isotropic, but decaying (Comte-Bellot and Corrsin, 1966).

There is a pattern in the relationship between asymmetry of the forcing and anisotropy of the turbulence. Machines with a single axis of symmetry, such as the von Kármán flow generators (e.g. Voth et al., 2002) and wind tunnels (e.g. Comte-Bellot and Corrsin, 1966), produced axisymmetric turbulence. Machines with more axes, such as the one developed by Hwang and Eaton (2004), produced isotropic turbulence. A careful study by Zimmermann et al. (2010) showed that six axes were sufficient to produce turbulence without a preferred direction. The machine to be described in this thesis has 16 axes.

Flow	Measurement location	R_λ	u'/v'	Direction	Source
Grid turbulence	$45 d$	669	1.23	streamwise/spanwise	Kistler and Vrebalovich (1966)
Grid (uncontracted)	$20 d - 200 d$	$37 - 72$	$1.05 - 1.25$	streamwise/spanwise	Comte-Bellot and Corrsin (1966)
Grid (contracted)	$20 d - 200 d$	$37 - 72$	$0.96 - 1.07$	streamwise/spanwise	Comte-Bellot and Corrsin (1966)
Oscillating grid	center plane	31	1.05	vertical/horizontal	Shy et al. (1997)
Cylinder wake	$75 d$ centerline	320	1.17	streamwise/spanwise	Hao et al. (2008)
Pipe flow	$100 d$ centerline	326	1.67	streamwise/spanwise	Pearson and Antonia (2001)
Jet	$40 d$ centerline	500	1.32	streamwise/spanwise	Romano and Antonia (2001)
von Kármán flow	center	970	1.47	radial/axial	Voth et al. (2002)
Wind tunnel shear flow	$6 d$	974	1.53	streamwise/spanwise	Shen and Warhaft (2000)
Plane jet	$50 d$	1107	1.13	streamwise/spanwise	Pearson and Antonia (2001)
Boundary layer	$0.37 d$	1450	1.26	streamwise/spanwise	Saddoughi and Veeravalli (1994)

Table 1.4: A bird’s eye view of the anisotropy observed in laboratory flows. The symbol d refers to distance between grid center lines, cylinder diameter, pipe diameter, jet nozzle diameter, tunnel width, jet width, or the boundary layer thickness, depending on the context. u'/v' refers to the ratio of streamwise to spanwise, vertical to horizontal, or radial to axial RMS velocity fluctuations, depending on the context. Shy et al. (1997) did not specify the Reynolds number, it is estimated from equation 1.7.

Batchelor (1946a) initiated the study of anisotropic turbulence by considering turbulence with reduced symmetry, namely symmetry about an axis, drawing motivation from wind-tunnel and pipe flows. Applying the invariant theory of Robertson (1940), Batchelor (1946a) showed that the correlation tensor, $R_{ij}(\mathbf{r}) = \langle u'_i(\mathbf{r} + \mathbf{x}) u'_j(\mathbf{x}) \rangle$, can be described by a single scalar function in systems of high symmetry (isotropic), but in axisymmetric turbulence additional functions are required. Chandrasekhar (1950) showed that it can be written in terms of only two independent scalar functions, which are not directly measurable. For two special forms of this tensor, which represent possibly the simplest kinds of non-isotropic turbulence, Sreenivasan and Narasimha (1978) showed that it is sufficient to give two functions of a single variable or even one function of a single variable with an additional parameter. An experimentally-oriented formulation developed by Lindborg (1995) re-expressed the correlation tensor in terms of 6 measurable two-parameter scalar functions, but because of reflectional symmetry only two of them are independent.

As the rank of the tensor increases, so does the number of independent functions we need to describe the tensor. Simple symmetry arguments, however, may reduce the number of terms and greatly simplify the expression. Let us consider $R_{ij}(x_k)$ where i, j, k are cyclic permutations of the indices 1, 2, 3. Reflectional symmetries of the Navier-Stokes equation about the $x - y$, $y - z$, and $x - z$ planes yield (e.g. Lindborg, 1995)

$$R_{ij}(x_k) = 0, \tag{1.55}$$

for all permutations of $(i, j, k) = (1, 2, 3)$. This is nothing but a consequence of the conservation of parity.

In principle, to fully describe the axisymmetric turbulence, all 6 functions

would need to be measured. Here, we ingeniously designed our flow apparatus to allow rotations of the anisotropic large scale forcing, instead of the measurement apparatus, in order to measure parts of two out of these six functions with separations that extended radially from the center of the turbulent region. In the same spirit as the previous sections, we shall examine in chapter 7 the directional dependence of these correlations in anisotropic turbulence.

1.7 Overview

The central idea that interweaves all the chapters in this thesis is anisotropic turbulence. From this idea, we develop three interrelated sub-themes. First, we discuss the generation of anisotropic turbulence in the laboratory. In chapter 2, we introduce the turbulence generation apparatus and describe the accompanying flow measurement technique. Following this, in chapter 3, we explain the coordinate system we have used to present our measurements, and describe the measurement protocol and methods. In chapter 4, we examine the performance of the turbulence generator. We discuss three aspects of the large scale velocity fluctuations: the uniformity in the anisotropy, axisymmetry, and homogeneity. Combining these and the auxiliary measurements of the mean flow, the velocity fluctuations mixed correlation, and the Reynolds stress, we evaluate to what degree the turbulence in the fluid is homogeneous and axisymmetric.

The second idea concerns the influence of large scale anisotropy on the inertial scales of turbulence. This influence is traditionally studied through the structure functions. In chapter 5, we review the existing works on anisotropy in structure functions. We examine an aspect that has been overlooked in the

literature, namely the behavior of second-order transverse structure functions in different directions of the flow. We found that the two structure functions become equal at the inertial scales. This contrasts with existing results obtained in shear flows and suggests that anisotropy produced in the fluctuations and that produced by shear are likely to be fundamentally different. Our measurements suggest that the Kolmogorov constant is independent of the direction in which it is measured. This we exploit to determine the parameters of the turbulence. Following this, in chapter 6, we examine structure functions of order four, five, and six. We illustrate the difficulty in obtaining precise measurements of these structure functions with measurements of their probability density functions. We demonstrate the possible influence anisotropy might have on the shape of the probability density functions.

The third idea covers the influence of large scale anisotropy on the integral scales of turbulence. This is studied through the correlation functions. In chapter 7, we devote ourselves to the analysis of transverse correlation functions measured in different directions. We observed that they deviate from each other at the large scale. We propose a scaling form similar to one that is studied in problems dealing with critical phenomena, and combine it with Kolmogorov-type inertial range scaling to show that the data collapse when appropriately scaled. We then derive a power-law relationship between the integral length and the large scale velocity fluctuation and demonstrate that the power-law exponent is indeed linked to the inertial range scaling exponent.

Finally, in chapter 8, we summarize the results presented in this thesis and discuss several shortcomings of our arguments, as well as future measurements that may complement and extend the results of this thesis.

CHAPTER 2

THE FLOW APPARATUS AND THE MEASUREMENT TECHNIQUE

The goal of the present experimental study is to generate a closer approximation to tunable and anisotropic, but unsheared, turbulent flows than those obtained by Shen and Warhaft (2002), which we accomplished through the construction of a flow apparatus described hereunder. The apparatus makes systematic studies of anisotropic turbulence feasible, and a direct comparison of anisotropic turbulence with isotropic turbulence in a single apparatus possible. The flows generated by this apparatus are characterized using laser Doppler velocimetry (LDV). We review the LDV measurement technique and discuss some of the essential features, only to a degree sufficient for the understanding of this thesis.

2.1 The flow apparatus

We now describe our turbulence chamber, the loudspeaker turbulence generator and the loudspeaker amplifier unit. We review in some detail the algorithm we used for driving the turbulence generators.

2.1.1 The chamber

The geometry of our flow chamber was inspired by the apparatus developed by Zimmermann et al. (2010) at the Max Planck Institute for Dynamics and Self-Organization in Göttingen, Germany. As shown in figure 2.1, our turbulence chamber had the shape of a truncated icosahedron and it had a diameter of

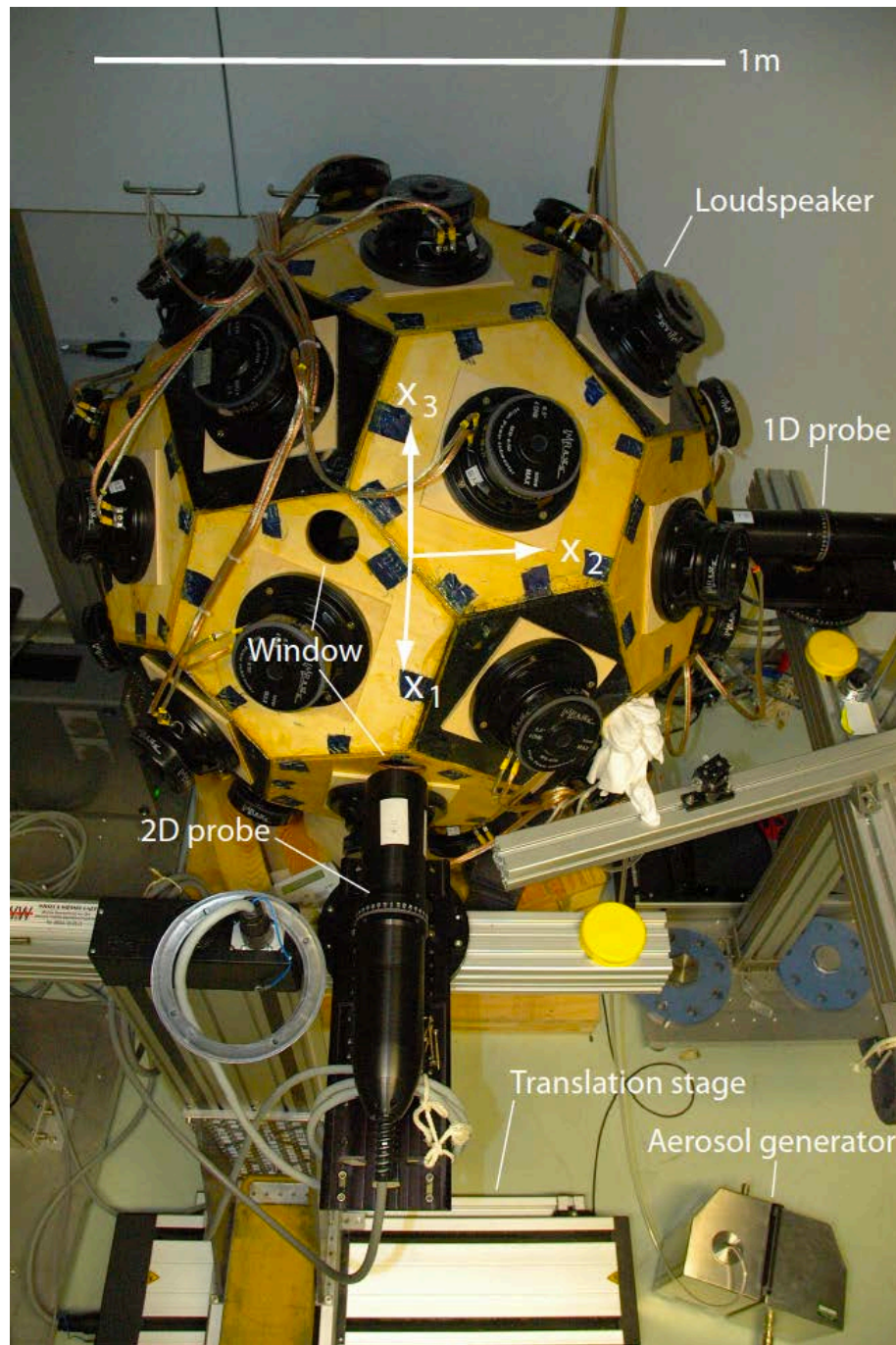


Figure 2.1: The 'soccer ball' chamber. Also shown is the layout of the Laser Doppler velocimetry probes in the experiment. A two-component probe aligned along the x_1 -axis measured the components of velocity in the x_2 and x_3 directions, and an additional one-component probe aligned along the x_2 axis measured velocities in the x_3 direction.

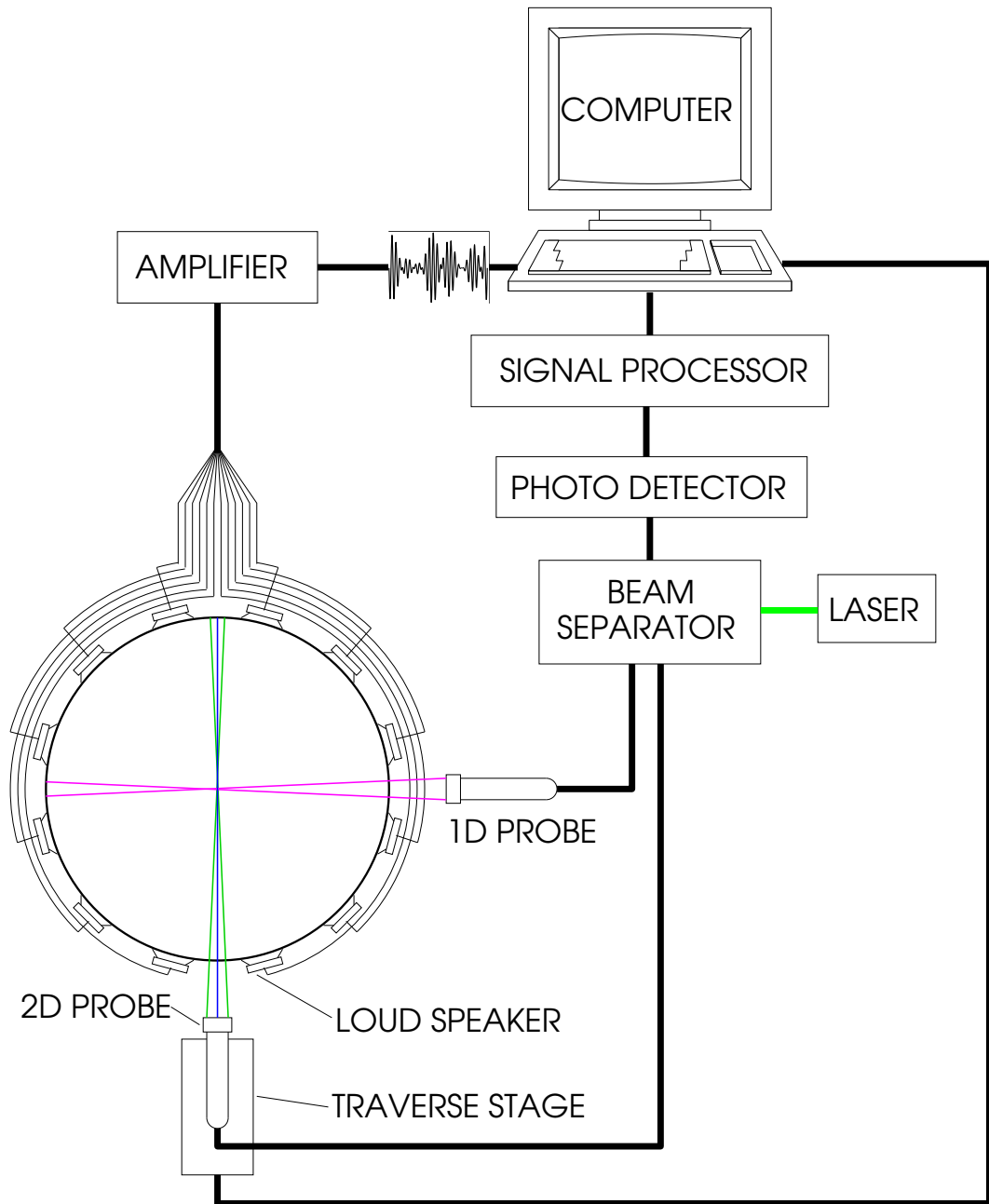


Figure 2.2: An overview of the experiment showing the 'soccer ball', the amplifier unit, and the measurement apparatus. The amplifier received signals from the multichannel high-speed voltage output device on the computer through a BNC connector block, and sent the signals to the loudspeaker array on the soccer ball. A laser Doppler velocimetry (LDV) system collected velocity signals and saved the data on a computer (not shown).

99 cm. It was made of wood with twelve regular pentagonal and twenty regular hexagonal faces joined together with nylon straps and glue. The inner and outer surfaces were coated with several layers of lacquer to make the chamber water repellent. In the center of each face, a circular hole was cut for the jet generator. In addition, further circular holes adjacent to the jet generators were cut out for optical access. As the shape resembles that of a soccer ball, we also refer to the flow apparatus as the 'soccer ball' chamber.

2.1.2 The loudspeaker

As depicted in figure 2.3, the turbulence mixers were jets, or jet-like winds that are produced by powerful acoustic sources in air, developed for flow control applications (Glezer and Amitay, 2002). A 150 W loudspeaker with a diameter of 16.5 cm and a uniform frequency response between 50 and 3000 Hz, was mounted on each face of the soccer ball and pointed towards the center of the chamber. The loudspeakers pushed air in and out through conical nozzles of opening angle 30° , length 4.3 cm and orifice diameter 5 cm. Each nozzle was held between a face of the soccer ball and a square wooden plate. By using a sinusoidal driving of the loudspeaker, we generated a pulsating turbulent jet, a phenomena known as acoustic streaming (Lighthill, 1978). When backing away from the orifice, the loudspeaker diaphragm ingests air from all directions, while it blows air out in a single direction when moving toward the orifice. As the jet travels downstream and reaches the center of the soccer ball, it interacts with other jets created by other loudspeakers. These interactions produce a turbulent region that is more intense than the turbulence due to a single turbulent jet. The sound level inside the soccer ball was typically 135 dB, which

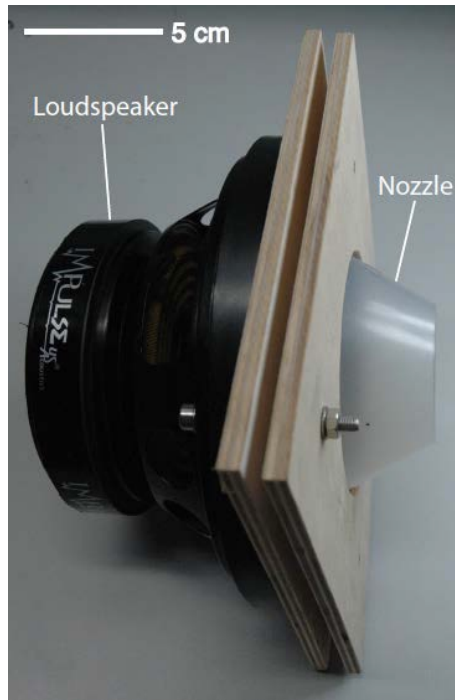


Figure 2.3: A loudspeaker with a conical nozzle.

corresponds to 0.2% of the measured turbulent kinetic energy. Thus, we expect the sound to have a negligible effect on the turbulence and the measurements of velocity.

The flow chamber was similar to the ones described by Hwang and Eaton (2004); Webster et al. (2004); Warnaars et al. (2006); Lu et al. (2008); Goepfert et al. (2010). The chamber by Hwang and Eaton was a $410 \times 410 \times 410 \text{ mm}^3$ cubical Plexiglas box, from which the corners were cut off to make the internal volume of the chamber closer to spherical. A loudspeaker-driven jet was mounted at each vertex, and aimed toward the center of the chamber. The loudspeakers were driven with sine waves, each with a random frequency and phase, to discourage the formation of standing waves or periodic structure inside the chamber; the power spectra were uniform in the range from 90 Hz

	Hwang & Eaton (2004)	Webster <i>et al.</i> (2004)	Warnaars <i>et al.</i> (2006)	Lu <i>et al.</i> (2008)	Goepfert <i>et al.</i> (2010)	Present work
Geometry	Truncated cube	Truncated cube	Rectangular	Truncated cube	Octahedron	Truncated icosahedron
Flow medium	Air	Saltwater	Water	Air	Air	Air
ϵ (m^2/s^3)	11	2.5×10^{-5}	1.25×10^{-6}	1.4	5.8	6.71
η (μm)	130	450	950	220	155	150
τ_η (ms)	1.2	200	1000	3.3	1.6	1.5
R_λ	220	68	5.89	260	250	480

Table 2.1: The chamber geometry and flow statistics from various speaker-driven flow chambers. The symbols from top to bottom are: energy dissipation rate (ϵ), Kolmogorov length scale (η), Kolmogorov time scale (τ_η), Taylor micro-scale Reynolds number (R_λ). For each study, only the case that gave the highest Reynolds number is reported.

to 110 Hz. The approach by Hwang and Eaton had inspired the design of flow apparatuses by various workers interested in the generation of homogeneous and isotropic turbulence; see Webster et al. (2004); Warnaars et al. (2006); Lu et al. (2008); Goepfert et al. (2010). We compare the flow parameters in table 2.1.

2.1.3 The driving algorithm

Here, we drove the loudspeakers with signals chosen to generate a flow with the desired anisotropy and low mean velocity. We achieved this by modulating the amplitude of a sine wave with independent noise (Fox et al., 1988) of correlation time 0.1 seconds, which was approximately equal to the large-scale eddy turn over time, \mathcal{L}/u' , \mathcal{L} being a characteristic length scale describing the large-scale motions of the flow (see section 7.1 for a definition), and u' being the RMS velocity fluctuations. This condition ensured that fluctuations in the energy input rate to the turbulence occurred on time scales that were equal to or faster than the turbulence decay time, so that the turbulence was in a steady state. In any case, we found that the statistical properties of the turbulence were insensitive to the correlation time.

At any given time t , the voltage for the i -th speaker was an amplitude-modulated sine signal

$$a_i = \delta_i \sin(2\pi f t), \quad (2.1)$$

where δ_i is the modulating noise and f is the base frequency of the sine wave. We drove the loudspeakers in phase and 50 Hz produced the strongest jet. The exponentially correlated noise δ_i was calculated according to the algorithm given by Fox et al. (1988). We first set the step size Δt , and the parameters D

and λ . At each time step, we picked two random numbers p and q , uniformly distributed on $[0, 1]$, and computed the following

$$E = \exp(-\lambda \Delta t), \quad (2.2)$$

$$h = [-2 D \lambda (1 - E^2) \ln(p)]^{1/2} \cos(2 \pi q), \quad (2.3)$$

$$\delta_i(t + \Delta t) = E \delta_i(t) + h. \quad (2.4)$$

It follows that δ_i is an exponentially correlated noise with the properties (Fox et al., 1988)

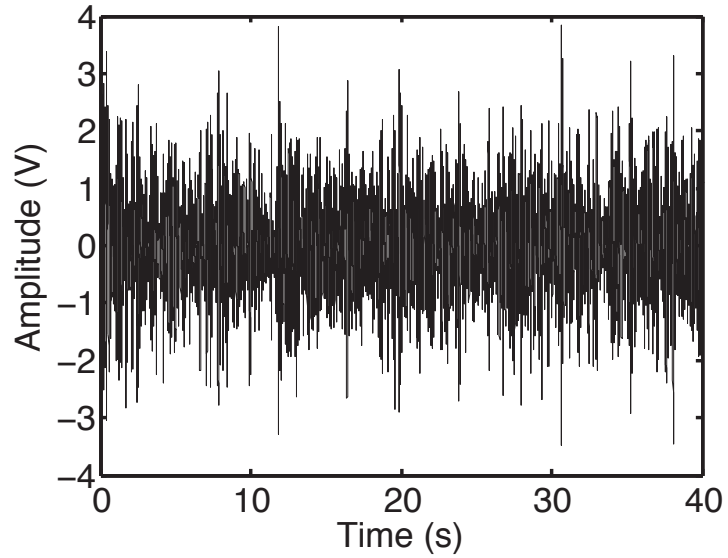
$$\langle \delta_i(t) \rangle = 0, \quad (2.5)$$

$$\overline{\langle \delta_i(t) \delta_i(s) \rangle} = D \lambda \exp(-\lambda |t - s|). \quad (2.6)$$

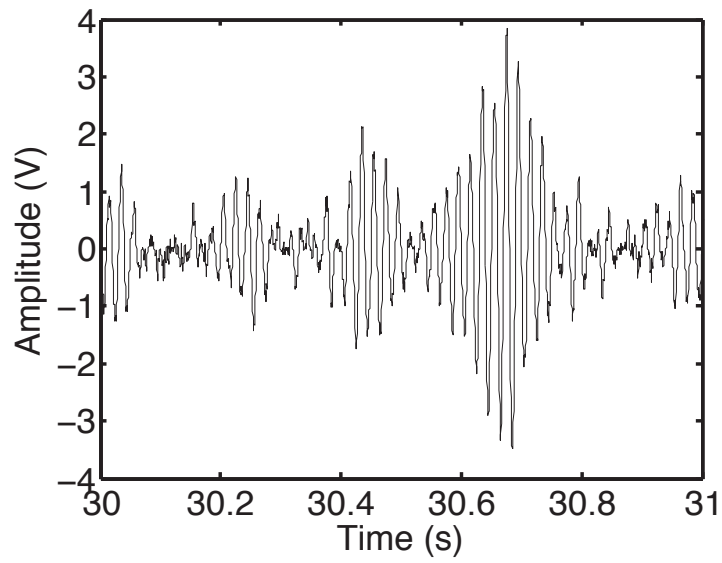
It can be seen from 2.6 that λ^{-1} is the correlation time for the noise.

Figure 2.4(a) shows a typical time series of the voltages generated at a sampling frequency $1/\Delta t = 3000$ Hz. A MATLAB[®] script to generate this is given in appendix C. We had set $\lambda = 10 \text{ s}^{-1}$, $D = 0.1 \text{ s}$, and the initial condition $\delta_i(t = 0) = 0$. The sequence was about 40 s long and the RMS voltage was 1 V. Zooming into the sequence, figure 2.4(b) shows the fine structure within 1 s of the signal. Because the correlation time of the noise is five times larger than the period of the carrier wave, the voltage amplitude varies slowly with time.

Figure 2.5(a) shows the unfiltered power spectrum of the voltage signal. The trend being masked by noise, in figure 2.5(b) we filter the spectrum with a running average to show the intended data. The spectrum was uniform up to about 30 Hz, at which point the spectrum increased steadily with increasing frequency and reached a peak at the carrier frequency of 50 Hz, after which the spectrum fell off approximately inversely proportional to the square of the frequency.

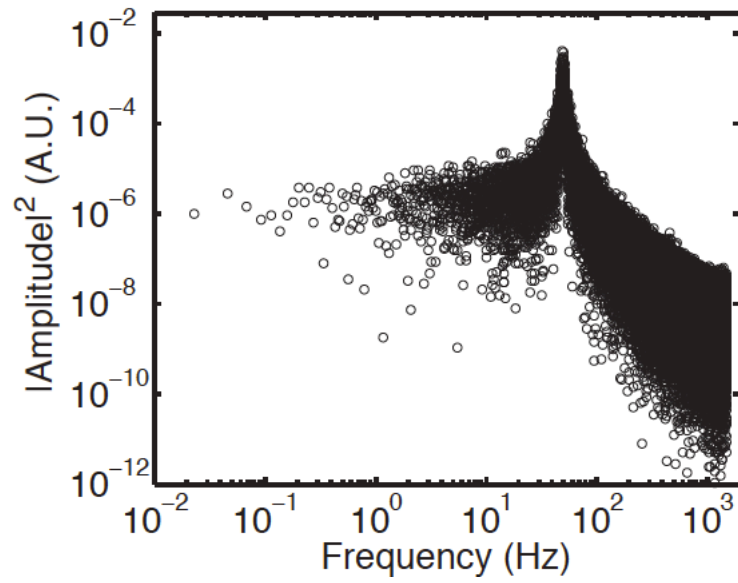


(a)

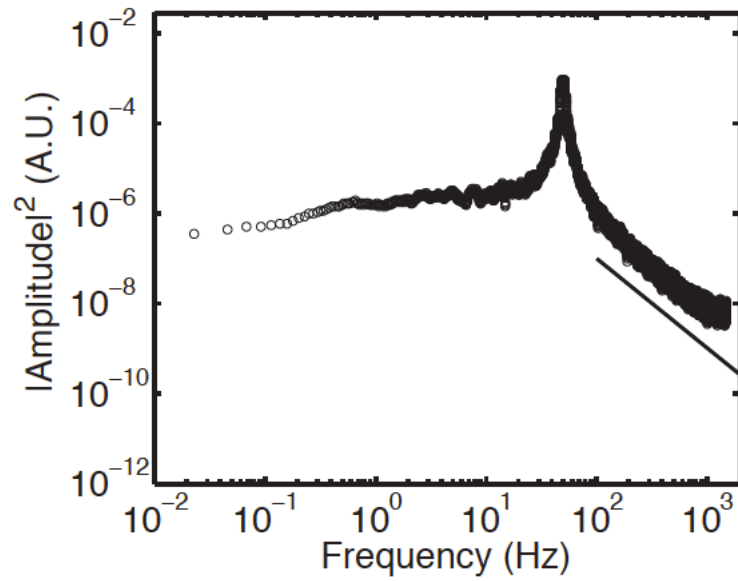


(b)

Figure 2.4: (a) A 40-second time series of the voltage applied to the loudspeakers. (b) A part of the time series, zoomed in to reveal the 50 Hz carrier wave.



(a)



(b)

Figure 2.5: The spectrum of the voltage applied to the loudspeakers (a) before filtering and (b) after filtering. The solid line in (b) is proportional to a power law with an exponent of -2 .

Finally, to avoid mean flows, the amplitudes of each driving signal are constrained so that they sum to zero. This is ensured by sending

$$a_i - \frac{1}{32} \sum_{j=1}^{32} a_j, \quad (2.7)$$

to the i -th loudspeaker. If the response of the loudspeakers to the driving signal is linear, this adjustment maintains a constant volume of air in the flow apparatus. It also reduces the amplitude of the sound generated by the loudspeakers, and minimizes the amount of air exchanged between the inside of the apparatus and the room.

The code for driving the loudspeakers was programmed in a LabView environment. The 32 independent voltage signals were generated with a National Instruments 32-channel DAQ card (NI PCI-6723) on a computer and amplified by an amplifier unit before being sent out to the loudspeakers.

2.1.4 The distribution of amplitudes

The distribution of loudspeaker amplitudes is shown in figure 2.6. By calibrating the RMS amplitude of each loudspeaker along the surface of the soccer ball, we were able to select the desired anisotropy. As we restricted ourselves to cylindrically symmetric forcing, the asymmetry can be characterized by the ratio of the axial amplitude, b_{axial} , to the radial amplitude, b_{radial} :

$$A = \frac{b_{\text{axial}}}{b_{\text{radial}}}. \quad (2.8)$$

Here, the RMS amplitudes are taken as $b_{\text{axial}} = \langle a_{\text{axial}}^2 \rangle^{1/2}$ and $b_{\text{radial}} = \langle a_{\text{radial}}^2 \rangle^{1/2}$, where $\langle a_{\text{axial}}^2 \rangle$ and $\langle a_{\text{radial}}^2 \rangle$ refer to the RMS amplitude of the polar and equatorial loudspeakers, respectively. A forcing is then described as exhibiting oblate

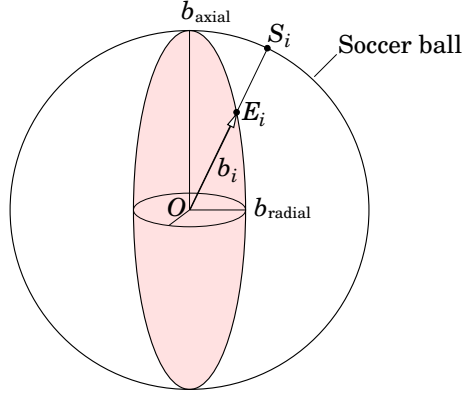


Figure 2.6: A sketch showing the assignment of RMS amplitude for a given loudspeaker. The vector pointing from the center of a sphere, O , to the center of a loudspeaker, S_i , intersects an inscribed ellipsoid at E_i . The distance of E_i from the center of the sphere sets the RMS amplitude b_i for the given loudspeaker.

(pancake) asymmetry when $0 < A < 1$, spherical symmetry when $A = 1$, and prolate (cigar) asymmetry when $A > 1$.

As we have 32 loudspeakers distributed in an icosahedral symmetry, the RMS amplitude for a given loudspeaker was set according to the following scheme. As shown in figure 2.6, a vector was drawn from the center of the sphere to the center of the loudspeaker. We calculated the intersection between the vector and the surface of an inscribed ellipsoid, which had the same center as the sphere. The distance between this intersection and the center of the soccer ball set the relative RMS amplitude for the given loudspeaker. Given an asymmetry A and any one of the principal radii, b_{axial} and b_{raial} , the geometrical shape of the ellipsoid is uniquely specified. Therefore, the distances may be precalculated once and used for setting the RMS amplitudes for all the loudspeakers.

Figure 2.7(a) shows a typical fluid velocity time series when the 32 loudspeakers were driven according to the prescription described above. Figure 2.7(b) shows the velocity spectrum calculated using Lomb algorithm for

unequally spaced data¹ (see e.g. Press et al. (2007)). We did not detect the 50 Hz oscillation in the velocity spectrum. We think that any traces of such periodic excitation may have been erased as a result of the fluid mechanical interactions between multiple turbulent jets.

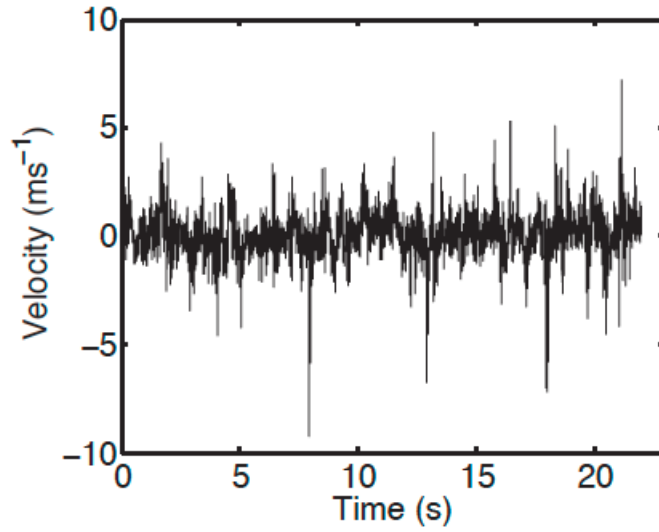
2.1.5 The amplifier

Sixteen Raveland XCA 700 two-channel amplifiers, each being capable of delivering up to 700 Watts of power, amplified the digital signals sent through a PCI-to-BNC interface. The design and building of the amplifier unit was done by Ortwin Kurre and his technical assistants from the electronic shop at the Max Planck Institute for Dynamics and Self-Organization in Goettingen, Germany.

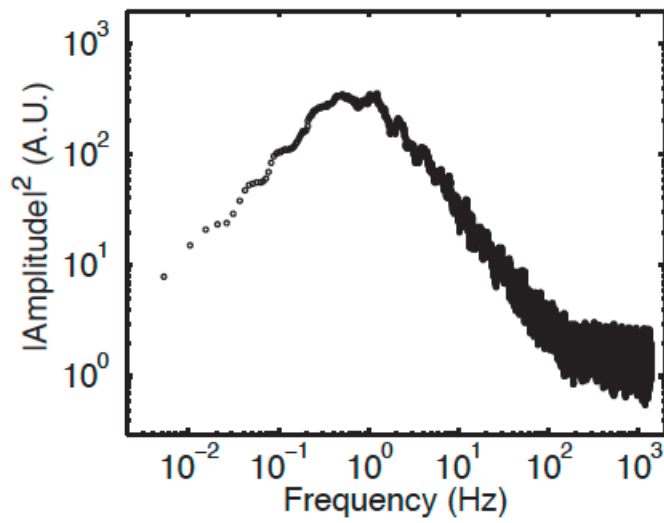
2.2 Laser Doppler Velocimetry

Much of the information about the flows we generated inside the soccer ball was collected using laser Doppler velocimetry (LDV). It is a technique for extracting the components of the velocity of individual particles from the light scattered by them (e.g. Albrecht et al., 2003). A laser light source is an essential part of the technique. As shown in figure 2.10, two beams of collimated, monochromatic, and coherent laser light are focused by a converging lens and made to cross at their respective focal point, where they interfere and generate a set of straight fringes. Focusing is not essential to the explanation that will be made, but is only required for making the intersection volume small so that only one par-

¹The MATLAB[®] code by C. Saragiotis for calculating spectrum with Lomb algorithm is greatly acknowledged.



(a)



(b)

Figure 2.7: The figure shows (a) a truncated time series of one component of the fluid velocities in response to the forcing and (b) its spectrum calculated using the Lomb algorithm for unequally spaced data.



Bild oben
 Endstufe NF-Eingänge & Regler
 NF-Ausgänge & Spannungsversorgung
 Bild unten



Figure 2.8: The Raveland amplifier.

ticle can be inside this volume at any given time. As individual particles pass through the fringes in the measurement volume, defined by the crossing of the two beams and is approximately ellipsoidal in shape, they reflect light from the regions of constructive interference into a photo detector. The component of velocity perpendicular to the fringes can be calculated from the frequency of the signal received at the detector. There exist, in the literature, two explanations for the frequency dependency of the particle velocity (e.g. Albrecht et al., 2003). Both yield the same result but the explanations differ slightly in their starting point and emphasis. We review them in the following sections and discuss the limitations of LDV for turbulence measurements in air.

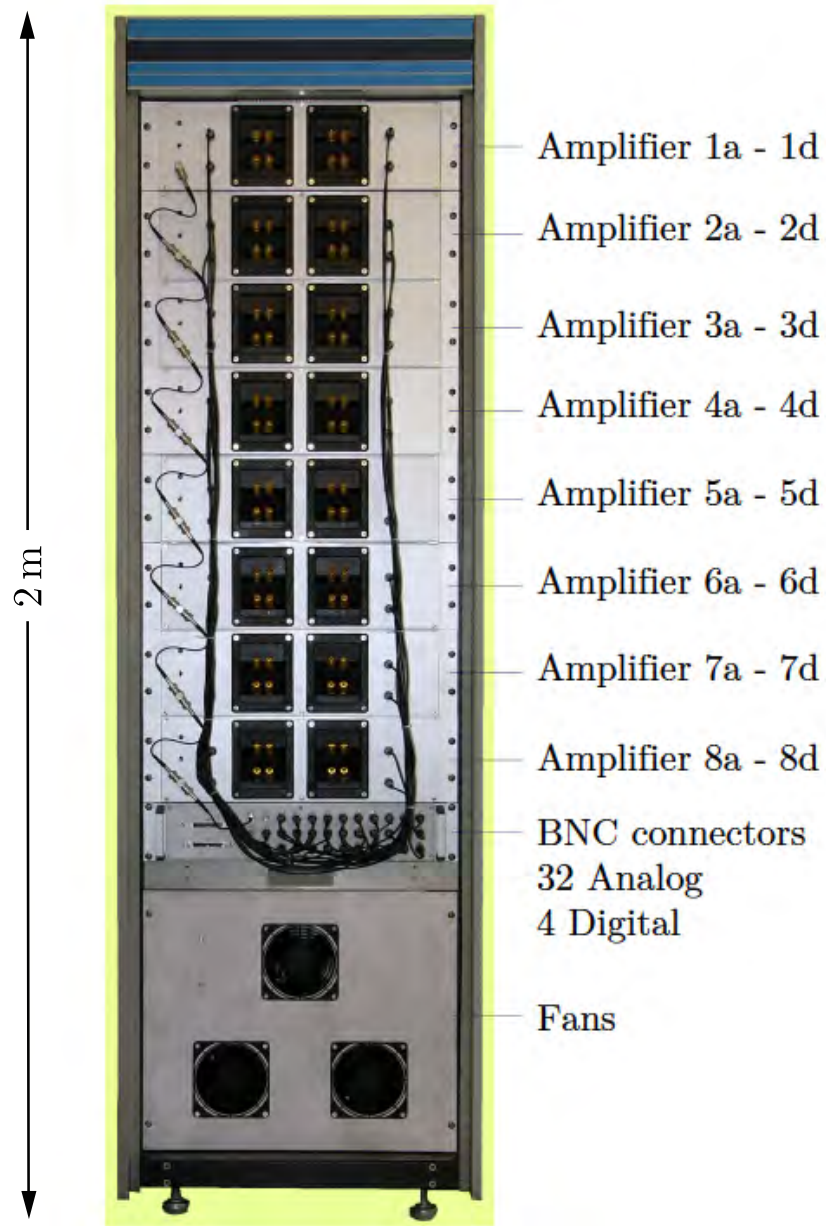


Figure 2.9: The amplifier unit.

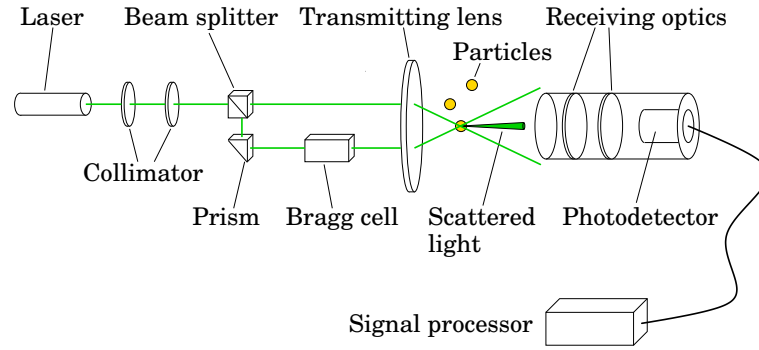


Figure 2.10: A schematic of a laser Doppler velocimeter.

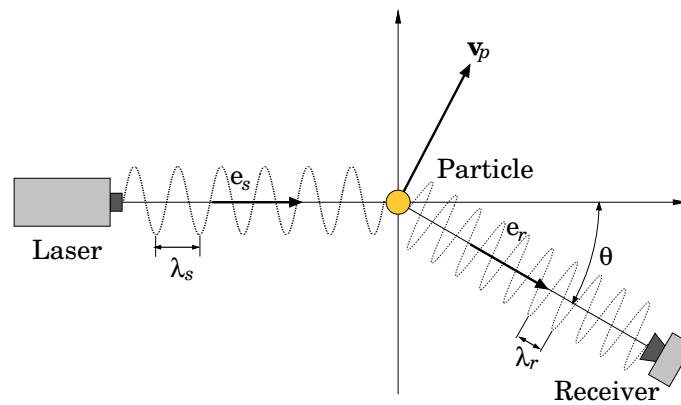


Figure 2.11: The figure illustrates the change in received frequency caused by the motion of the particle in a single-beam scattering process.

2.2.1 The Doppler model

The first explanation is based on the Doppler effect. Consider the scenario in figure 2.11, in which a stationary monochromatic light source with wavelength λ_s and frequency ν_s impinges on a particle moving with velocity \mathbf{v}_p in the flow. Denoting the Doppler frequency perceived by the particle as ν_p , we have

$$\nu_p = \nu_s \left(1 - \frac{\mathbf{e}_s \cdot \mathbf{v}_p}{c} \right), \quad (2.9)$$

where \mathbf{e}_s is the unit wave vector of the incident beam and c is the speed of light. Invoking the Doppler effect a second time, the frequency received by a

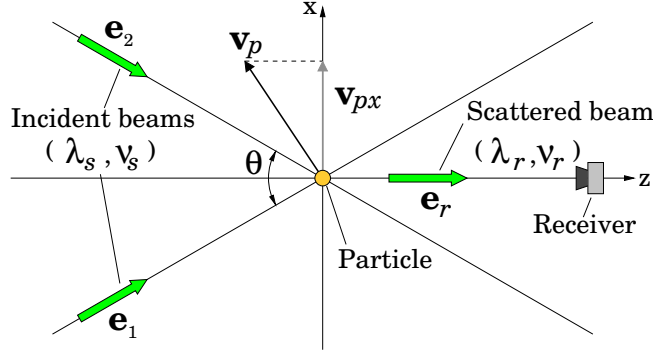


Figure 2.12: The figure illustrates the dual-beam scattering process.

stationary detector is

$$\nu_r = \frac{\nu_p}{1 - \mathbf{e}_r \cdot \mathbf{v}_p/c} = \nu_s \left(\frac{1 - \mathbf{e}_s \cdot \mathbf{v}_p/c}{1 - \mathbf{e}_r \cdot \mathbf{v}_p/c} \right), \quad (2.10)$$

where \mathbf{e}_r is the unit wave vector of the scattered beam at the receiver's end. For typical turbulent flows, the particle speed is much less than the speed of light. Thus, we have for the expression in equation 2.10 the Taylor expansion

$$\nu_r = \nu_s + \frac{\mathbf{v}_p \cdot (\mathbf{e}_r - \mathbf{e}_s)}{\lambda_s} \quad (|\mathbf{v}_p| \ll c, c = \lambda_s \nu_s). \quad (2.11)$$

For typical flow velocities (1~100 m/s), the Doppler shift frequency is of the order 1 MHz to 100 MHz, and is contained in the light frequency, which is approximately 10^{14} Hz. To resolve this small fraction of Doppler shift from the light source is technically challenging, if not at all impossible; see Paul and Jackson (1971). In order to make the Doppler frequency lie in a more manageable range, two coherent laser beams of equal intensity and wavelength are used instead of one. Figure 2.12 shows the dual-beam scattering process. When a particle moves across the measurement volume formed at the intersection of the two beams, it scatters light from both beams, each with a frequency

$$\nu_1 = \nu_s + \frac{\mathbf{v}_p \cdot (\mathbf{e}_r - \mathbf{e}_1)}{\lambda_s}, \quad \nu_2 = \nu_s + \frac{\mathbf{v}_p \cdot (\mathbf{e}_r - \mathbf{e}_2)}{\lambda_s}. \quad (2.12)$$

The light is focused and mixed on the detector to yield the beat frequency

$$\nu_B = \nu_2 - \nu_1 = \frac{\mathbf{v}_p \cdot (\mathbf{e}_1 - \mathbf{e}_2)}{\lambda_s}. \quad (2.13)$$

If the angle formed by the intersection of the two beams is denoted by θ , and the component of particle velocity perpendicular to the bisector of the beams (the z -axis) is denoted by v_{px} , then the beat frequency can be expressed as

$$\nu_B = \frac{2 \sin(\theta/2)}{\lambda_s} |v_{px}|. \quad (2.14)$$

Thus, the frequency difference is linearly proportional to the velocity component perpendicular to the bisector of the two beams.

2.2.2 The fringe model

The expression in equation 2.14 is derived largely based on kinematic consideration and it does not explain the origin of the beat frequency. The fringe model fills this gap of our understanding. We illustrate it using the configuration in figure 2.12. If two incident beams of equal amplitude E_0 and frequency ω_s , and linearly polarized perpendicular to the plane in which the two beams lie, then the electric field of each beam at an arbitrary point \mathbf{r} in space is described by

$$\mathbf{E}_1 = \mathbf{e}_y E_0 \exp(i[\omega_s t - \mathbf{k}_1 \cdot \mathbf{r} + \phi_1]), \quad (2.15)$$

$$\mathbf{E}_2 = \mathbf{e}_y E_0 \exp(i[\omega_s t - \mathbf{k}_2 \cdot \mathbf{r} + \phi_2]). \quad (2.16)$$

\mathbf{k}_1 and \mathbf{k}_2 are the wave vectors of the two beams, given by

$$\mathbf{k}_1 = k_s \mathbf{e}_1, \quad \mathbf{k}_2 = k_s \mathbf{e}_2, \quad k_s = 2\pi/\lambda_s. \quad (2.17)$$

ϕ_1 and ϕ_2 are the initial phases of the waves at the origin, respectively. At the crossing of the two beams, the two electric fields add according to the superpo-

sition principle to give an intensity I proportional to

$$I \propto |\mathbf{E}_1 + \mathbf{E}_2|^2. \quad (2.18)$$

By substituting the expressions for the electric fields from equations 2.15, 2.16, and 2.17, we have for the intensity

$$I \propto 2 E_0^2 \left[1 + \cos \left(2 \pi \left(\frac{2 \sin(\theta/2)}{\lambda_s} \right) x - (\phi_1 - \phi_2) \right) \right]. \quad (2.19)$$

It can be seen that the electromagnetic wave intensity varies periodically in x , with a fringe spacing given by

$$\Delta x = \frac{\lambda_s}{2 \sin(\theta/2)}. \quad (2.20)$$

A particle of diameter $d_p \ll \Delta x$ passing through the intersection volume samples the local intensity of the interference pattern and produces a burst of flickering light. If Δt is the particle's fringe crossing time, then the frequency of flickering is given by

$$\nu_{\text{detector}} = \frac{1}{\Delta t} = \frac{2 \sin(\theta/2)}{\lambda_s} \frac{\Delta x}{\Delta t} = \frac{2 \sin(\theta/2)}{\lambda_s} |\mathbf{v}_{px}|, \quad (2.21)$$

which is precisely equation 2.14. The fringe model offers a very physical and intuitive approach for understanding the laser Doppler technique. This model is only valid when the particle diameter is less than the wavelength of light. For particles larger than the wavelength of light, the arguments have to be modified in order to take into account the additional phase shift due to wave propagation inside the particles. This additional phase shift only causes the fringe pattern to be shifted in phase and equation 2.21 remains valid. The reader is referred to chapter 2 of Albrecht et al. (2003) for a full account of the particle finite size effect.

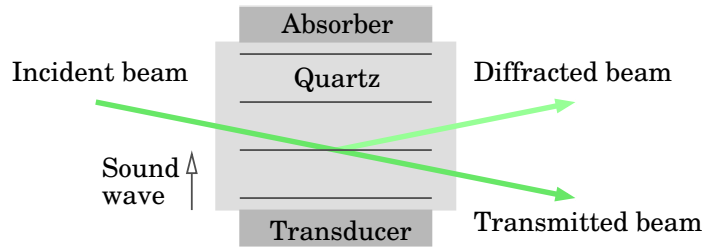


Figure 2.13: A schematic of a Bragg cell. A transducer generates an acoustic wave, resulting in a moving periodic refractive index grating that diffracts the incident light similar to in Bragg diffraction. The arrow points in the direction of travel of the acoustic wave.

2.2.3 The Bragg cell

The reader may note that particles with equal, but opposite velocities, moving across the measurement volume formed in the dual beam arrangement will produce the same frequency of flickering. To resolve the particle velocity direction, a Bragg cell is placed in one of the beam paths to modify the Doppler frequency. It consists of a mechanical oscillator, such as a piezoelectric transducer, attached to an optically transparent material, such as quartz. An oscillating electric field drives the transducer to vibrate, emanating a traveling acoustic wave. Under the mechanical pressure of the wave, a periodic refractive index grating results. This traveling periodic grating diffracts the incident light much like the atomic planes of a crystal in Bragg diffraction.

If a Bragg cell is placed in the path of beam 1 in figure 2.12, the frequency of the incident beam is shifted by an amount ν_{sh} to $\nu_1 + \nu_{sh}$ when the acoustic wave moves toward the beam, and $\nu_1 - \nu_{sh}$ when the acoustic wave moves away from the beam. In the fringe model, the first case corresponds to a movement of the fringes in the $-x$ direction, whereas the second case corresponds to a movement of the fringes in the $+x$ direction. The light from beam 1 and 2 is mixed on the

detector to yield a beat frequency

$$\nu_B = \begin{cases} \nu_{\text{sh}} + \frac{2 \sin(\theta/2)}{\lambda_s} \mathbf{e}_x \cdot \mathbf{v}_p & \text{fringes move in the } -x \text{ direction,} \\ \nu_{\text{sh}} - \frac{2 \sin(\theta/2)}{\lambda_s} \mathbf{e}_x \cdot \mathbf{v}_p & \text{fringes move in the } +x \text{ direction.} \end{cases} \quad (2.22)$$

It is easily seen that a stationary particle will yield a signal with frequency ν_{sh} , a movement in the direction of the fringes a lower frequency, and a movement against the fringes a higher frequency.

Figure 2.14 shows an overview of the TSI LDV system used in our investigation. An argon ion laser by Coherent (Innova 90C-5) provided a multi-colored beam. A multicolor beam separator (TSI Model 450200), converted the beam into three beam pairs of different wavelengths: green, blue, and violet. A Bragg cell in the beam separator shifted one in each beam pair by 40 MHz. Two fiberoptic probes focused the light from the beams to form a measurement volume. One probe measured two components, and the other one only one component, of the velocity of individual particles that passed through the approximately ellipsoidal measurement volume, which measured

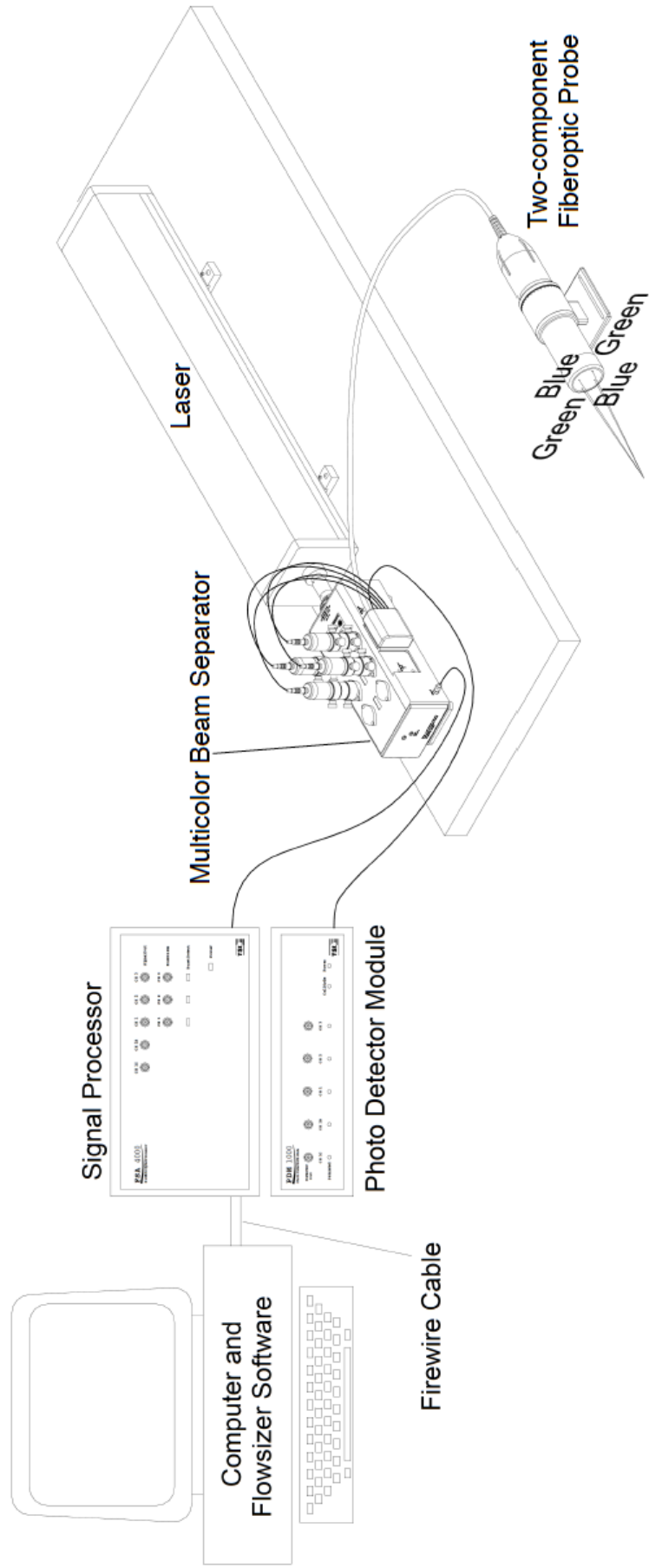


Figure 2.14: An overview of a TSI LDV system. Figure adapted from TSI LDV/PDPA system installation manual, page 73.

100 μm in diameter and 2 mm in length. The effect of a finite measurement volume on the measurement of particle velocity is discussed in greater detail in section 2.2.5. This resolution, however, was sufficient to resolve scales larger than the dissipation scale of the turbulence in this experiment. A receiving fiber in the probe collected light scattered by particles in the volume and sent the light to a photodetector (PDM 1000). The photodetector converted the scattered light into electrical signal which was then sent to a signal processor (FSA 4000). The signal processor extracted Doppler frequency information from the electrical signals and sent the digitized signal to be analyzed by software (FLOWSizer™) on a computer for data acquisition, yielding a single velocity measurement. Data consisted of a stream of velocity samples with irregular time intervals between them. The mean data rate was between 300 and 3000 samples per second, depending on the probe. For statistical convergence, we typically collected 2×10^6 data points per aspect ratio of the forcing and per spatial position of the probes.

2.2.4 Data processing

In LDV measurement, the flow velocity is sampled in time by random passages of particles that go through the measurement volume. This has two consequences. First, the velocity samples are irregularly spaced in time. Second, the measurement volume is sampled by high-speed particles more often than low-speed ones. As a consequence, even if the particle spatial distribution is independent of the velocity field, the rate of particle arrival at the measurement volume is correlated with the velocity field (McLaughlin and Tiederman, 1973). Without careful attention to this latter fact, statistical average of flow quantities can be biased. Thus, velocity samples must be weighted by appropriate statis-

tical factors to yield unbiased statistical averages (McLaughlin and Tiederman, 1973). The statistical factor we used for correcting single-point statistics is the arrival time weighting factor (see e.g. Adrian and Yao, 1987). Other methods may also work (see e.g. Buchhave, 1975; Buchhave et al., 1979; McDougall, 1980), but the arrival time method has the advantage of being computationally efficient and is well-suited for non-homogeneously seeded flow fields.

The method works by weighting the observables with the arrival times between particles. For example, the estimator for the mean and the RMS fluctuations are

$$\langle v \rangle = \frac{\sum_{i=1}^N v_i (t_i - t_{i-1})}{\sum_{i=1}^N t_i - t_{i-1}}, \quad (2.23)$$

$$\langle u'^2 \rangle = \frac{\sum_{i=1}^N (v_i - \langle v \rangle)^2 (t_i - t_{i-1})}{\sum_{i=1}^N t_i - t_{i-1}}, \quad (2.24)$$

where N is the total number of velocity samples. As noted by Albrecht et al. (2003), this method is suitable for moment estimation of single point statistics but fails for estimation of correlation functions. Therefore, we did not apply this method to our two-point correlation measurements, and we did not take any measures to correct for possible bias in our two-point correlations.

Because different probes record slightly different particle arrival times, in order to calculate two-point statistics, one must look for coincidences of velocity samples coming from these probes. We found these coincidences by discretizing the velocity time series using a slotting technique (Mayo et al., 1974) and searched for samples coming from each of the two probes with time separations falling within a given temporal bin, Δt , of duration 0.5 ms. This duration was chosen because it maximized both the number of coincidences and the value of the velocity autocorrelations (see section 7.1) near zero separation while keeping the value of the structure functions near zero separation small (see figures 2.15,

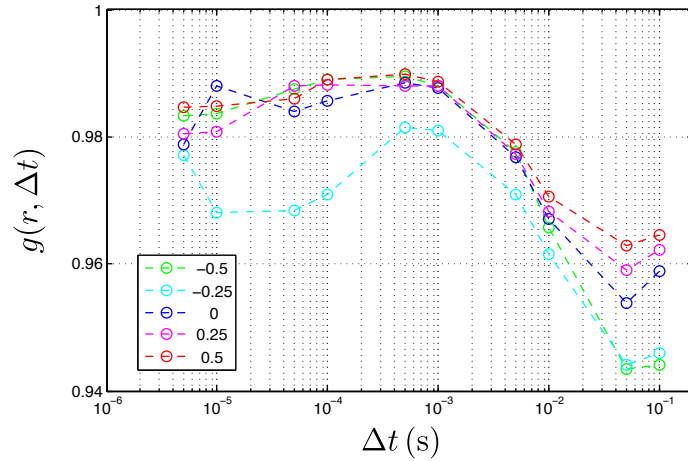


Figure 2.15: The effect of temporal binning on the value of the velocity correlation, $g(r)$, near zero separation. The values in the legend are the separations in millimeters.

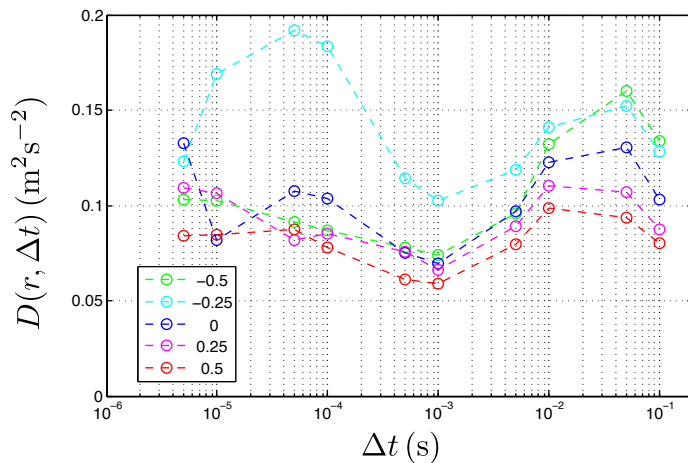


Figure 2.16: The structure function as a function of temporal bin width. For legend, see previous figure.

2.16, and 2.17). We typically collected about $10^4 - 10^5$ velocity samples.

For each of the two probes, an average was taken of velocity signal coming from the same probe falling within Δt . The product of all averaged velocity pairs was then added to a sum. After processing the entire temporal sequence,

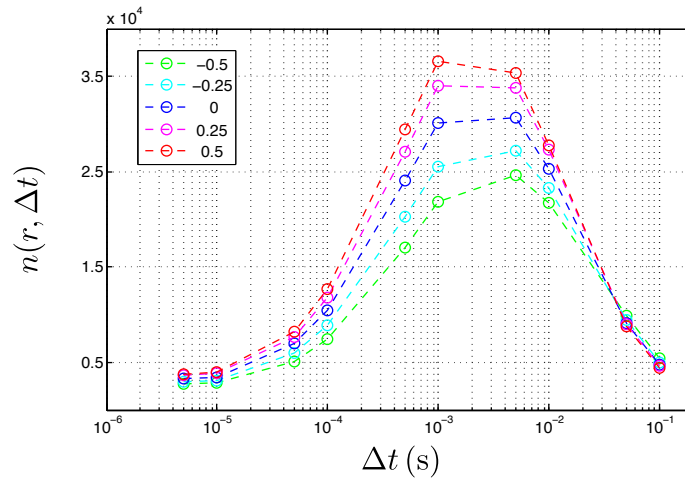


Figure 2.17: The number of samples yielding the velocity correlation as a function of temporal bin width. For legend, see figure 2.15.

the total sum was divided by the number of accumulated products, giving us the value of the velocity autocorrelation for that given spatial separation. We found that so long as Δt was smaller than 15 ms, the difference in the values of the correlation was less than 1%, as shown in figure 2.15.

By definition, the velocity correlation is unity at zero separation. Noise, however, may contaminate the data and mask the true value of the correlation at zero separation. In order for the correlation to comply with this definition, we normalized the velocity correlation with its value at zero separation. The measured structure functions could have been corrected to yield better accuracy at the smaller separations, but since the measured structure functions had leveled off at the low end (see figures 5.1 and 5.3), and correction of any data is never a satisfying proposition, no matter how carefully executed, because in some sense it presumes the answer, therefore no attempt was made to apply corrections to these measurements, but they may be required in some future investigation. It can certainly be said that the uncorrected data were internally consistent and the

inertial scale measurements were done with sufficient accuracy that no special correction needed to be developed.

2.2.5 Limitations of the LDV technique

In addition to the bias discussed in 2.2.4, other physical parameters may limit the accuracy of LDV. We review these limitations in the following by dividing them into those arising from the flow and those arising from measurement instruments.

Tracer particles

The motion of an individual spherical particle in a turbulent flow has been extensively studied (see e.g. Corrsin and Lumley, 1956; Manton, 1977; Maxey and Riley, 1983), and the response of a tracer particle to isotropic turbulence has been examined by Mei (1996). In making accurate velocity measurements of a fluid with LDV, we require the velocity of the tracer particle be close to the local, instantaneous fluid velocity. The particle inertial effects are described by the Stokes number

$$\text{St} = \frac{\tau_p}{\tau_\eta}, \quad (2.25)$$

where τ_p is the particle response time defined as

$$\tau_p = \frac{1}{18} \left(\frac{\rho_p}{\rho_f} \right) \left(\frac{D^2}{\nu} \right), \quad (2.26)$$

where ρ_p , ρ_f , D , and ν are the particle density, the density of the fluid, the particle diameter, and the fluid viscosity, respectively. τ_η is the Kolmogorov time defined in equation 1.10. Buchhave et al. (1979) considered the particle-fluid

relative velocity, using a model by Lumley (1976), and estimated an upper limit of the particle Stokes number of $St \leq 1/74$ with the criterion that the error in the velocity be less than 1%. We used oil droplets (density 0.9 g cm^{-3}) as tracer particles in air (density 1.2 kg m^{-3}), generated by a Palas AGF 10.0 aerosol generator. The droplets had a most probable diameter of about $3 \text{ }\mu\text{m}$. They settled in air at $200 \text{ }\mu\text{m s}^{-1}$. The Stokes number based on the most probably diameter was about 0.02, the smallness of which qualifies these oil droplets as passive tracers (see e.g. Bewley et al., 2008).

A second problem connected to seeding the fluid with particles is turbulence modification due to particle-fluid interaction. This is an area of active research (see e.g. Hestroni, 1989; Elghobashi and Truesdell, 1993). The addition of particles at a volume fraction of as low as 10^{-5} to a turbulent flow modifies its motion (Elghobashi, 1994). For low values of particle volume fraction ($\leq 10^{-6}$) the particles have negligible effect on the flow (Elghobashi, 1994). The oil droplets used in our experiment were present at a volume fraction of less than 10^{-7} . This particle concentration was too small to alter the turbulence.

The effect of refractive index fluctuations

Since the laser beams of the LDV probes must propagate through a medium having random index of refraction fluctuations, the beam paths will no longer be straight, but will take on random fluctuating passages through the medium, and the phase and amplitude of the receiving signal will fluctuate randomly. The fluctuations in the index of refraction are primarily due to pressure fluctuations and temperature fluctuations in the medium. Buchhave et al. (1979) estimated that, by considering an isentropic variations in the pressure in a com-

compressible flow and assuming a quasi-Gaussian relationship between pressure and velocity fluctuations, a root-mean-square (RMS) velocity fluctuations of the order of 70 m s^{-1} are necessary to produce significant changes in the index of refraction. For temperature fluctuations, they obtained an estimate for the rate of decrease of index of refraction with temperature of the order of $1 \times 10^{-6} \text{ K}^{-1}$ for air at 273 K. Since the typical velocity fluctuations in our experiment was 1 m s^{-1} ($\ll 70 \text{ m s}^{-1}$), and the rate of change of index of refraction with temperature is small, we can neglect the effect of index-of-refraction fluctuations.

The probe volume size

The probe volume is defined by the surface on which the light intensity of the fringes is $1/e^2$ of the maximum intensity in the beam intersection region. With Gaussian beams the probe volume is an ellipsoid, and we have the expression for the probe volume dimensions in terms of the principal diameters of the ellipsoid in the coordinate system defined in figure 2.18:

$$d_x = \frac{d_0}{\cos \kappa}, \quad (2.27)$$

$$d_y = d_0, \quad (2.28)$$

$$d_z = \frac{d_0}{\sin \kappa}, \quad (2.29)$$

where d_0 , the width of the waist of the focused beam, is

$$d_0 = \frac{4 \lambda f}{\pi a}, \quad (2.30)$$

for λ , the wavelength of the light, f , the focal length of the transmitting lens, and a , the diameter of the beam. For our LDV system, the probe volume formed by the two beams of wavelength $\lambda = 514.5 \text{ nm}$ had the largest dimension. Each beam had a diameter of 3.5 mm, and for our optics, $f = 512 \text{ mm}$, $\kappa = 2.8^\circ$,

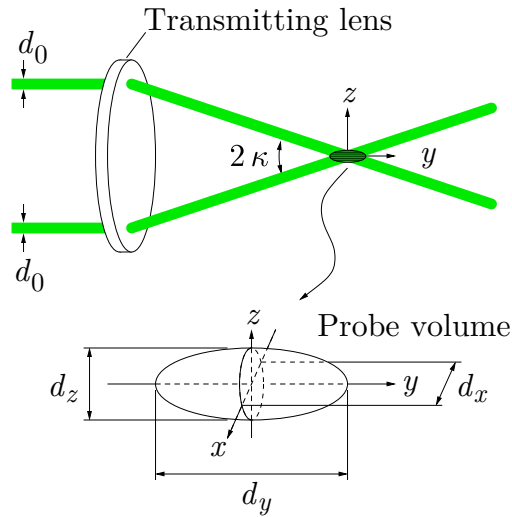


Figure 2.18: The schematic shows the LDV probe volume dimensions.

the probe volume dimensions were $d_x \approx d_y \approx 96 \mu\text{m}$, and $d_z = 1.97 \text{ mm}$. In order to resolve the smallest length scales in the flow, we required that any of the three probe volume linear dimension be smaller than the Kolmogorov scale, η (see equation 1.9). Our probe volume dimensions were $d_x \approx 0.6 \eta$, $d_y \approx 0.6 \eta$, and $d_z \approx 12 \eta$ (see table 4.2 for values of η in the experiment). Thus, our optical setup had not met this condition but it had sufficient dynamic range to resolve the intermediate and the very large scale motion.

CHAPTER 3

THE EXPERIMENTAL PROCEDURE

Here we describe the coordinate system we used to present our results. We describe the measurement protocol that exploited the symmetry of the flow generation system to rotate the turbulence relative to our LDV measurement apparatus. We discuss the quantity we fixed when comparing flows with different values of the forcing anisotropy.

3.1 The coordinate system

The turbulence coordinate system was not fixed to the laboratory frame, (x_1, x_2, x_3) , as is shown in figure 3.1, but was fixed to the turbulence symmetry axis. Because the turbulence was axisymmetric, it had two principal axes; one being the axis of symmetry of the forcing, and the other one, a radial axis, perpendicular to it. However, as described in 3.2, our measurement apparatus measured particle velocities only at points that lie along a straight line fixed in the laboratory frame. In order to sample the statistics of turbulence along both axes, we rotated the axis of symmetry of the turbulence by taking advantage of the symmetries of the flow apparatus.

The two orientations of the symmetry axis in the laboratory frame are shown as x'_1 and x'_3 in figure 3.1, each of which passes through the centers of opposite hexagonal faces of the flow apparatus. The x'_1 axis was nearly parallel to the line along which we collected velocity samples, x_1 , and it lay along $\theta = 107^\circ$ and $\phi = -4^\circ$. The x'_3 axis lay along $\theta = 4^\circ$ and $\phi = 180^\circ$, and was close to the x_3 axis. These two axes, x'_1 and x'_3 , were also nearly perpendicular and

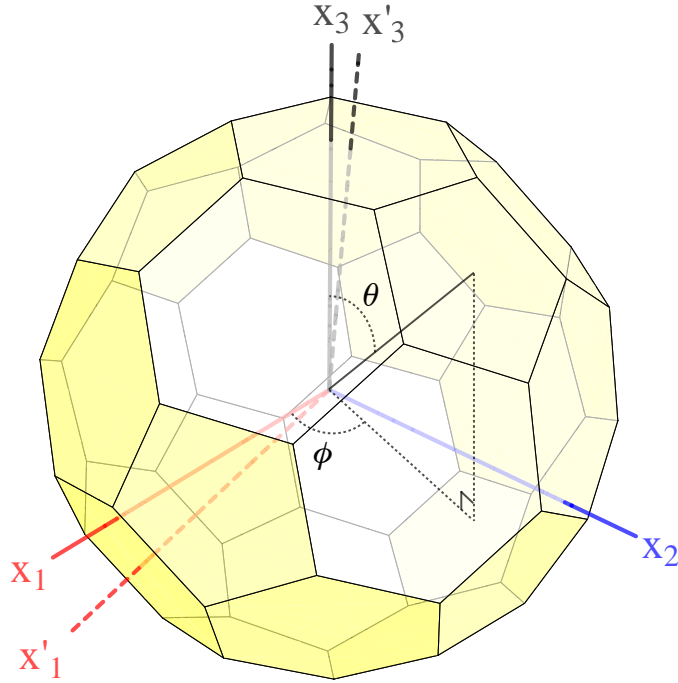


Figure 3.1: The schematic shows the coordinate system in the laboratory frame. x_3 was aligned with the vertical. The axis of symmetry of the forcing lay along either x'_1 or x'_3 , depending on the configuration. Our measurements were made at points lay along x_1 .

parallel to the vertical axis, respectively. We assume that the two orientations are equivalent because the acceleration of gravity is negligible relative to particle accelerations in the turbulent field (see e.g. Voth et al., 2002). Because the primed and unprimed coordinate systems are close to each other, we do not distinguish between them in the rest of this thesis.

Figures 3.2(a) and (b) show the coordinate system, (r_1, r_2, z) , which was aligned with the symmetry axis of the forcing, z . The two orientations of the forcing coordinate system with respect to the laboratory frame correspond to the two cases described above. Hereafter, 'axial' refers to both the direction of

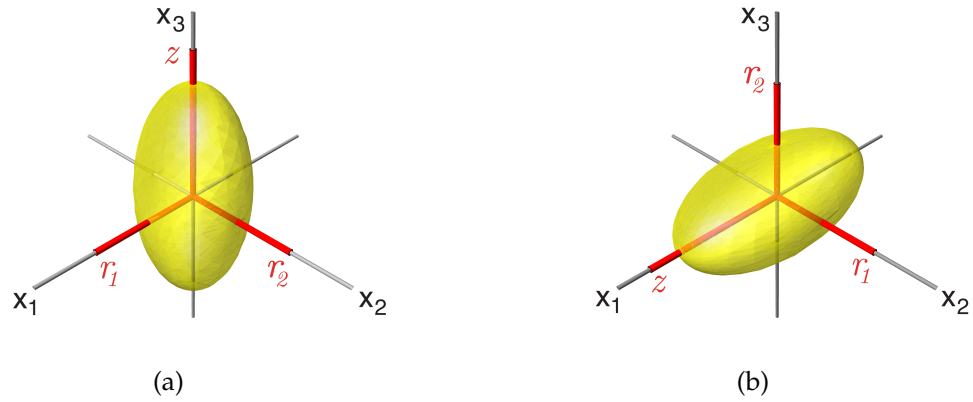


Figure 3.2: The figure shows the orientations of the body coordinate system (in red) of the forcing (ellipsoidal surface in yellow) with respect to the laboratory frame (gray), and the conventions we used: (a) when the axis of symmetry of the forcing lay close to the x_3 axis of the laboratory frame, and (b) when the axis of symmetry lay close to x_1 axis of the laboratory frame. The coordinate system (x_1, x_2, x_3) was fixed in the laboratory frame, and the coordinate system (r_1, r_2, z) was fixed with respect to the symmetry of the forcing.

the particle velocity component measured along the axis of symmetry, and, in discussing two-point statistics, separations along the axis of symmetry. Likewise, ‘radial’ refers to both the direction of the particle velocity components normal to the axis of symmetry, and to separations normal to the axis of symmetry. Additionally, we refer to two-point quantities whose separation vector lies along the axis of symmetry as axial quantities, and those with radial separations as radial quantities. For example, a two-point quantity $f(x_1)$ is denoted as $f(z)$ when the axis of symmetry of the forcing lies along x_1 , and is called an axial quantity. In keeping with the geometry described above, our ‘axial’ measurements were in reality about 15° away from the axis of symmetry, and the ‘radial’ measurements were about 4° from its normal. Our results do not depend on the angle between the ‘axial’ and ‘radial’ measurements.

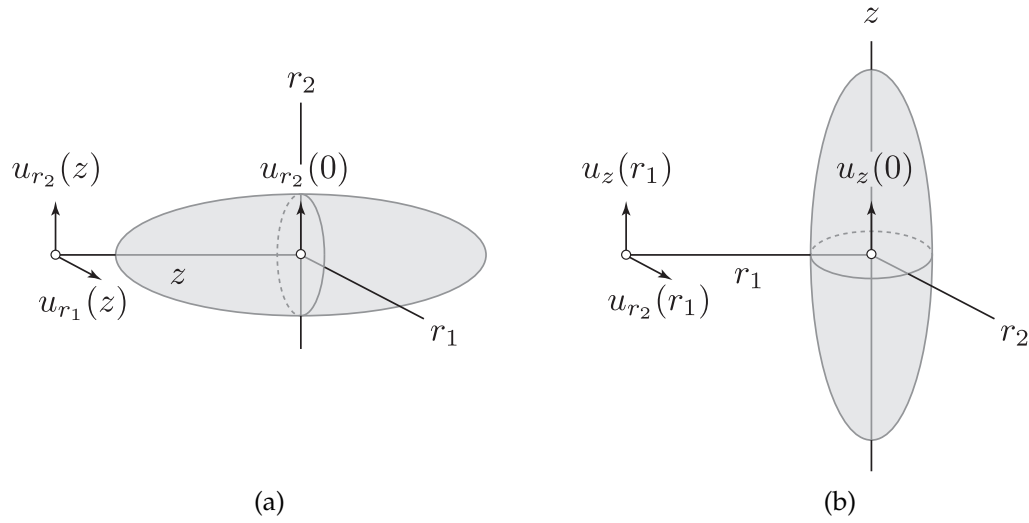


Figure 3.3: The figure shows the orientations of the measured velocity components with respect to the forcing coordinate system when the separation vector lay (a) along the axis of symmetry, or (b) perpendicular to the axis of symmetry.

3.2 The measurement protocol

We used the LDV probes in two configurations. In one configuration, all three orthogonal components of the fluid velocities were measured at a single point. For these measurements, the probes observed a fixed volume (aligned to within $10\ \mu\text{m}$ with a pin hole) close to the center of the soccer ball, which is the point $(0, 0, 0)$ in the laboratory frame shown in figure 3.1. One probe measured a single component of the fluid velocities, namely $u_{x_1}(0, 0, 0)$. The second probe measured two orthogonal components of the fluid velocities, namely $u_{x_2}(0, 0, 0)$ and $u_{x_3}(0, 0, 0)$. In the second configuration, we aligned the probes in a similar way, except that we positioned the two-component probe at different points along the x_1 axis, using a programmable linear traverse. This probe now measured $u_{x_2}(x_1, 0, 0)$ and $u_{x_3}(x_1, 0, 0)$. In addition, the single-component probe was rotated by 90° to measure $u_{x_3}(0, 0, 0)$, which was coincident with one of the components measured by the two-component probe when x_1 equaled zero. These

velocity components, expressed in the (r_1, r_2, z) coordinate system, are shown schematically in figure 3.3. The two orientations of the forcing coordinate system relative to the laboratory frame are described in figure 3.1.

3.3 Methods

We collected two data sets for each of a series of forcing anisotropy, A , given by equation 2.8. For one data set, the axis of symmetry of the forcing was aligned close to x_3 , and for the other, the symmetry axis was aligned close to x_1 . For each value of the forcing anisotropy, and each orientation of the forcing symmetry axis, data were collected with the two-component LDV probe positioned at various locations along the x_1 -axis. We varied the forcing anisotropy while fixing the turbulent kinetic energy in the center of the soccer ball

$$K = \frac{1}{2} \left[\langle u_{x_1}'^2(0, 0, 0) \rangle + \langle u_{x_2}'^2(0, 0, 0) \rangle + \langle u_{x_3}'^2(0, 0, 0) \rangle \right], \quad (3.1)$$

where u_{x_i}' is the RMS fluctuations of the fluid velocity in the x_i direction, and $\langle \dots \rangle$ denotes temporal averaging.

CHAPTER 4

THE FLOWS

In this chapter, we evaluate the quality of the flows generated by the turbulence apparatus introduced in chapter 2. Three-dimensional velocity measurements made at single points in the center region of the flow apparatus show that the anisotropy of the turbulent velocity RMS fluctuations followed the anisotropy of the forcing signal. Two-point velocity measurements made at points that lay along a single line in the laboratory frame show that the flows were approximately homogeneous and axisymmetric. For the case of spherically symmetric forcing, with $A = 1$ (see equation 2.8), we expected and indeed found that the turbulence was isotropic. In all cases, the mean velocities were less than 0.24 ms^{-1} , or less than 23% of the fluctuations and the shear stresses were less than 7% of the turbulent kinetic energy, as shown in table 4.2.

4.1 Anisotropy of the fluctuations

Figure 4.1 shows the ratio of axial to radial velocity fluctuations as a function of the forcing anisotropy, A . It is evident that the anisotropy of the turbulence followed the variation of A . In addition, the anisotropy was nearly the same whether measured in the r_1 or r_2 directions. Therefore, the turbulence was close to cylindrical symmetric, though this was less so at extreme values of A . The loss of cylindrical symmetry might be explained by the decrease in the number of loudspeakers driving the turbulence as the value of A moved away from one. This is the nature of the forcing algorithm described in section 2.1.3. We think that, as the number of loudspeakers effectively decreased, the turbulence became more sensitive to mechanical differences between the loudspeakers, and

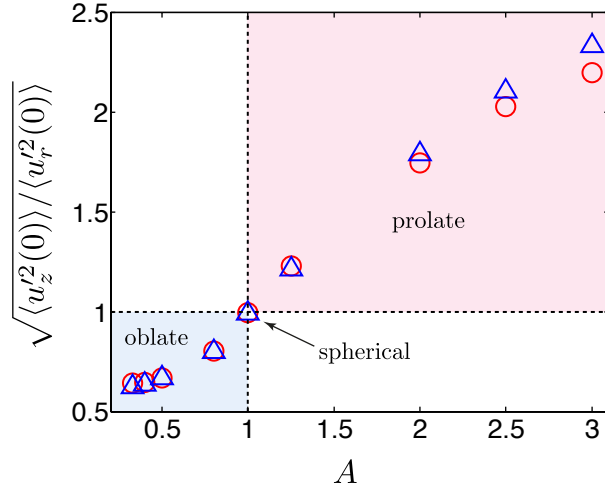


Figure 4.1: The velocity fluctuation ratios as a function of the forcing anisotropy, A . The circular symbols (\circ) are $\sqrt{\langle u_z'^2(0) \rangle / \langle u_{r1}'^2(0) \rangle}$ and the triangular symbols (\triangle) are $\sqrt{\langle u_z'^2(0) \rangle / \langle u_{r2}'^2(0) \rangle}$. Symbols in the region shaded in blue have oblate shape asymmetry, whereas those in the region shaded in red have prolate shape asymmetry. Spherical symmetry lies at the intersection of the two regions. Data are collected with the axis of symmetry lying along x'_3 . We obtained similar results (not shown) when the axis of symmetry lay along x'_1 .

to misalignments of the nozzles.

4.2 Axisymmetry of the fluctuations

Here, we characterize the degree to which the axisymmetry was spatially uniform. In figure 4.2(a), we examine the ratio of the two radial fluctuating velocities, $\sqrt{\langle u_{r2}'^2(0, 0, z) \rangle / \langle u_{r1}'^2(0, 0, z) \rangle}$, as a function of the distance from the center of the soccer ball along the axial direction for three values of the forcing anisotropy. Within 50 mm from the middle of the flow chamber, the values of this ratio deviated by less than 10% from the value 1, indicating that the turbulence was close to being cylindrically symmetric. To gauge the extent of spatial uniformity of the anisotropy, we plot in figure 4.2(b) the ratio of the axial fluctuating

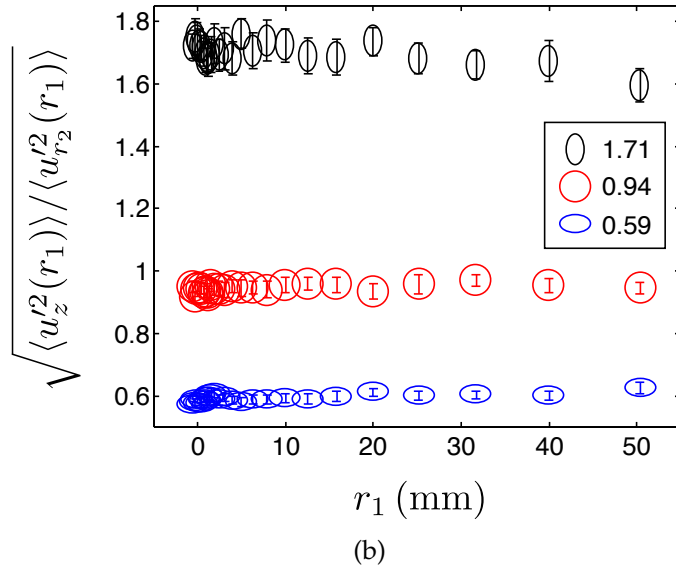
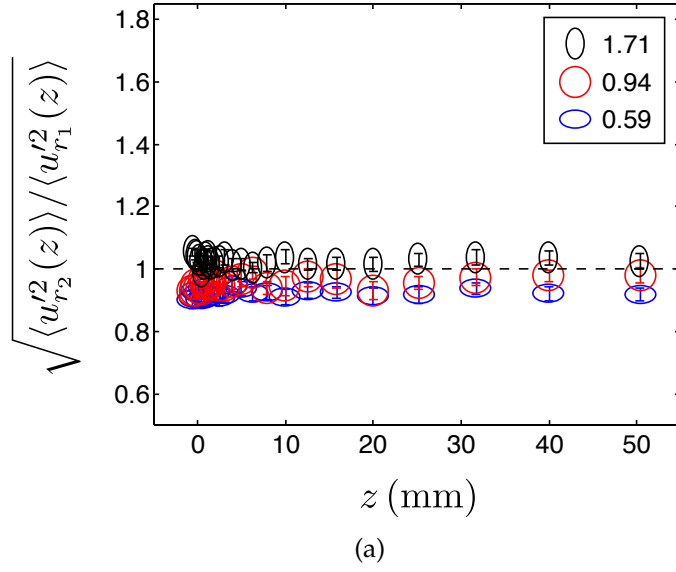


Figure 4.2: For three values of the anisotropy measured at the centre of the ball, $\sqrt{\langle u_z'^2(0) \rangle / \langle u_r'^2(0) \rangle}$, we plot (a) the ratio of the two radial components of the velocity fluctuations $\sqrt{\langle u_{r_2}'^2(0, 0, z) \rangle / \langle u_{r_1}'^2(0, 0, z) \rangle}$ and (b) the ratio of the axial fluctuations to the radial fluctuations, $\sqrt{\langle u_z'^2(r_1, 0, 0) \rangle / \langle u_{r_2}'^2(r_1, 0, 0) \rangle}$ at various points moving away from the center of the ball. The values in these legends, and in all others in this thesis, are those of the data in (b) for $r_1 = 0$.

velocity to one of the radial fluctuating velocities, $\sqrt{\langle u_z'^2(r_1, 0, 0) \rangle / \langle u_{r_2}'^2(r_1, 0, 0) \rangle}$, as a function of the distance from the center of the chamber. Here, the measurement points lie on a line nearly normal to the axis of symmetry, and the values of this ratio at $r_1 = 0$ correspond to the values shown in figure 4.1. Again, the velocity fluctuation ratio is approximately constant within 50 mm of the center of the chamber. Thus, we inferred that the degree of anisotropy was approximately uniform within a central spherical region with radius 50 mm. In both plots, the error bars were the standard errors of the measurements obtained by truncating the original data sets into 20 equal parts. They indicate the sampling accuracy and not the measurement accuracy. These error bars were always less than $\pm 8.5\%$. We concluded that, within the error bars, the ratios of the fluctuating velocities at different locations from the center of the soccer ball were indistinguishable from each other.

Since we take axial and radial measurements through the turbulence region, we obtained twice the information on the radial velocity. Thus, the ratio $\sqrt{\langle u_z'^2(0) \rangle / \langle u_r'^2(0) \rangle}$ in our experiment may be calculated in two different ways. The first one is the ratio of the two orthogonal velocity fluctuations in the limit as $r_1 \rightarrow 0$

$$u_z'/u_{r_2}' = \lim_{r_1 \rightarrow 0} \sqrt{\langle u_z'^2(r_1, 0, 0) \rangle / \langle u_{r_2}'^2(r_1, 0, 0) \rangle}, \quad (4.1)$$

and the second one is

$$u_z'/u_{r_2}' = \lim_{\substack{r_1 \rightarrow 0 \\ z \rightarrow 0}} \sqrt{\langle u_z'^2(r_1, 0, 0) \rangle / \langle u_{r_2}'^2(0, 0, z) \rangle}. \quad (4.2)$$

A	Eq.	0.33	0.4	0.5	0.8	1.0	1.25	2.0	2.5
u'_z (m s^{-1})	4.1	0.74 ± 0.01	0.75 ± 0.01	0.79 ± 0.01	0.91 ± 0.02	1.08 ± 0.02	1.21 ± 0.02	1.42 ± 0.04	1.47 ± 0.04
u'_{r_2} (m s^{-1})	4.1	1.26 ± 0.04	1.24 ± 0.03	1.27 ± 0.03	1.19 ± 0.03	1.15 ± 0.03	1.03 ± 0.03	0.83 ± 0.02	0.75 ± 0.02
u'_{r_2} (m s^{-1})	4.2	1.11 ± 0.02	1.09 ± 0.02	1.12 ± 0.02	1.08 ± 0.02	1.08 ± 0.02	1.04 ± 0.02	0.90 ± 0.02	0.84 ± 0.02
u'_z/u'_{r_2}	4.1	0.59 ± 0.03	0.60 ± 0.02	0.63 ± 0.03	0.77 ± 0.03	0.94 ± 0.04	1.17 ± 0.05	1.71 ± 0.10	1.97 ± 0.10
u'_z/u'_{r_2}	4.2	0.67 ± 0.03	0.69 ± 0.03	0.71 ± 0.03	0.85 ± 0.03	1.00 ± 0.04	1.16 ± 0.03	1.58 ± 0.09	1.76 ± 0.09

Table 4.1: For forcing anisotropy ratios (A) ranging from 0.33 to 2.5, the table shows the velocity fluctuation ratio according to the two limits discussed in the text (equations 4.1 and 4.2).

We calculated the ratio in each case by averaging the RMS velocity fluctuations at locations within 10 mm from the center of the chamber, and then taking the ratio between the axial and radial fluctuations. Their values are summarized in table 4.1. The variation in the fluctuations in this range was less than 5% and we used this variation for estimating the error in the velocity fluctuations. Our single-point statistics do not depend on this choice of the definition for the anisotropy ratio, and we discussed the results in terms of u'_z/u'_{r_2} defined in 4.1. The two-point correlation functions, as we will show in chapter 7, do depend on the anisotropy of the fluctuations and we discuss the results in terms of u'_z/u'_{r_2} defined in 4.2, since these are the velocity fluctuations associated with the radial and axial correlation functions.

4.3 Homogeneity of the fluctuations

To evaluate the homogeneity of the turbulent fluctuations, we present measurements of $\sqrt{\langle u'^2_{r_2}(0, 0, z) \rangle / \langle u'^2_{r_2}(0, 0, 0) \rangle}$ and $\sqrt{\langle u'^2_z(r_1, 0, 0) \rangle / \langle u'^2_z(0, 0, 0) \rangle}$ in figures 4.3. These ratios compare the amplitude of the velocity fluctuations at locations away from the center to those in the center of the chamber. The error bars were the standard errors of the measurements obtained by dividing the original data sets into 20 equal parts. Within a radius of 50 mm, the difference between $\sqrt{\langle u'^2_{r_2}(0, 0, z) \rangle / \langle u'^2_{r_2}(0, 0, 0) \rangle}$ and its value at the origin is within 5% of the value at the origin. The inequality also holds for $\sqrt{\langle u'^2_z(r_1, 0, 0) \rangle / \langle u'^2_z(0, 0, 0) \rangle}$. Thus, we conclude that the RMS fluctuations are homogeneous.

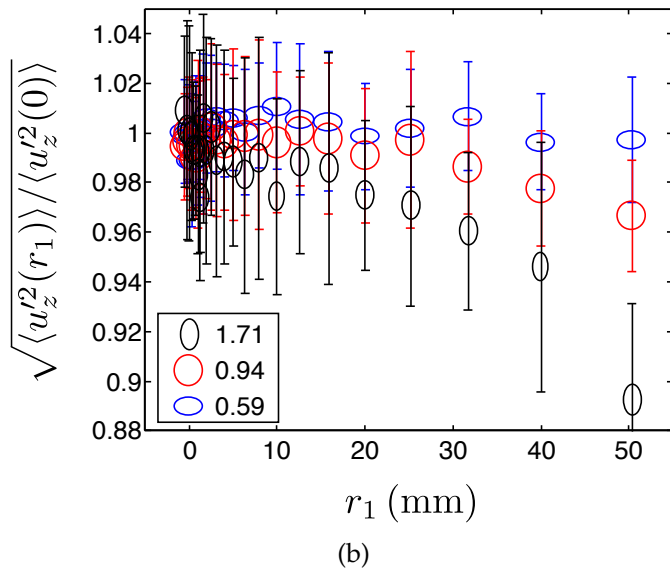
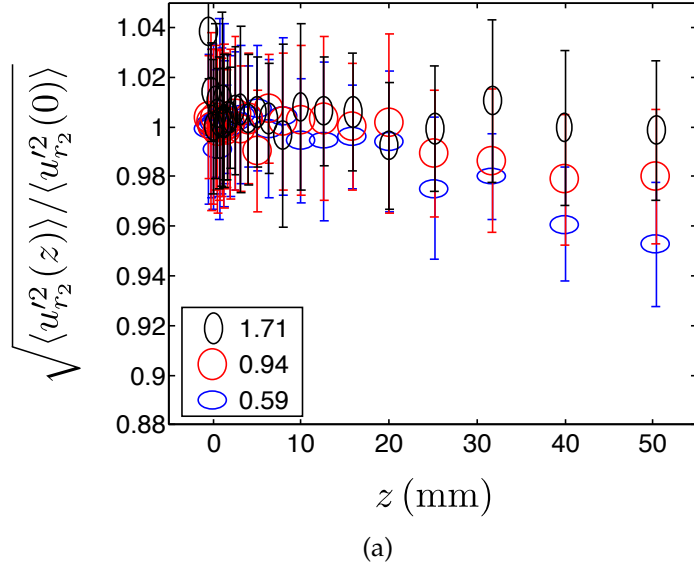


Figure 4.3: The comparison of fluctuations at various distances from the center of the soccer ball to those in the middle. (a) Radial fluctuations along axial separations, $\sqrt{\langle u_{r_2}^2(0, 0, z) \rangle / \langle u_{r_2}^2(0, 0, 0) \rangle}$, for anisotropy ratios, $\sqrt{\langle u_z^2(0) \rangle / \langle u_r^2(0) \rangle}$, ranging from 0.59 to 1.71. (b) Axial fluctuations along radial separations, $\sqrt{\langle u_z^2(r_1, 0, 0) \rangle / \langle u_z^2(0, 0, 0) \rangle}$, for the same range of anisotropy. The anisotropy ratios in the legend are measured at the center of the soccer ball.

4.4 Anisotropy of the mean flow

Because anisotropy can manifest itself not only in the fluctuations, but also through spatial variation of the mean velocity, we show in figure 4.4(a) and (b) the ratio of the mean flow velocity to the velocity fluctuations, $\langle U_{r_2}(0, 0, z) \rangle / \langle u_{r_2}'^2(0, 0, z) \rangle^{1/2}$ and $\langle U_z(r_1, 0, 0) \rangle / \langle u_z'^2(r_1, 0, 0) \rangle^{1/2}$. It is difficult to predict a trend in the data, but may indicate that the actual center of the turbulence was displaced from the center of our coordinate system. We concluded that the variation in the mean velocity was negligible because it was typically less than 10% of the fluctuations. Only at the extreme values of the anisotropy was the mean velocity as much as 15% of the fluctuations. This may have been due to the sensitivity of the turbulence to small differences between the loudspeakers in this range of anisotropies, as discussed in section 4.1.

4.5 Reflectional symmetry

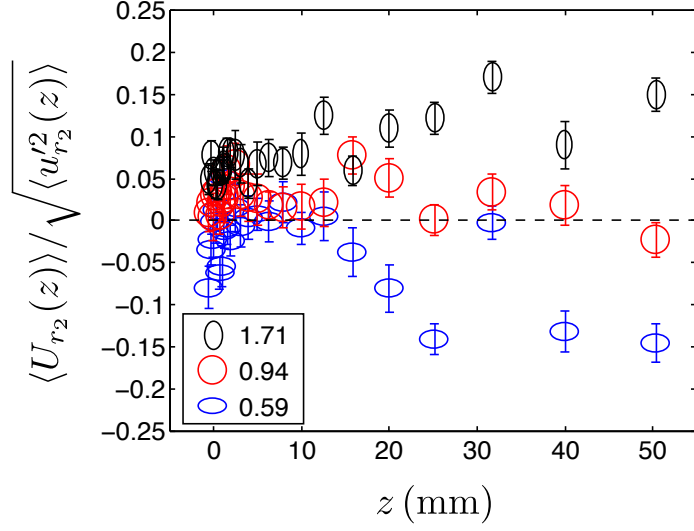
As described in section 1.6, reflectional symmetry in a plane containing the axis of symmetry implies that (e.g. Lindborg, 1995)

$$\chi_{r_1 r_2} = \frac{\langle u_{r_1}'(0, 0, z) u_{r_2}'(0, 0, 0) \rangle}{\sqrt{\langle u_{r_1}'^2(0, 0, z) \rangle \langle u_{r_2}'^2(0, 0, 0) \rangle}} = 0. \quad (4.3)$$

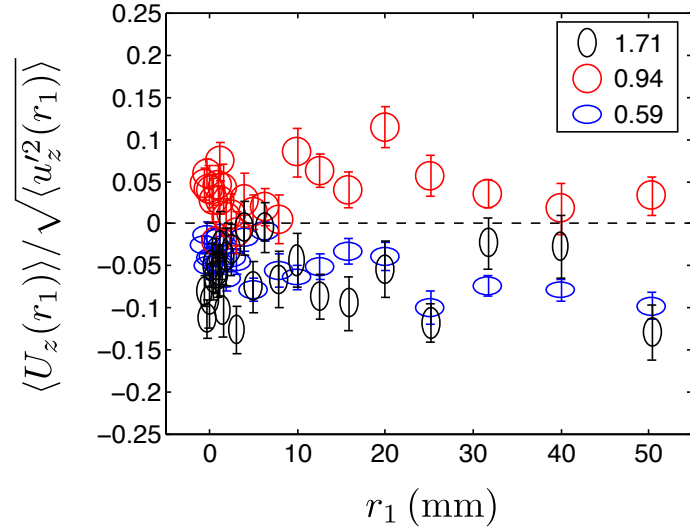
In addition, reflectional symmetry in a plane normal to the the axis of symmetry implies that

$$\chi_{z r_2} = \frac{\langle u_z'(r_1, 0, 0) u_{r_2}'(0, 0, 0) \rangle}{\sqrt{\langle u_z'^2(r_1, 0, 0) \rangle \langle u_{r_2}'^2(0, 0, 0) \rangle}} = 0. \quad (4.4)$$

The measurements of these correlations are shown in figure 4.5. The shape of the curves are difficult to interpret, but may suggest that the symmetry planes of the turbulence were slightly tilted from the plane of measurement. In both

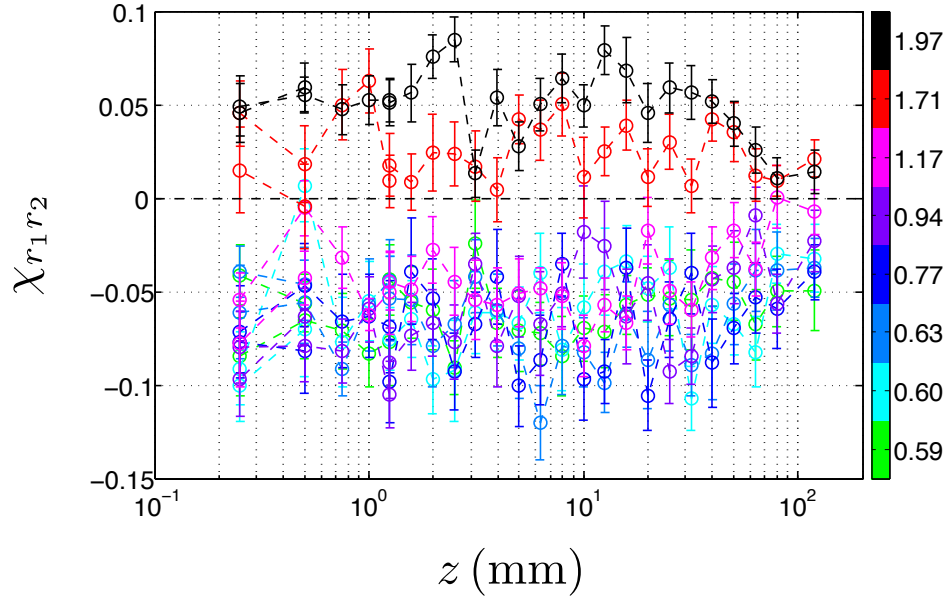


(a)

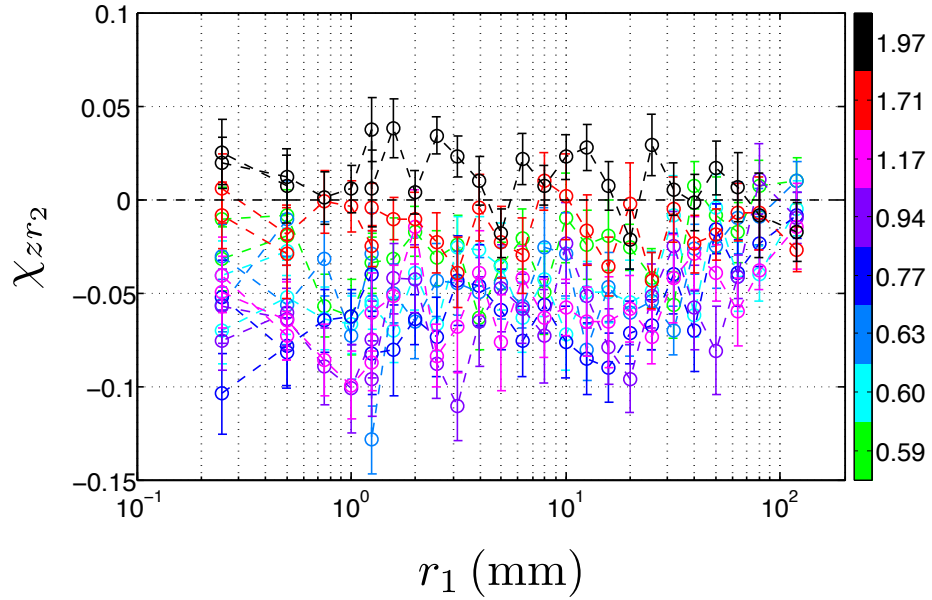


(b)

Figure 4.4: The mean flow as a fraction of the fluctuating velocity (a) $\langle U_{r_2}(0, 0, z) \rangle / \sqrt{\langle u_{r_2}^2(0, 0, z) \rangle}$, and (b) $\langle U_z(r_1, 0, 0) \rangle / \sqrt{\langle u_z^2(r_1, 0, 0) \rangle}$ for axial-to-radial velocity fluctuation ratios ranging from 0.59 to 1.71. The values in the legend are the anisotropy measured at the centre of the soccer ball.



(a)



(b)

Figure 4.5: The cross correlations of orthogonal velocity components at various distances from the center of the soccer ball (a) along the axis of symmetry, and (b) along an axis perpendicular to the axis of symmetry of the forcing. The values in the color bar are the anisotropy measured at the center of the soccer ball for various values of the anisotropy of the forcing.

plots, the error bars were the standard errors of the measurements obtained by truncating the original data sets into 20 equal parts. These errors were always less than $\pm 3\%$. We do not believe that the trend and the scatter in the data were significant enough to be the basis of a theory. Because the variation in the cross correlations was always less than 10% (the mean was no more than 5%), we concluded that the turbulence possessed remarkable reflectional symmetries

4.6 Reynolds shear stresses

Two observations of turbulent shear flows may be useful. First, results obtained in the strongly sheared part of the boundary layer by Saddoughi and Veeravalli (1994) indicated that the width of the Kolmogorov scaling range of the second order transverse structure function is significantly shorter than that of the longitudinal function (see figure 1.2). In an overview of turbulence spectra obtained in various flows, Sreenivasan (1995) noted that shear-flow turbulence exhibits inertial range scaling in the transverse spectrum only at values of R_λ larger than 10^3 . A later study by Noullez et al. (1997) lowered this threshold to 500. Second, there is evidence from experiments (e.g. Stolovitzky and Sreenivasan, 1993; Shen and Warhaft, 2002) and numerical simulations (e.g. Benzi et al., 1996) that the presence of a strong shear at low Reynolds numbers may destroy the extended self-similarity method (ESS) introduced by Benzi et al. (1993) (see section 1.4). We surmise from these observations that a delayed emergence of a scaling region can be avoided by eliminating shear from the turbulence. The process of elimination entails creating a uniform mean profile, $\langle U \rangle$, and mini-

mizing the Reynolds shear stresses, $\langle uv \rangle$. The total shear stress being¹

$$\tau(y) = \rho \nu \frac{\partial \langle U \rangle}{\partial y} - \rho \langle uv \rangle, \quad (4.5)$$

by having a uniform mean profile, the gradient term, $\partial \langle U \rangle / \partial y$, can be kept small; and if the Reynolds shear stress, $\langle uv \rangle$, is small too, the total shear stress is then negligible.

It was hoped that randomizing the forcing would suppress the growth of the Reynolds shear stress term, $\langle uv \rangle$. We gauged the Reynolds stresses by measuring the normalized correlations between orthogonal velocity components,

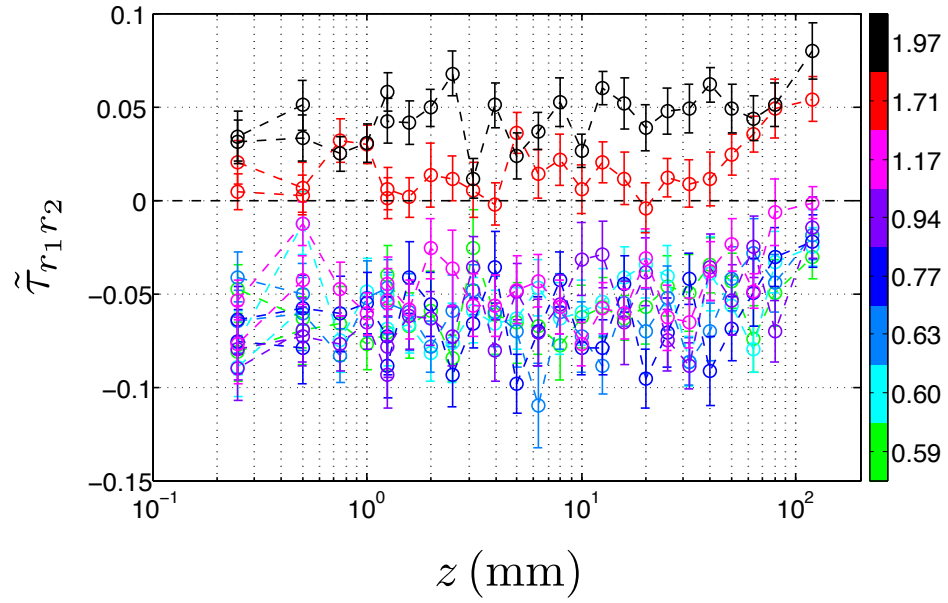
$$\tilde{\tau}_{r_1 r_2} = \frac{\langle u'_{r_1}(0, 0, z) u'_{r_2}(0, 0, z) \rangle}{\sqrt{\langle u'^2_{r_1}(0, 0, z) \rangle \langle u'^2_{r_2}(0, 0, z) \rangle}}, \quad (4.6)$$

and

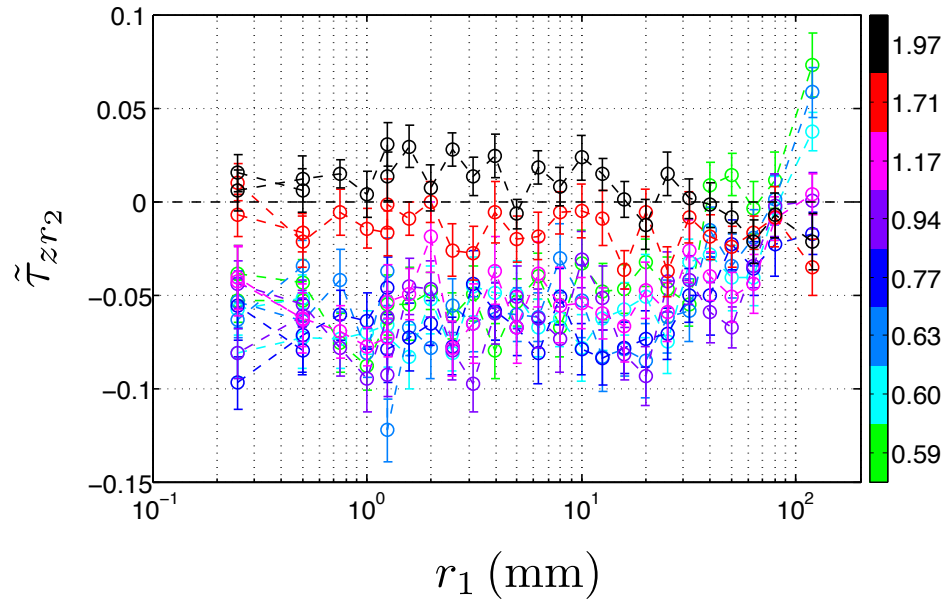
$$\tilde{\tau}_{z r_2} = \frac{\langle u'_z(r_1, 0, 0) u'_{r_2}(r_1, 0, 0) \rangle}{\sqrt{\langle u'^2_z(r_1, 0, 0) \rangle \langle u'^2_{r_2}(r_1, 0, 0) \rangle}}, \quad (4.7)$$

at various locations, z and r_1 , along the axial and radial axes. Figure 4.5(a) and (b) show tests at different levels of anisotropy. The shear stresses were always closer to zero than ± 0.1 over the entire range of distances from the center of the soccer ball; Shen and Warhaft (2000) and Shen and Warhaft (2002) have measured the shear stress in sheared turbulence and found that the value is about -0.4 and is constant throughout the flow. We concluded that the turbulence is essentially shearless because the mean shear stresses were less than 7% of the corresponding kinetic energies, $u'_{r_1} u'_{r_2}$ and $u'_z u'_{r_2}$, respectively. The present forcing randomization scheme is a simple method that gave remarkably satisfactory shearless turbulence. We believe the shear can be reduced further, for example, by covering the nozzle with specially designed passive grid with so-

¹It is customary to use U , V , and W to denote the mean velocities in the x , y , and z directions, respectively; and u , v , and w their corresponding RMS of the velocity fluctuations in the x , y , and z directions.



(a)



(b)

Figure 4.6: The figure shows the normalized Reynolds stress of orthogonal velocity components at various locations (a) along the axis of symmetry of the forcing, and (b) perpendicular to it. The values in the color bar are the anisotropy measured at the center of the soccer ball for various values of the anisotropy of the forcing.

lidity² $\sigma = 0.34$. For extreme values of solidity, $\sigma > 0.4$, the resulting turbulence behind the grid is unstable and non-uniform³ (Corrsin, 1963a). Useful design guidelines regarding pressure losses across the grid, the uniformity of the turbulence behind the grid, and its stability are collected in Roach (1987).

4.7 Conclusions

Our apparatus is unique among other loudspeaker-driven flow chambers because it permits a systematic exploration of anisotropic turbulence. We have shown that we are able to control the large-scale anisotropy of the turbulence, as summarized by the ratio between axial and radial components of the root-mean-square velocity, to any value between 0.6 and 2.3, with 1 being the value for isotropic turbulence. Table 4.2 summarizes the values of various parameters for the flows. Because the anisotropy, the mean flow, and the strength of the fluctuations are approximately constant within 50 mm of the center of the soccer ball, we call this the region of homogeneity.

²The solidity of a grid, σ , is defined as the projected solid area per unit total area. For a biplane grid with square mesh and round rods, the solidity is $\sigma = \frac{d}{M} (2 - \frac{d}{M})$, where d is the rod diameter and M is the distance between rod centerlines, or mesh size. The popular grid solidity $\sigma = 0.34$ is a compromise between low turbulence intensity, $u'/\langle U \rangle$, and high flow stability.

³The critical solidity $\sigma = 0.4$ limits the turbulence intensity behind the grid, since the turbulence intensity is proportional to the drag coefficient, and that, in turn, is proportional to the solidity.

A	0.33	0.4	0.5	0.8	1.0	1.25	2.0	2.5
u'_z (m s ⁻¹)	0.74	0.75	0.79	0.91	1.08	1.21	1.42	1.47
u'_{r_2} (m s ⁻¹)	1.26	1.24	1.27	1.19	1.15	1.03	0.83	0.75
u'_z/u'_{r_2}	0.59	0.60	0.63	0.77	0.94	1.17	1.71	1.97
K (m ² s ⁻²)	1.87	1.83	1.92	1.82	1.91	1.79	1.69	1.65
$ U_z/U_{r_2} $	0.31	0.16	0.13	0.15	4.04	2.57	7.58	23.9
$ U $ (m s ⁻¹)	0.17	0.18	0.13	0.10	0.05	0.07	0.14	0.24
$\tilde{\tau}_{r_1 r_2}$	-0.07	-0.06	-0.06	-0.07	-0.07	-0.05	0.01	0.04
$\tilde{\tau}_{z r_2}$	-0.06	-0.07	-0.06	-0.07	-0.07	-0.06	-0.01	0.02
ϵ (m ² s ⁻³)	5.41	4.94	5.43	6.00	6.71	6.98	6.49	6.45
η (μm)	163	167	163	159	155	153	156	156
τ_η (ms)	1.7	1.8	1.7	1.6	1.5	1.5	1.6	1.6
λ (mm)	7.4	7.6	7.5	6.9	6.7	6.3	6.4	6.3
R_λ	525	536	538	485	480	443	434	423

Table 4.2: The table shows the turbulence parameters, for loudspeaker RMS amplitude ratios (A) ranging from 0.33 to 2.5. K is the turbulent kinetic energy, $\frac{1}{2}(u_z'^2 + 2u_{r_2}'^2)$, and $|U|$ is $(U_z^2 + 2U_{r_2}^2)^{1/2}$. $\tilde{\tau}_{r_1 r_2}$ and $\tilde{\tau}_{z r_2}$ are the average normalized Reynolds stresses measured along and normal to the axis of symmetry, respectively (see section 4.6). ϵ is the energy dissipation rate estimated according to the procedure prescribed in section 5.1. η and τ_η are the Kolmogorov length and time scales, respectively. λ is the Taylor length (see section 5.3) and R_λ is the Taylor scale Reynolds number. Data were collected at the center of the soccer ball when the axis of symmetry of the forcing is horizontal. Similar results (not shown) were obtained when the axis of symmetry is vertical.

CHAPTER 5

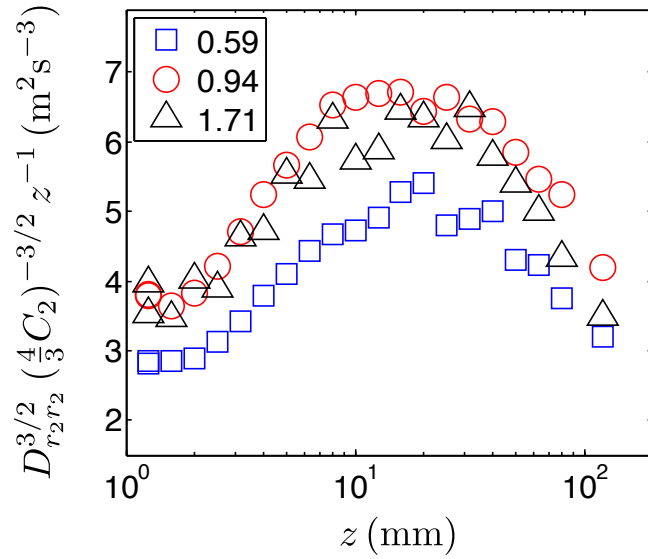
UNIVERSALITY IN THE STRUCTURE FUNCTIONS

In this chapter, we examine how the inertial scales of the turbulence generated by the apparatus introduced in chapter 2 are influenced by the anisotropy of the forcing, through the measurements of the second order moment of velocity increments. We measured the transverse structure functions, $D_{r_2 r_2}(z) = \langle (u'_{r_2}(0, 0, z) - u'_{r_2}(0, 0, 0))^2 \rangle$ and $D_{zz}(r_1) = \langle (u'_z(r_1, 0, 0) - u'_z(0, 0, 0))^2 \rangle$, with the separation vector lying nearly along the axis of symmetry or perpendicular to it, and show that, in an inertial range that spanned nearly a decade, the Kolmogorov constant and the inertial range scaling exponents were scalar valued in unsheared anisotropic turbulence, within the experimental error of 10%.

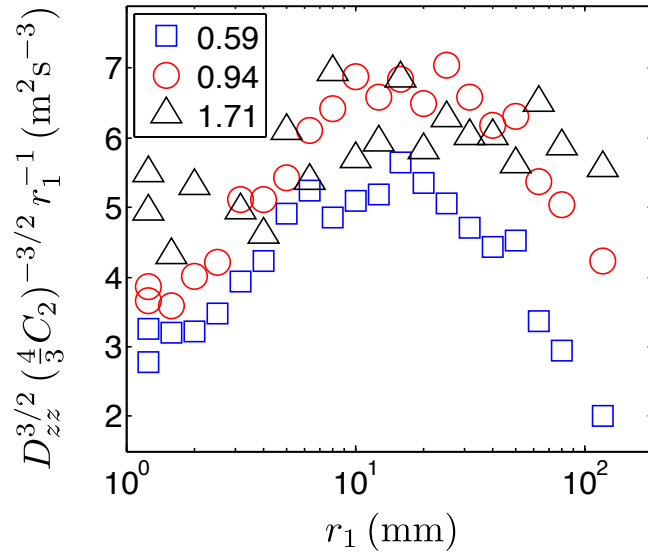
5.1 Isotropy of the structure functions

To determine the inertial range of the turbulence for different anisotropies, we plot in figures 5.1(a) and (b) the measure for energy per unit time and mass, $(D_{r_2 r_2}(z))^{3/2} (4 C_2/3)^{-3/2} z^{-1}$ and $(D_{zz}(r_1))^{3/2} (4 C_2/3)^{-3/2} r_1^{-1}$, as functions of z and r_1 , respectively. No noise corrections were applied to the structure functions. The value of C_2 was taken to be 2.1 (Sreenivasan, 1995). We found that the inertial range spanned approximately one decade, as indicated by the extent of flat region in figures 5.1(a) and (b).

Figure 5.2 shows the scale-dependent measure of isotropy, namely $D_{zz}(r_1)/D_{r_2 r_2}(z)$, where $r_1 = z$. In the limit of large separations, the ratio should approach $u'_z{}^2/u'_{r_2}{}^2$, since the velocities $u'_i(\mathbf{r})$ and $u'_i(0)$ are uncorrelated when \mathbf{r} is large enough. Although we could not resolve this asymptotic limit due to ex-



(a)



(b)

Figure 5.1: The figure shows the (a) axial structure functions, $D_{r_2 r_2}(z)$, and (b) radial structure functions, $D_{zz}(r_1)$. In both cases, the structure functions are divided by the inertial range scaling predicted by Kolmogorov. The error bars are smaller than the symbols. The values in the legends are the anisotropy measured at the center of the soccer ball for various values of the anisotropy of the forcing.

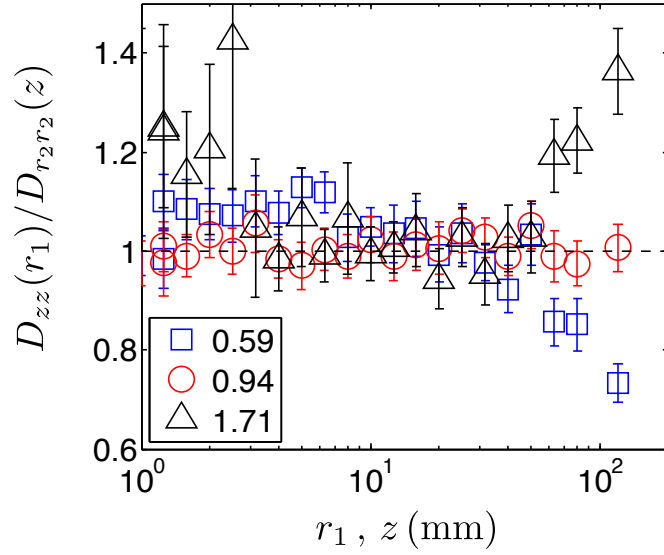


Figure 5.2: The ratios between structure functions in different directions but in the same flow, $D_{zz}(r)/D_{r_2r_2}(z)$, approach the isotropic value of one when the separation distance, $r_1 = z$, decreases. Results for data taken at other values of the large-scale anisotropy are consistent with those shown here. The values in the legends are the anisotropy measured at the center of the soccer ball.

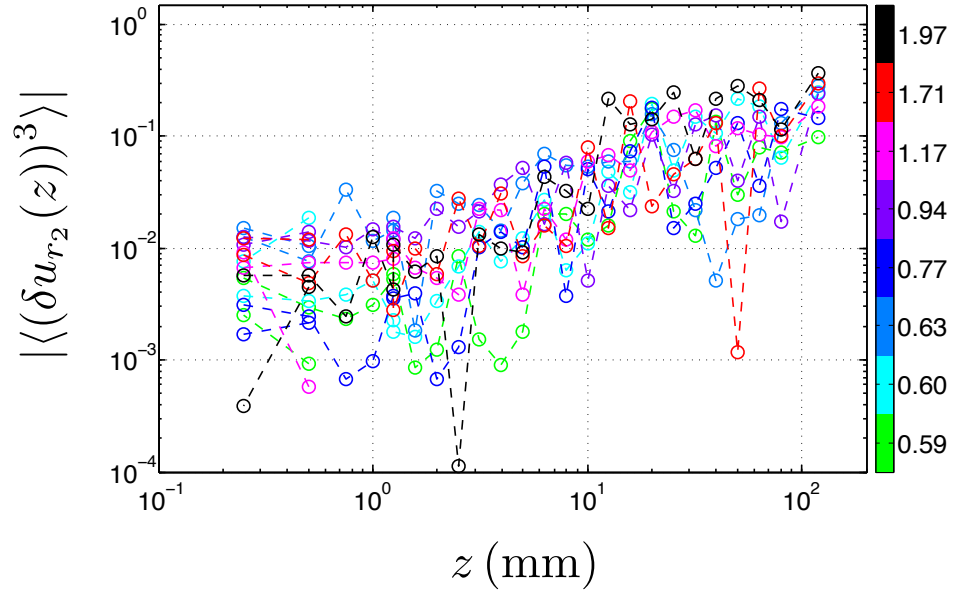
perimental limitations, the values of this ratio in anisotropic cases did clearly separate from the isotropic value. Moving toward small scales, local isotropy requires that $D_{zz}(r)/D_{r_2r_2}(z)$ approaches one. The figure reveals that within the experimental error we observed local isotropy for separations smaller than the energy injection scale.

5.2 Equality of transverse ESS scaling exponents

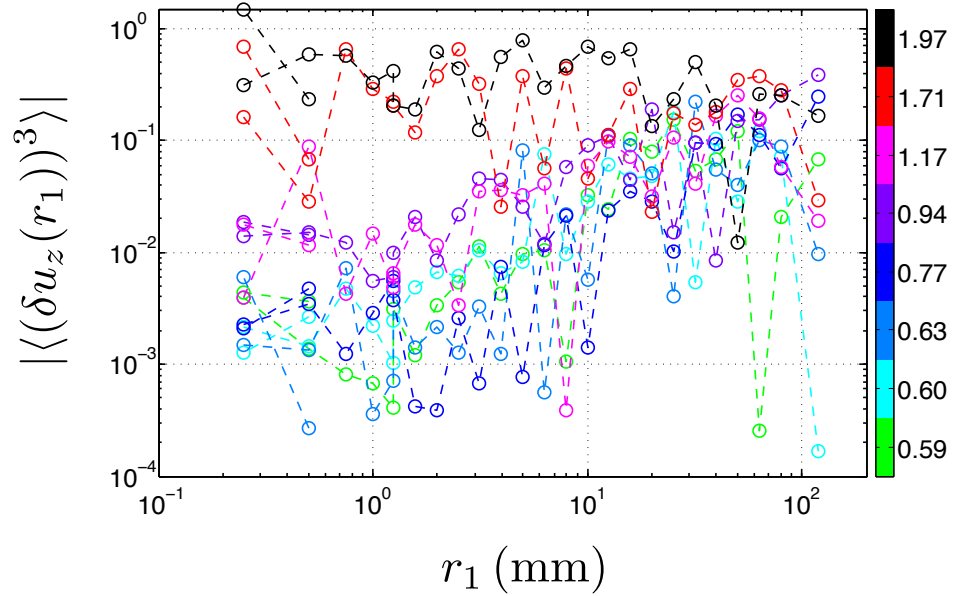
Here, we investigate how the scaling exponent measured using the ESS method, as described in section 1.4, depends on the anisotropy of the forcing. We begin with an examination of the third order transverse structure function, $\langle(\delta u(x))^3\rangle$, and its ESS variant, $\langle|\delta u(x)|^3\rangle$. Figures 5.3(a) and (b) show $\langle(\delta u_{r_2}(z))^3\rangle$ and

$\langle(\delta u_z(r_1))^3\rangle$ as functions of z and r_1 , respectively. No noise corrections were applied to these structure functions. It can be seen that $\langle(\delta u_{r_2}(z))^3\rangle$ and $\langle(\delta u_z(r_1))^3\rangle$ were nearly zero and varied unsystematically with separations, as all odd-order moments should if the turbulence is locally isotropic (Shen and Warhaft, 2002). This contrasts the predictions in shear flows, where simple Kolmogorov-type argument assuming that $\langle(\delta u(x))^3\rangle$ is proportional to the shear yields $\langle(\delta u(x))^3\rangle \sim x^{4/3}$ (Lumley, 1967). The absence of a four-thirds scaling reflects the absence of shear in our flow. Figures 5.4(a) and (b) show the scaling of $\langle|\delta u_{r_2}(z)|^3\rangle$ and $\langle|\delta u_z(r_1)|^3\rangle$ with separations, z and r_1 . It can be seen that the scaling range spans approximately a decade from 2 mm to 20 mm. For reference, it might be noted that the empirical scaling for $\langle|\delta u(x)|^3\rangle$ is $\langle|\delta u(x)|^3\rangle \sim x^{1.17}$ for the present measurement, for which the value 1.17 has been obtained by averaging the exponents obtained from straight-line fits, $\log\langle|\delta u(x)|^3\rangle \sim \log x$, to the individual curves.

We now consider the ESS plots for $D_{r_2 r_2}(z) \sim \langle|\delta u_{r_2}(z)|^3\rangle^{\zeta_2^{(z)}}$ and $D_{zz}(r_1) \sim \langle|\delta u_z(r_1)|^3\rangle^{\zeta_2^{(r_1)}}$ in figure 5.5. We obtain two sets of exponents, $\zeta_2^{(z)}$ for the axial function, $D_{r_2 r_2}(z)$, and $\zeta_2^{(r)}$ for the radial function, $D_{zz}(r_1)$, by calculating the slopes obtained from straight-line fits, $\log(D(r)) \sim \log\langle|\delta u(r)|^3\rangle$, to the data. The exponents, $\zeta_2^{(z)}$ and $\zeta_2^{(r)}$, are shown in figure 5.6. The uncertainty in the exponents was estimated with the standard error of the slopes in the straight-line fits (see equation B.12 in appendix B). Table 5.1 lists the numerical values for $\zeta_2^{(z)}$ and $\zeta_2^{(r)}$. The scatter in the data sets for $D_{zz}(r_1)$ with anisotropy ratios $u'_z/u'_r = 1.71$ and 1.97 could be due to a number of reasons. It may have been an artifact of the limitation in instrument spatial resolution, a residual shear in the turbulence, or an insufficiently developed turbulent region. For these reasons, we have plotted their exponents with gray symbols in figure 5.6. The average

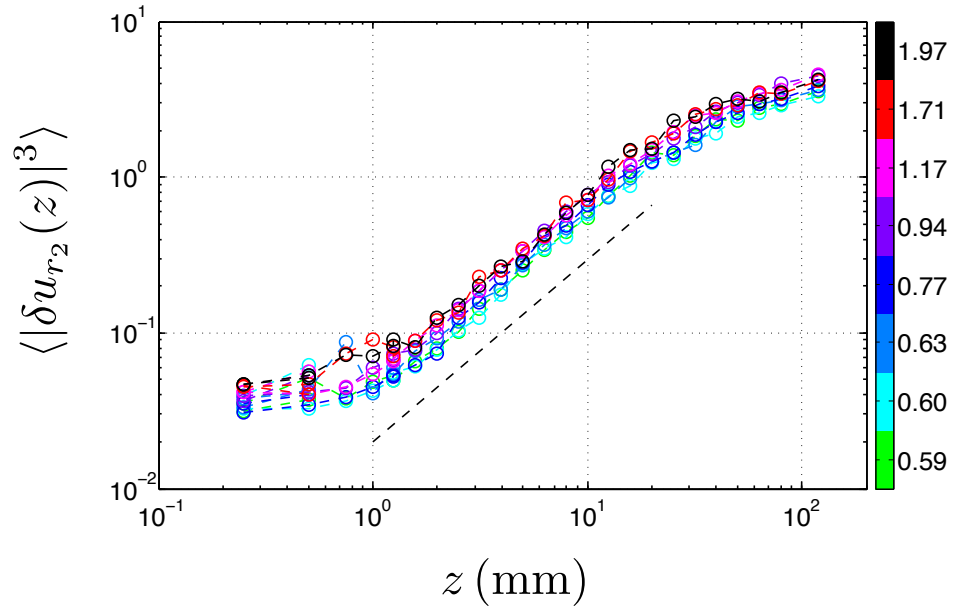


(a)

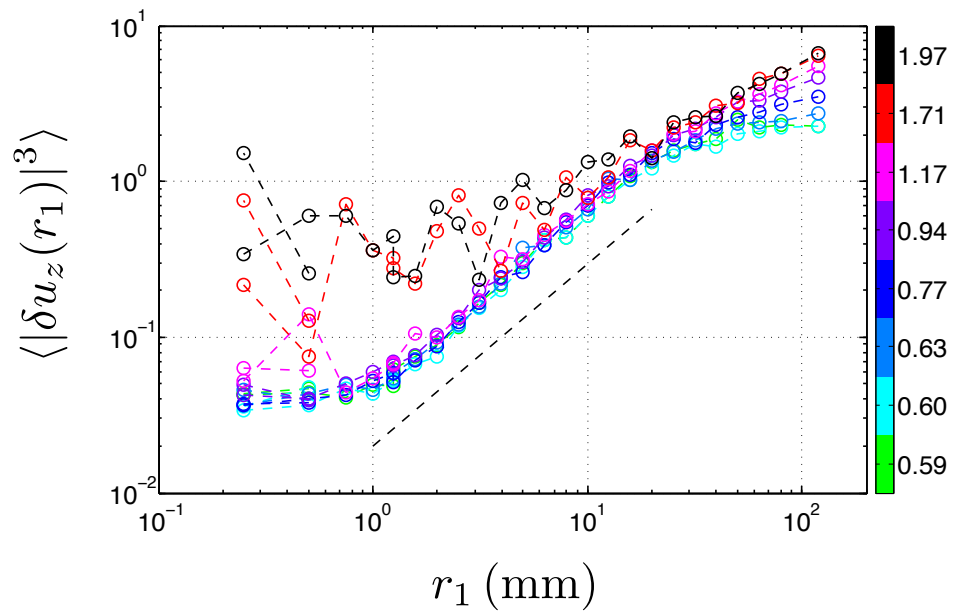


(b)

Figure 5.3: The third-order structure functions with separations in the direction (a) along the axis of symmetry, and (b) perpendicular to the axis of symmetry. The values in the color bar are the anisotropy measured at the center of the soccer ball.



(a)



(b)

Figure 5.4: The third-order moments of the absolute values of the velocity increments with separations in the direction (a) along the axis of symmetry, and (b) perpendicular to the axis of symmetry. The dashed lines are proportional to a power law with exponent 1.17. The values in the color bar are the anisotropy measured at the center of the soccer ball.

u'_z/u'_r	$\zeta_2^{(r)}$	$\zeta_2^{(z)}$	$\zeta_2^{(r)}/\zeta_2^{(z)}$
0.59 ± 0.03	0.739 ± 0.007	0.721 ± 0.005	1.024 ± 0.017
0.60 ± 0.02	0.733 ± 0.007	0.732 ± 0.008	1.001 ± 0.020
0.63 ± 0.03	0.733 ± 0.006	0.726 ± 0.011	1.009 ± 0.024
0.77 ± 0.03	0.730 ± 0.004	0.727 ± 0.004	1.004 ± 0.011
0.94 ± 0.04	0.719 ± 0.004	0.724 ± 0.004	0.993 ± 0.012
1.16 ± 0.05	0.752 ± 0.018	0.733 ± 0.005	1.026 ± 0.031
1.71 ± 0.10	0.847 ± 0.072	0.730 ± 0.007	1.161 ± 0.111
1.98 ± 0.10	0.875 ± 0.101	0.738 ± 0.007	1.186 ± 0.147

Table 5.1: The numerical data for radial scaling exponents ($\zeta_2^{(r)}$), axial scaling exponents ($\zeta_2^{(z)}$), and the ratio between the two.

ζ_2	R_λ	Source
0.70 ± 0.005	37 – 82	Camussi et al. (1996)
0.70 ± 0.01	365 – 605	Noullez et al. (1997)
0.71	1000	Zhou et al. (2001)
$0.71 - 0.74$	$40 - 10^4$	Pearson and Antonia (2001)
0.73 ± 0.02	480	Present work

Table 5.2: The value of the scaling exponent of transverse second order structure functions, ζ_2 , measured using the ESS method for various laboratory flows.

value for the scaling exponents, excluding the last two radial data sets, was 0.73 ± 0.02 , for which the error was the the standard deviation of the values of the exponents. The value for the mean exponent is largely consistent with values measured using similar transverse ESS method reported in the literature at comparable Reynolds numbers, see table 5.2.

We now consider the ratio formed by the two exponents, $\zeta_2^{(r)}/\zeta_2^{(z)}$, and observe how it varies with anisotropy, u'_z/u'_r . As shown in figure 5.7, except for the last two values of anisotropy, the ratio is nearly 1. Again, noise or residual shear

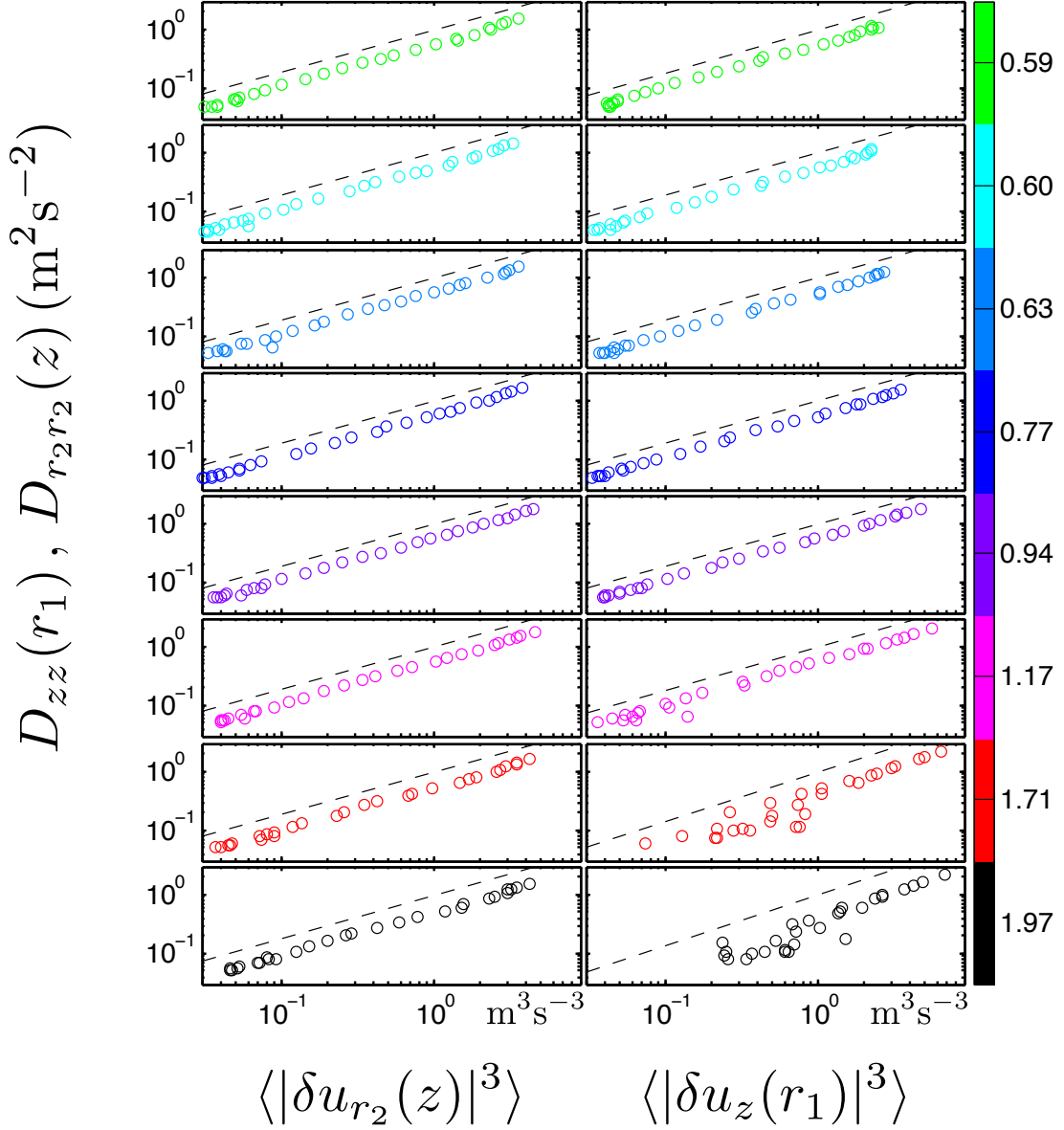


Figure 5.5: The extended-self-similarity plots for the second-order transverse structure functions. The dashed lines are proportional to the power laws obtained from least squares fits to data. The values in the color bar are the anisotropy measured at the center of the soccer ball for various values of the anisotropy of the forcing. The error bars are smaller than the symbols.

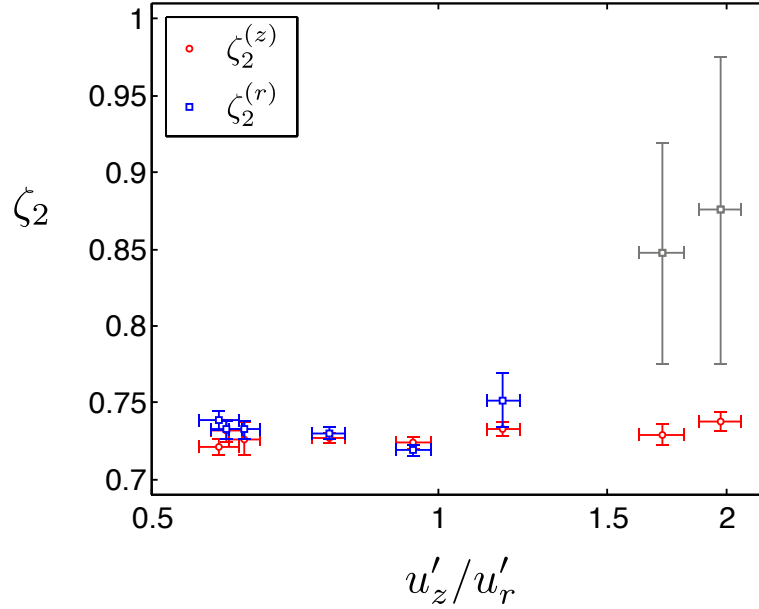


Figure 5.6: The scaling exponents for the transverse structure functions measured using the extended-self-similarity method. The \circ symbols are the scaling exponents for $D_{r_2 r_2}(z)$ and the \square symbols are for $D_{zz}(r_1)$. The last two points in the radial data set have large uncertainties due to spatial resolution. They are marked in gray to show the general trend of the exponents.

might have affected the last two radial structure functions, even though the exponents $\zeta_2^{(z)}$ for the corresponding axial structure functions were well within the mean of the estimated values. Thus, based on our measurements for anisotropy ratios $0.59 \leq u'_z/u'_r \leq 1.16$, we conclude that $\zeta_2^{(z)}$ and $\zeta_2^{(r)}$ are equal.

5.3 Scalar-valuedness of the Kolmogorov constant

Let us now examine the Kolmogorov constant, C_2 (see equation 1.19 and 1.20). Anisotropy of the large scales allows for a family of equations in the form of equation 1.20, but with different constants, $C_2^{(x)}$, for each direction of r . A

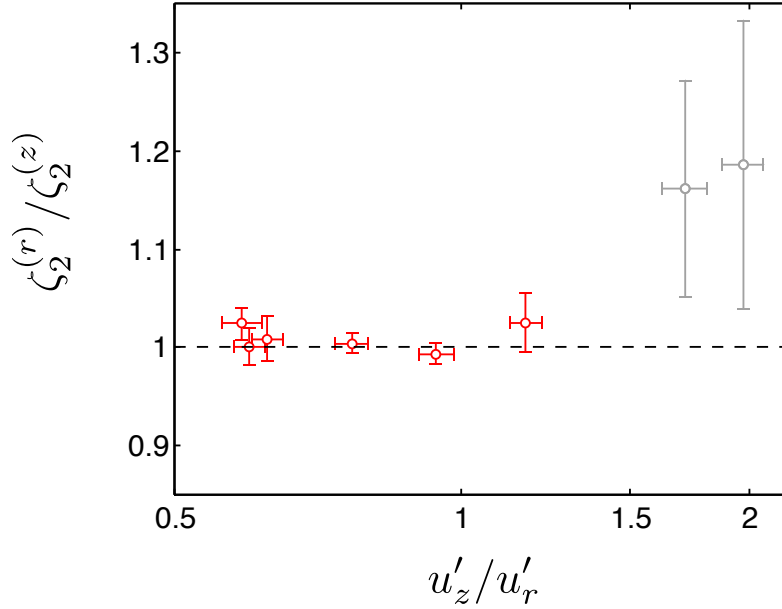


Figure 5.7: The figure shows $\zeta_2^{(r)}/\zeta_2^{(z)}$, the ratio between the scaling exponents of the radial structure functions and those of the axial structure functions. The last two points with large uncertainties due to spatial resolution are marked in gray.

measure of inertial range anisotropy is $C_2^{(r)}/C_2^{(z)}$, which we calculated in two ways. First, in figure 5.8, we plot $D_{zz}(r_1)/D_{r_2r_2}(z)$ against the separations r_1 and z . These are the same data sets shown in figure 5.2. For clarity, they are displayed individually. We computed an average of the structure function ratio, $\langle D_{zz}(r_1)/D_{r_2r_2}(z) \rangle$, taken over the range of separations where the compensated structure functions displayed a reasonable plateau, or $7 \text{ mm} < r_1, z < 70 \text{ mm}$. Since the energy dissipation, ϵ , is a scalar quantity, the ratio of structure functions in the inertial range of scales is equal to the ratio $C_2^{(r)}/C_2^{(z)}$. To estimate the uncertainty in the measurements, we have used the standard error in the measurements of the ratios (see appendix B, equation B.3). The second method was designed to mimic the one usually employed to measure C_2 (or ϵ) when the data are collected in only one direction. That is, we estimated C_2 from the

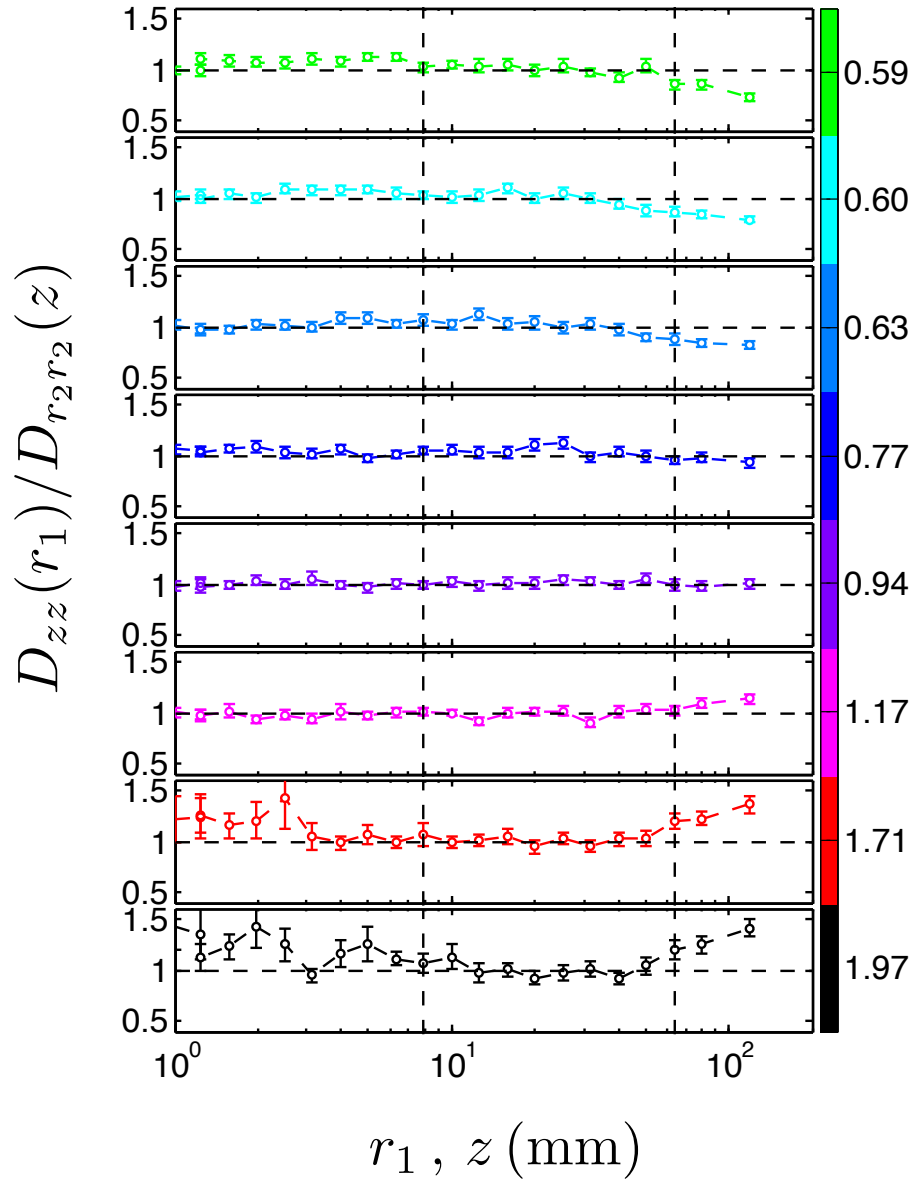


Figure 5.8: The figure shows the ratio between structure functions in different directions in the same flow, $D_{zz}(r_1)/D_{r_2r_2}(z)$, for all values of the anisotropy of the forcing. The data are the same as in figure 5.2. They are plotted separately to display individual trends. The two vertical dashed lines demarcate the range of scales between 7 and 70 mm where the compensated structure functions displayed a reasonable plateau. The values in the color bar are the fluctuations anisotropy measured at the center of the soccer ball for various values of the anisotropy of the forcing.

maxima of the compensated structure functions, $D(x) x^{-2/3}$. In order to reduce the influence of noise, we fit a second-order polynomial function

$$y = a + b \log(x) + c (\log(x))^2, \quad (5.1)$$

to each data set in the range of scales between 2 and 50 mm, see figure 5.9. Although this form is decidedly inappropriate since the structure function should approach a constant for large separations, it proves to be very instructive in analyzing the data. We estimated the maximum value of $C_2^{(x)} \epsilon^{2/3}$ for each curve by calculating the ordinate of the peak of the parabola, given analytically in terms of the fitting parameters a , b , and c

$$y_{\max} = a - \frac{b^2}{4c}. \quad (5.2)$$

The ratio between the maxima, $\max(D_{zz}(r_1) r_1^{-2/3}) / \max(D_{r_2 r_2}(z) z^{-2/3})$, was then calculated. The ratio so formed, the energy dissipation rate being a scalar quantity falls out of the ratio, gave a second measure of $C_2^{(r)} / C_2^{(z)}$. To evaluate the fit, we calculated the difference between experimental and predicted values, $\xi_i = y_i - \tilde{y}_i$, where y_i is the original value from experiment and \tilde{y}_i is the value predicted by the parabolic fit. The standard deviation, or variability, of ξ_i

$$\text{Variability} = \left[\frac{1}{N-1} \sum_{i=1}^N (\xi_i - \langle \xi \rangle)^2 \right]^{1/2}, \quad (5.3)$$

where N is the number of data points used in the fit, gave an estimate for the error in the measurements

The two measures of $C_2^{(r)} / C_2^{(z)}$ are shown in figure 5.10, and their numerical values are listed side by side in table 5.3. It can be seen that within measurement error, $C_2^{(r)}$ equals $C_2^{(z)}$; the small downward trend is comparable to the scatter. Thus, we conclude that the Kolmogorov constant is scalar valued over the range of anisotropies studied here.

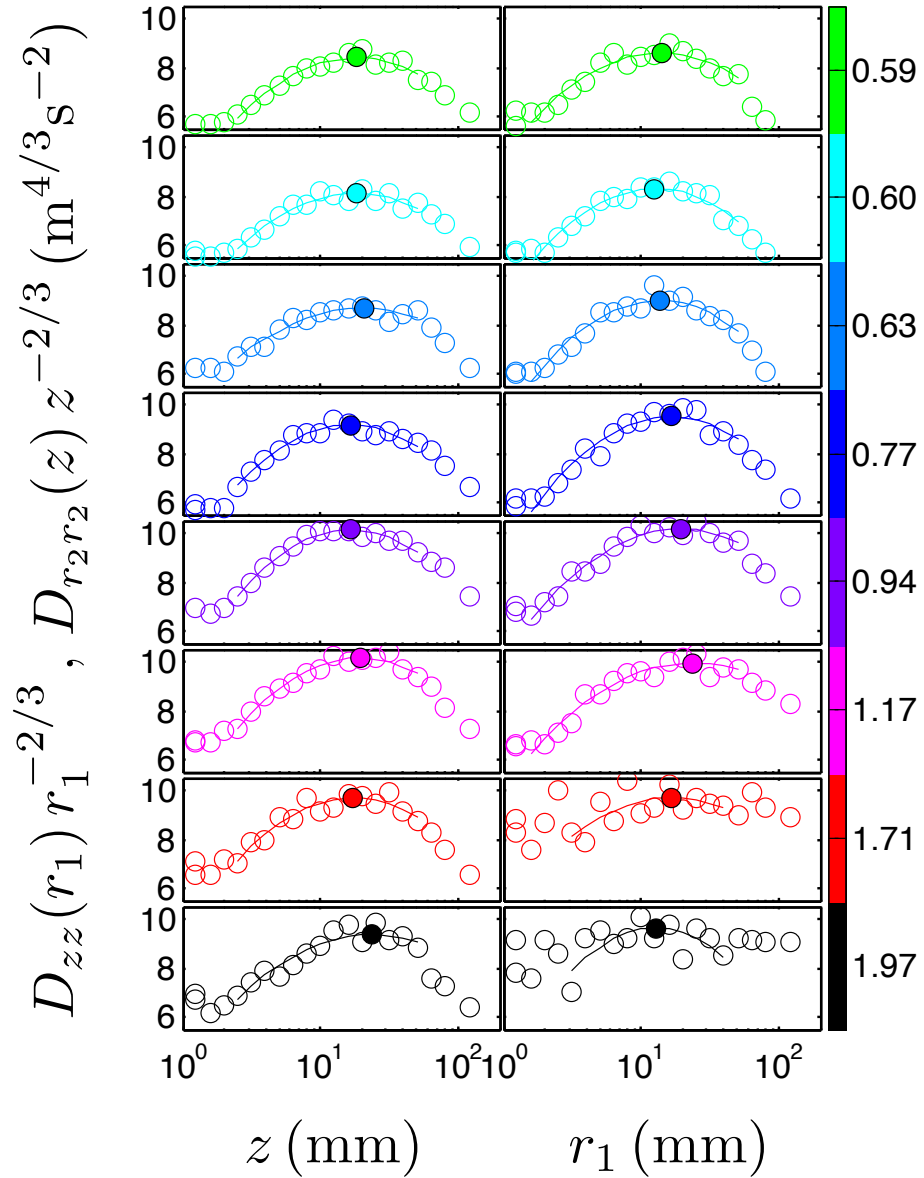


Figure 5.9: The compensated axial and radial transverse structure functions for all values of anisotropy. Only the data in the range of scales between 2 and 50 mm are used in the determination of the ratio of the Kolmogorov constant. Solid lines are the second-order, least-square, linear-log polynomial fits to the structure function data. Solid symbols are the maxima of the fitted curves. The error bars are smaller than the symbols. The values in the color bar are the anisotropy measured at the center of the soccer ball for various values of the anisotropy of the forcing.

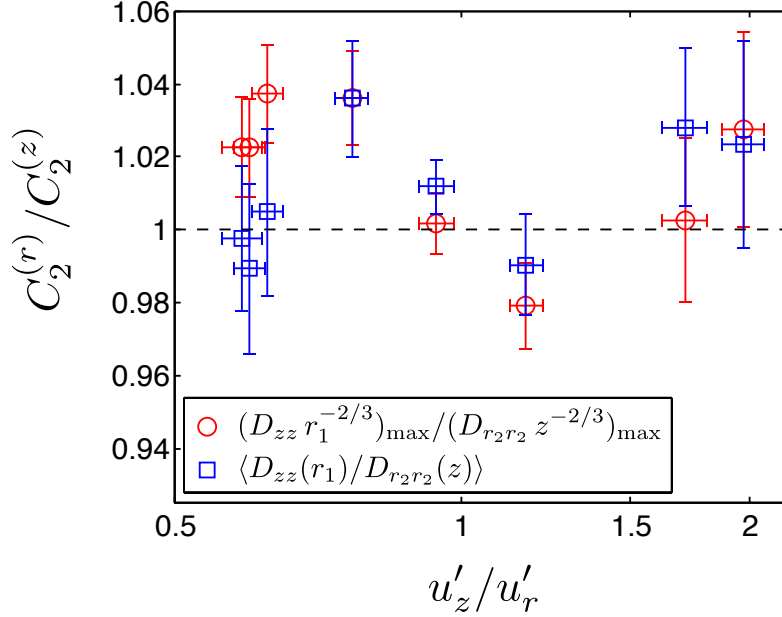


Figure 5.10: The ratio between Kolmogorov constants measured in different directions $C_2^{(r)}/C_2^{(z)}$. The open circular symbols (\circ) are the ratio between the maximum values of the compensated radial and axial structure functions. The open square symbols (\square) are $\langle D_{zz}(r_1)/D_{r_2r_2}(z) \rangle$, the ratio of radial to axial structure functions averaged over a range of scales $7 < r < 70$ mm.

Let us conclude with the calculation of the flow parameters. We determined ϵ by taking the peak values of the compensated structure functions, as plotted in figure 5.1, assuming that the second order structure functions obey Kolmogorov-type scaling law. This assumption may not be valid in view of the anomaly of the scaling exponent discussed in section 5.2, but dimensional considerations compelled us to adhere to this definition. The dissipation rates depended on the anisotropy and reached a maximum value of $6.71 \text{ m}^2\text{s}^{-3}$ for the case of isotropic turbulence. The variation of the dissipation rate with varying anisotropy of the agitation is most likely the result of our decision to fix the total kinetic energy of the turbulence, see equation 3.1. Fixing the turbulence kinetic energy does not guarantee a constant energy dissipation rate, since the

$C_2^{(r)}/C_2^{(z)}$				
$\frac{u'_z}{u'_r}$	$\left\langle \frac{D_{zz}(r_1)}{D_{r_2r_2}(z)} \right\rangle$	Variability	$\frac{\max(D_{zz}/r_1^{2/3})}{\max(D_{r_2r_2}/z^{2/3})}$	Variability
0.59 ± 0.03	0.998	± 0.020	1.023	± 0.014
0.60 ± 0.02	0.989	± 0.024	1.022	± 0.014
0.63 ± 0.03	1.004	± 0.023	1.037	± 0.014
0.77 ± 0.03	1.036	± 0.016	1.036	± 0.013
0.94 ± 0.04	1.012	± 0.007	1.002	± 0.009
1.16 ± 0.05	0.990	± 0.014	0.979	± 0.012
1.71 ± 0.10	1.028	± 0.022	1.003	± 0.023
1.98 ± 0.10	1.024	± 0.029	1.028	± 0.027

Table 5.3: The numerical data for the ratio of the Kolmogorov constant for transverse structure functions measured in nearly orthogonal directions, computed from averaging the ratio $D_{zz}(r_1)/D_{r_2r_2}(z)$ over a range of scales between 7 and 70 mm (second column), as well as from taking the ratio between the maxima of appropriately compensated structure functions, $\max(D_{zz}/r_1^{2/3})/\max(D_{r_2r_2}/z^{2/3})$ (fourth column). The values in the third and the last columns are the corresponding estimated error.

energy dissipation rate depends also on the large scales of the flow, which in turn depend on the anisotropy.

Under isotropic forcing, the Taylor scale was $\lambda = \sqrt{15\nu u'^2/\epsilon} = 6.7$ mm, where $\nu = 1.568 \times 10^{-5}$ m²s⁻¹ is the kinematic viscosity of air at room temperature, and the Taylor-microscale Reynolds number was $R_\lambda = \lambda u'/\nu = 480$. The Reynolds numbers for the anisotropic cases were slightly lower. The corresponding Kolmogorov length and time scales were $\eta = (\nu^3/\epsilon)^{1/4} = 155$ μ m and $\tau_\eta = \sqrt{\nu/\epsilon} = 1.5$ ms.

5.4 Conclusions

We investigated systematically the influence of the anisotropic agitation on the inertial scales of turbulence in flows for which the ratio of axial to radial RMS velocity fluctuations was between 0.6 and 2.3, with Taylor based Reynolds number $R_\lambda = 480$. For scales smaller than the energy injection scale, the second-order transverse velocity structure functions were independent of anisotropy. Within the experimental uncertainty, the inertial range scaling exponent and the Kolmogorov constant were independent of anisotropy. We expect anisotropic corrections, such as those introduced by the SO(3) decomposition (Biferale and Procaccia, 2005), to be smaller than the error in our measurements (about 5%). This will be true unless the corrections would cancel in the two directions we measured; an outcome we consider unlikely. Our findings contrast with previous results by Shen and Warhaft (2002), who found that the scaling exponent for the transverse structure function in the direction of a mean shear was different from the scaling exponent in the direction of the mean wind by about 0.1; this indicates that the anisotropy produced by shear may be inherently different from that produced by turbulent fluctuations. Our result is of practical importance in providing a means of unambiguously estimating the parameters of anisotropic flows without shear, such as the energy dissipation rate and the Reynolds number.

CHAPTER 6

HIGHER ORDER STATISTICS

In this chapter, we extend our investigation of the influence of anisotropy on the higher order statistics. We provide measurements of the structure functions, $\langle |\delta u(x)|^n \rangle$, for $n = 4, 5, 6$, as described in section 1.4, and the nondimensional ratios, $\langle |\delta u(x)|^4 \rangle / \langle |\delta u(x)|^2 \rangle^2$ and $\langle |\delta u(x)|^6 \rangle / \langle |\delta u(x)|^2 \rangle^3$.

It has now become common in studies of intermittency to look at higher order structure functions. Measurements of higher order structure functions are very difficult. This is because higher order moments are influenced by rare events in the tails of the probability distribution (PDF), thus requiring a longer data set. We can estimate how much time and storage space it requires to collect these rare events. Experiments (e.g. Anselmet et al., 1984) suggest that the probability distribution of the velocity increments, δu , can be approximated by an exponential, $P(x) \sim e^{-x}$, where $x = \delta u / \langle |\delta u|^2 \rangle^{1/2}$. For good convergence of the n th order moment, $\langle |\delta u|^n \rangle$, the rule of thumb is to resolve δu up to $n \langle |\delta u|^2 \rangle^{1/2}$, which corresponds to the location of the peak of $x^n P(x)$ (e.g. Staicu and Van de Water, 2003). Let us consider the sixth order moment. From figure 16 of Shen and Warhaft (2000), we estimate that $P(x = 6) \approx 10^{-4}$. If 10 counts are required around $x = 6$, then the total number of samples we need to collect is $10/10^{-4} = 10^5$. This is very close to the number of samples we actually collected for δu in the experiment. This amount of data occupied approximately 50 megabytes of disc space in 20 minutes. The total amount of time for 28 different separation distances and 16 anisotropies (8 for scanning along the symmetry axis of the forcing, and another 8 perpendicular to it) was then 6.2 days and the total disc space was about 22 gigabytes. Now for the 12th order mo-

ment, $P(x = 12) \approx 10^{-9}$ (Anselmet et al. (1984), figure 3). Taking 10 again as a reasonable number of counts, the total amount of time and disc space required would be about 1700 years and 2.1 petabytes. Thus, it can be seen that a precise measurement of the high-order moments of the velocity increments with LDV may take many generations of graduate students to accomplish.

6.1 Higher order structure functions

In figures 6.1, 6.2, and 6.3, we show the ESS plots of transverse structure functions up to the sixth order. As can be seen, the quality of data for higher order moments of velocity increments quickly deteriorates when increasing the order. This is especially so for extreme prolate shape anisotropies and for separations in the dissipative range. Let us examine the important issue of convergence. Figure 6.4 shows, from top to bottom, the normalized probability density of $\delta u_{r_2}(z)$, denoted as $P(x)$, where $x = \delta u_{r_2}(z)/\langle |\delta u_{r_2}(z)|^2 \rangle^{1/2}$ is the velocity increments normalized by their standard deviation, and $P(x)$ multiplied by x^2 , x^3 , x^4 , x^5 , and x^6 for a nearly spherically symmetric turbulent flow, $u'_z/u'_r = 0.94$, at $R_\lambda = 480$. Here, the probe volume spacing was 20 mm, which corresponded to about 130η . We obtained the PDF from approximately 78000 data points and resolved the PDF to approximately 8 standard deviations. There seemed to be no convergence problems for the second to fifth moments. The tails of these curves tended to flatten out at high x . The sixth moment was not as well converged as the lower orders; yet all moments showed strong asymmetry. This is clearly indicated in table 6.1 by the difference in the area integrated under the curves. The values of the third to the sixth moments were -0.107 , 6.88 , -0.689 , and 141 . The same features can be seen in the inertial range PDF obtained by Shen and

Order of moment (n)	0	2	3	4	5	6
$(-1)^n \int_{-\infty}^0 x^n P(x) dx$	0.512	0.519	1.14	3.57	14.6	71.8
$\int_0^{\infty} x^n P(x) dx$	0.488	0.468	1.03	3.31	13.9	69.6
$\int_{-\infty}^{\infty} x^n P(x) dx$	1.00	0.987	-0.107	6.88	-0.689	141

Table 6.1: The numerical integral of the PDF and its moments from the second to the sixth order of an isotropically forced turbulent flow, shown in figure 6.4. The isotropy ratio was $u'_z/u'_r = 0.94$ and the Reynolds number was $R_\lambda = 480$ (see table 4.2).

Warhaft (2000) in a wind tunnel homogeneous nonsheared turbulent flow at $R_\lambda = 934$ and a probe spacing of 153η . All their third to sixth moments showed strong asymmetry; their values were -0.46 , 5.14 , -7.81 , and 66.7 . Notice that the asymmetry in Shen and Warhaft (2000) is left-right inverted because their definition of the velocity increments is $\delta u(z) = u(0) - u(z)$ whereas we have defined it as $\delta u(z) = u(z) - u(0)$. The difference in signs between our odd order moments and those of Shen and Warhaft (2000) has been corrected in the above comparison.

Figure 6.5 shows the PDF of $\delta u_{r_2}(z)$ for an oblate shape forcing, $u'_z/u'_r = 0.60$, at the same probe separation and R_λ comparable to the spherically symmetric case. We obtained about 10^5 points. The improvement brought about by an increase in the sample size to the convergence of the higher order moments was marginal; yet the asymmetry in the PDF was evident, as indicated by an increase in the values of the odd order moments in table 6.2. The values for the third to the sixth moments were -0.19 , 7.07 , -2.11 and 154 . The asymmetry in the PDF of δu was highly reproducible from flow to flow with different values of anisotropy.

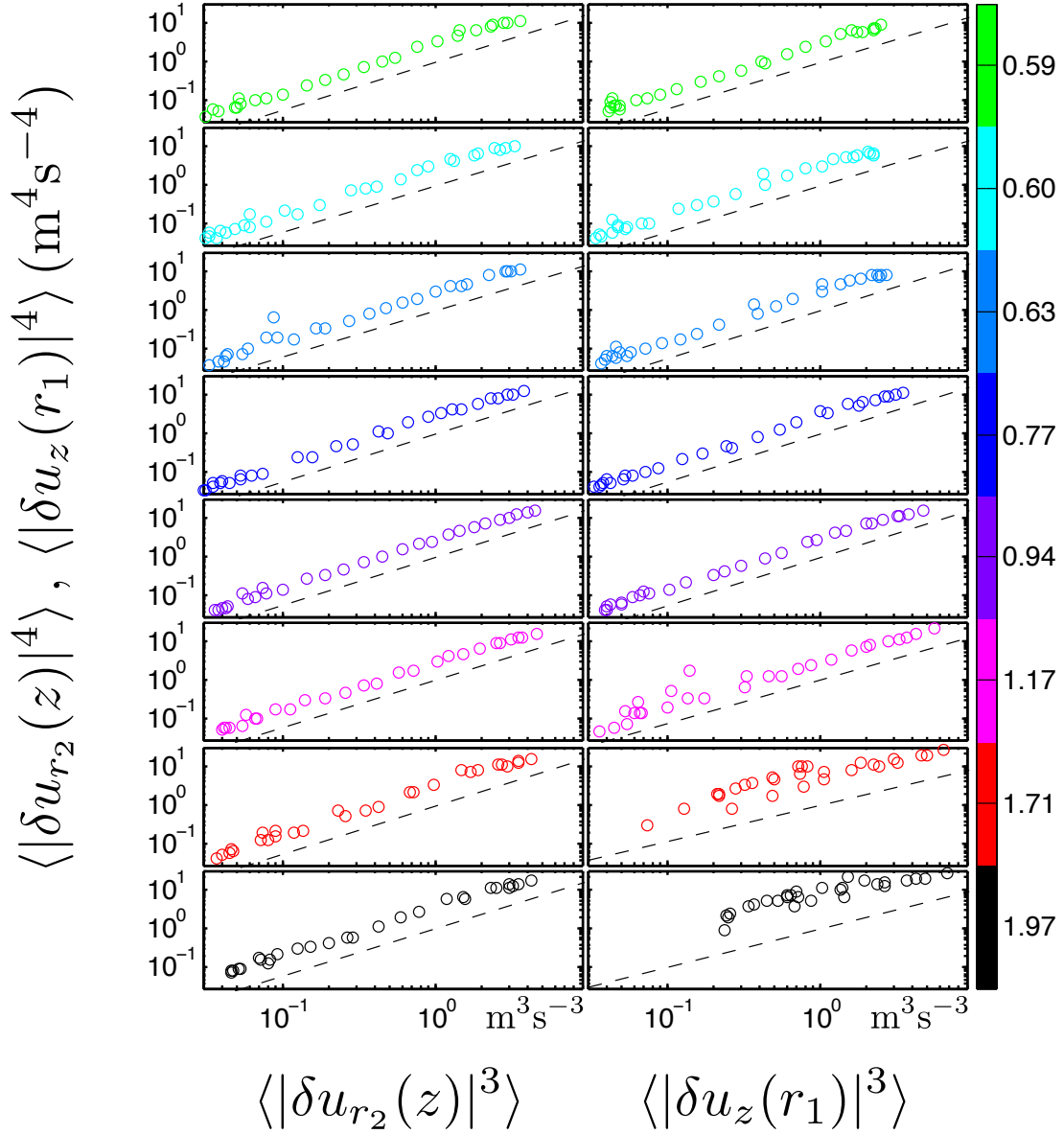


Figure 6.1: The extended-self-similarity plots for the fourth-order transverse structure functions. Dashed lines are proportional to power laws obtained from least squares fits to data. The values in the color bar are the anisotropy measured at the center of the soccer ball.

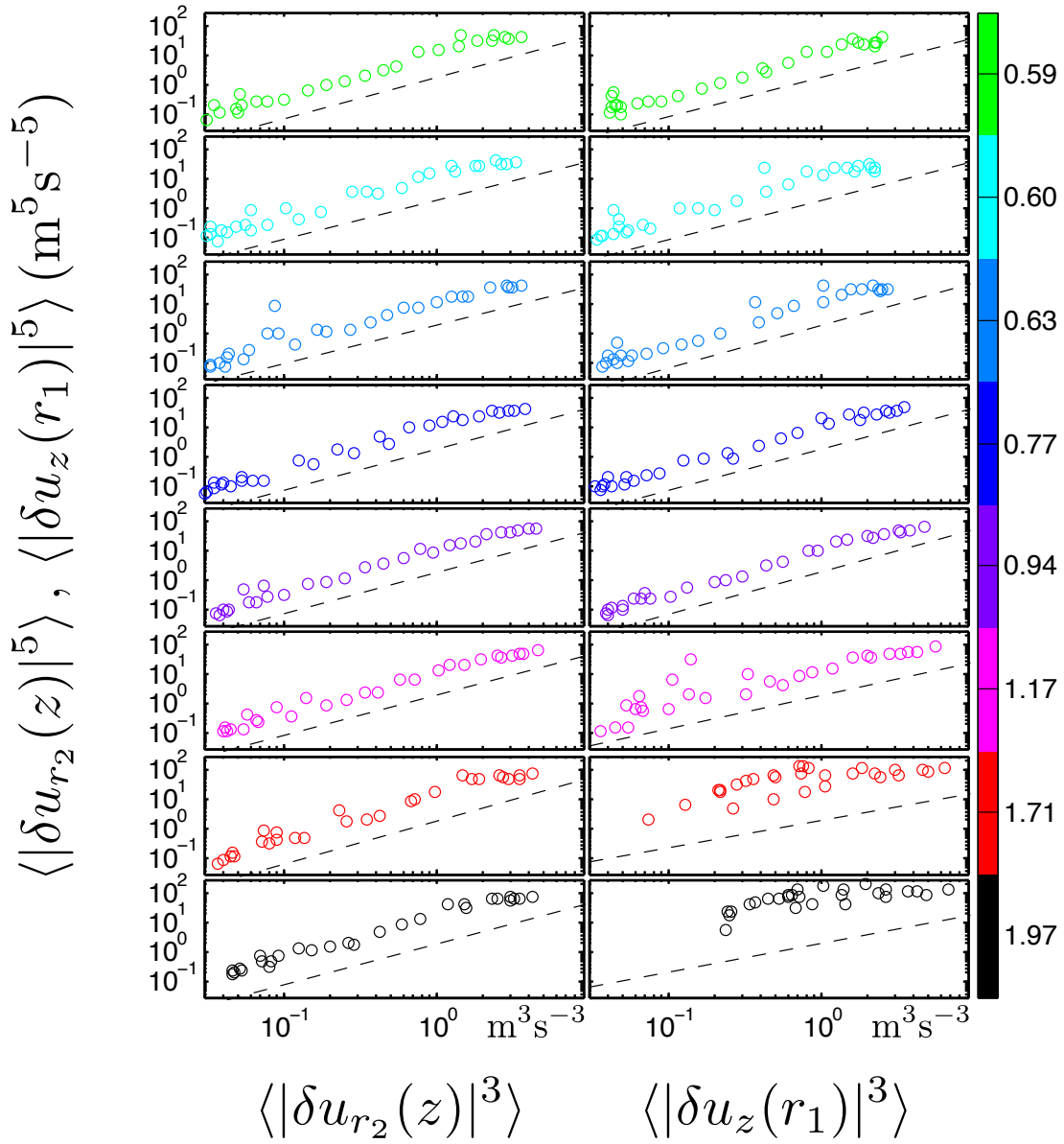


Figure 6.2: The extended-self-similarity plots for the fifth-order transverse structure functions. Dashed lines are proportional to power laws obtained from least squares fits to data. For legend, see figure 6.1.

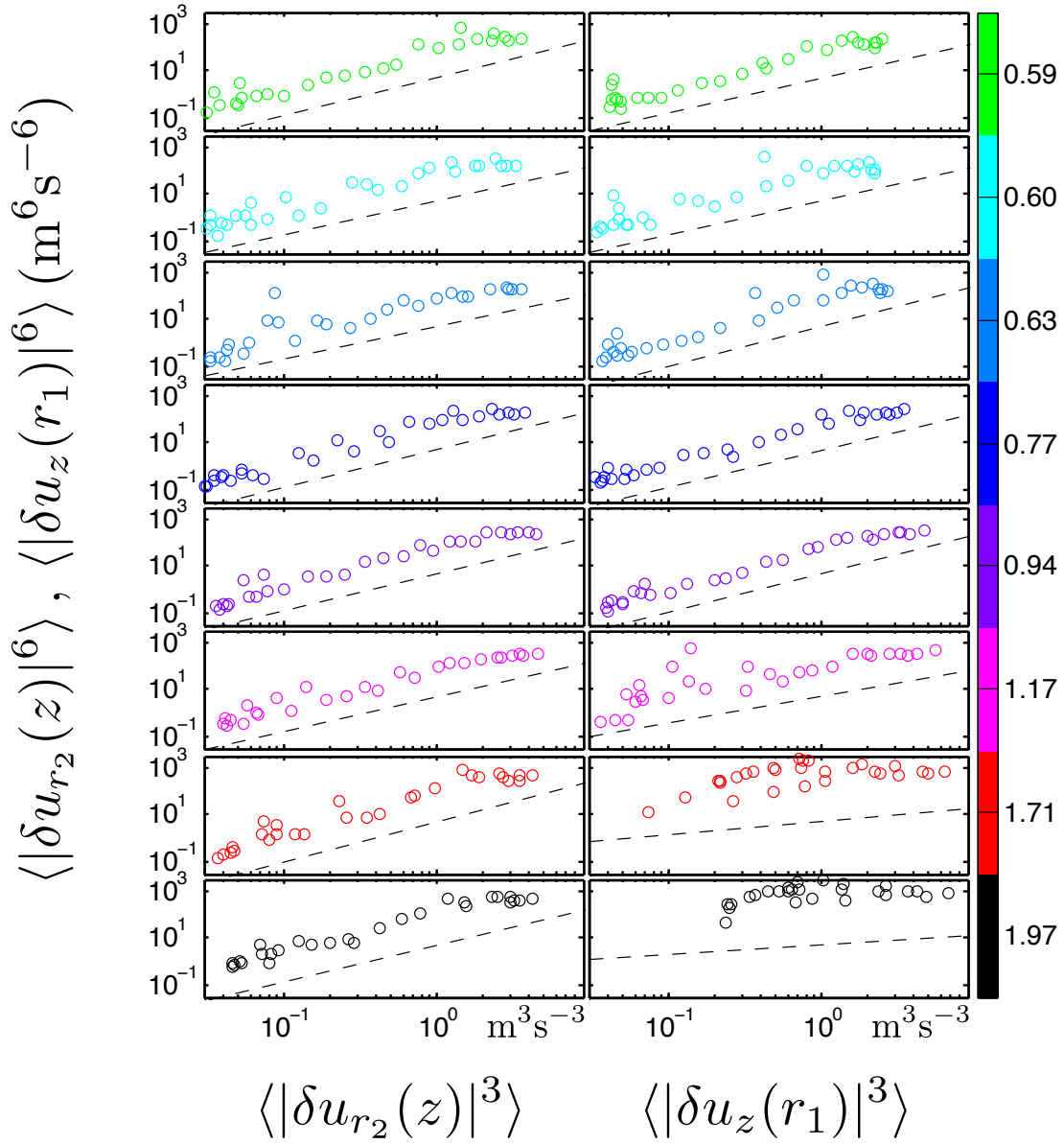


Figure 6.3: The extended-self-similarity plots for the sixth-order transverse structure functions. Dashed lines are proportional to power laws obtained from least squares fits to data. For legend, see figure 6.1.

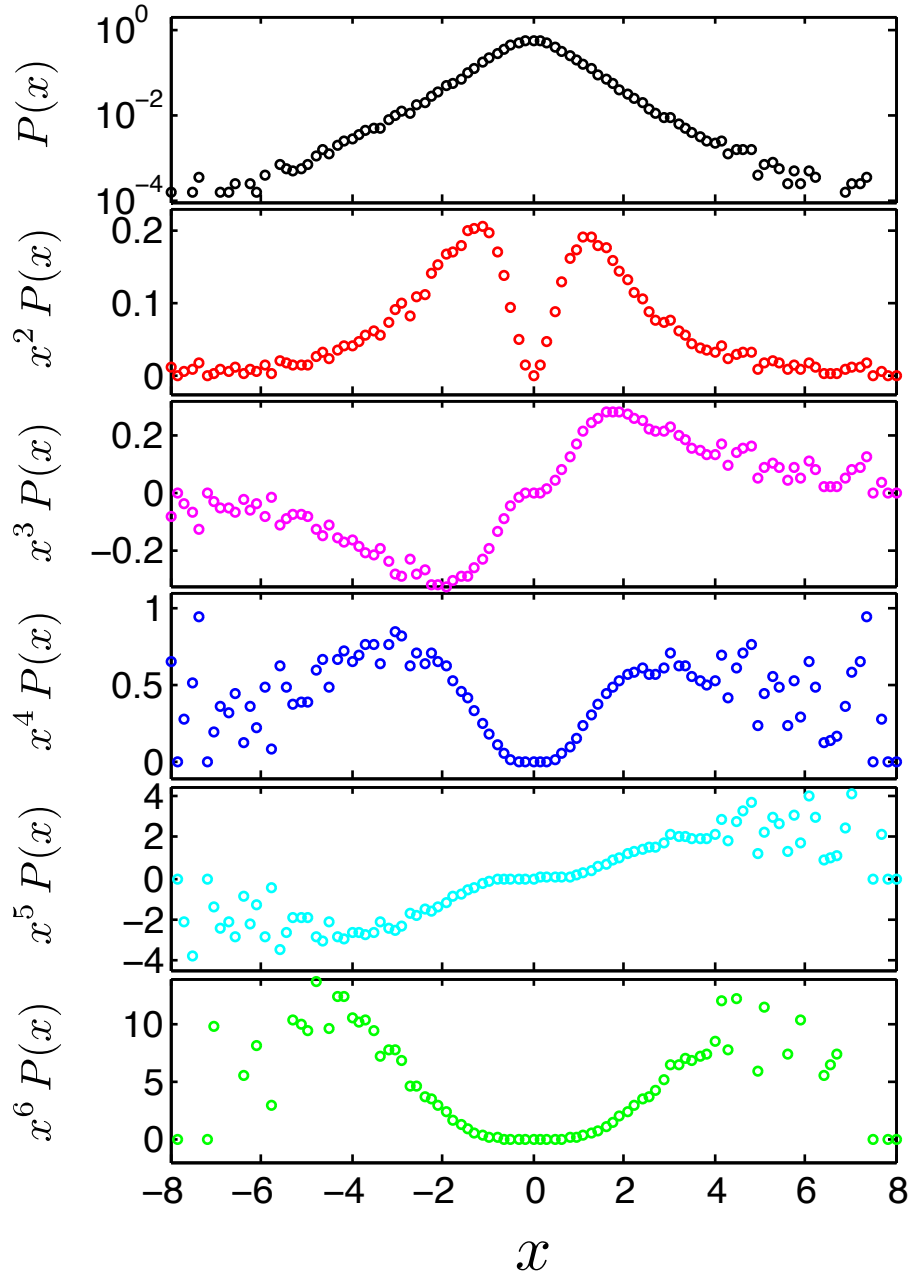


Figure 6.4: The probability density of velocity increments, $\delta u_{r_2}(z)$, and their moments for an inertial range separation $z/\eta \approx 130$ and spherically symmetric forcing, $u'_z/u'_r = 0.94$, at $R_\lambda = 480$ (see table 4.2). Here $x = \delta u_{r_2}(z)/\langle |\delta u_{r_2}(z)|^2 \rangle^{1/2}$.

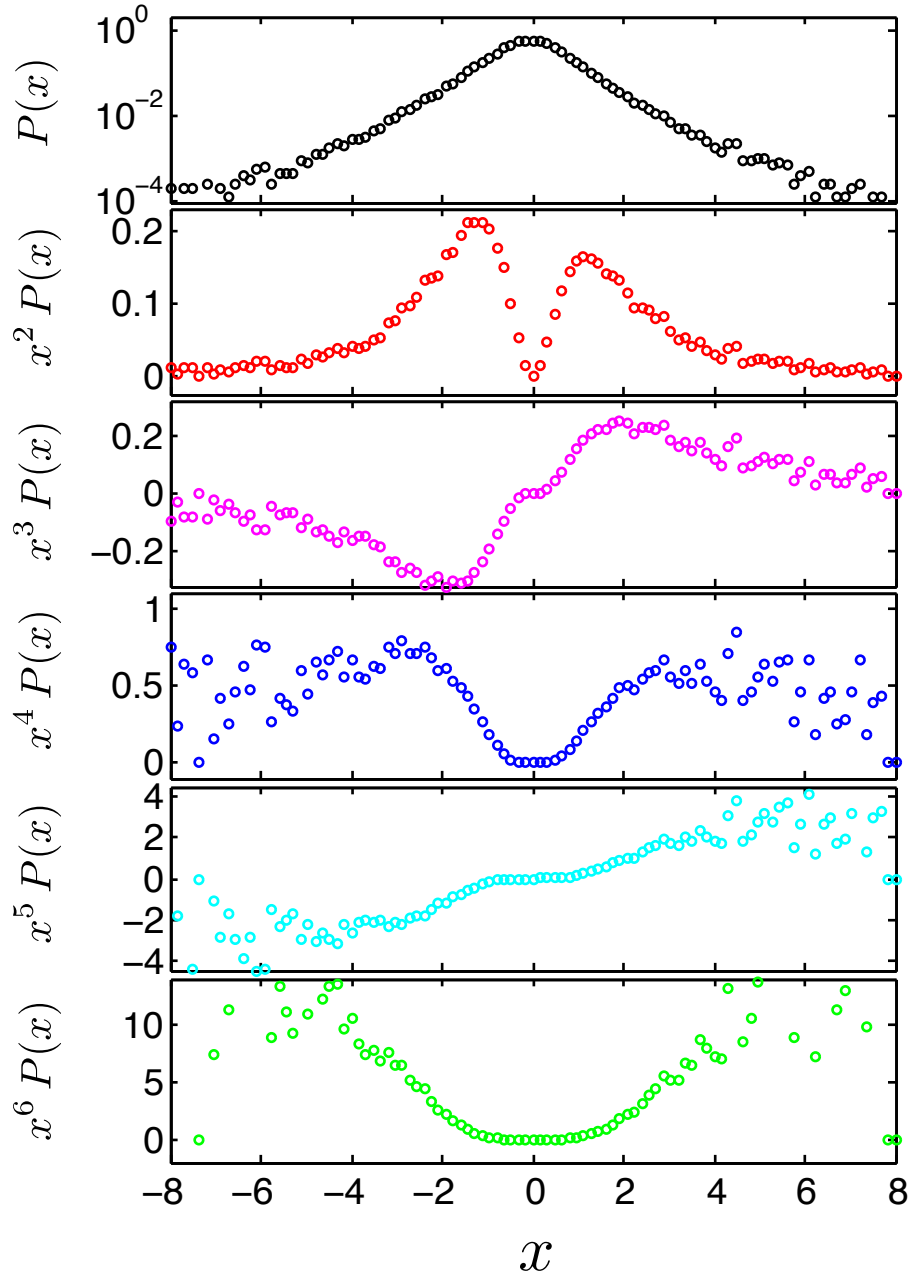


Figure 6.5: The probability density of velocity increments, $\delta u_{r_2}(z)$, and their moments for an inertial range separation $z/\eta \approx 130$ and oblate shape forcing, $u'_z/u'_r = 0.60$, at $R_\lambda = 536$ (see table 4.2). Here $x = \delta u_{r_2}(z)/\langle |\delta u_{r_2}(z)|^2 \rangle^{1/2}$.

Order of moment (n)	0	2	3	4	5	6
$(-1)^n \int_{-\infty}^0 x^n P(x) dx$	0.541	0.530	1.17	3.79	16.2	83.4
$\int_0^{\infty} x^n P(x) dx$	0.459	0.430	0.98	3.27	14.1	71.5
$\int_{-\infty}^{\infty} x^n P(x) dx$	1.00	0.96	-0.19	7.07	-2.11	154

Table 6.2: The numerical integral of the PDF and its moments from the second to the sixth order of figure 6.5. The flow anisotropy was $u'_z/u'_r = 0.60$ at $R_\lambda = 536$ (see table 4.2).

6.2 Kurtosis and hyperkurtosis of structure functions

We now turn to the normalized structure functions. When normalized by the second-order structure functions, the fourth and sixth order moments are given special names, namely the kurtosis

$$K_4(x) = \frac{\langle |\delta u(x)|^4 \rangle}{\langle |\delta u(x)|^2 \rangle^2}, \quad (6.1)$$

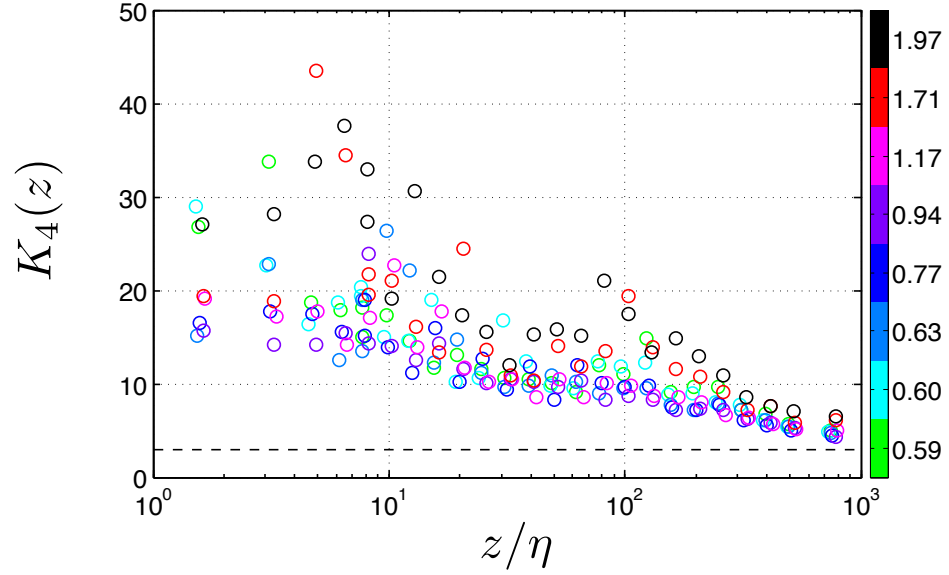
and the hyper-kurtosis

$$K_6(x) = \frac{\langle |\delta u(x)|^6 \rangle}{\langle |\delta u(x)|^2 \rangle^3}. \quad (6.2)$$

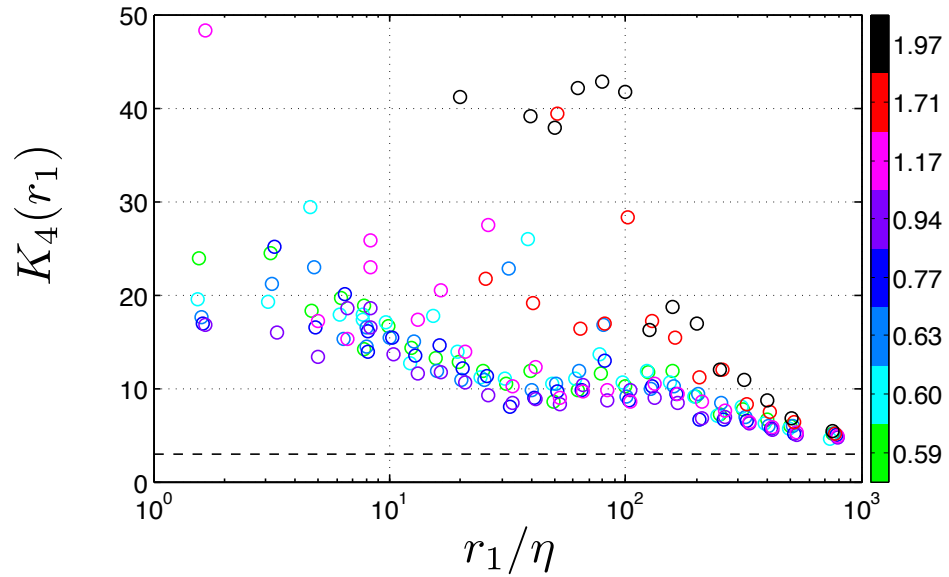
At the small scales, $K_4 > 3$ and $K_6 > 15$ because of intermittency (Frisch, 1995). At the large scales the PDF of δu follows a normal distribution and $K_4 = 3$ and $K_6 = 15$.

The measurements for the normalized axial and radial structure functions, $K_4(z)$, $K_4(r_1)$, $K_6(z)$, and $K_6(r_1)$, are shown in figures 6.6 and 6.7. It is evident that our flows were highly intermittent at the small scales. Both K_4 and K_6 showed trends of decreasing to the gaussian values of 3 and 15, respectively. Shen and Warhaft (2000) and Garg and Warhaft (1998) have shown that K_4 and K_6 in sheared and nonsheared turbulent flows asymptote to the same limits at

the integral scale, approximately at 2000η . If we can extend our measurement that far out, K_4 and K_6 in our experiment may continue to decrease and eventually reach their respective gaussian values. This is not physically possible in our experiment because 2000η would correspond to a distance of about 0.3 m, which is very close to the boundary of the apparatus where the anisotropy of the flow is heavily influenced by the confining walls rather than by the anisotropy of the agitation. What we gain by generating a stationary turbulent flow with negligible mean within confining walls we lose by having a finite extend in our turbulent region. Nevertheless, it is remarkable that K_4 and K_6 in our flow show downward trends toward their gaussian values similar to those observed in the wind tunnel. Shen and Warhaft (2000) also noted the presence of a small bump at 200η and attributed this to the scatter in the data. This bump was also noticeable in our measurements of K_4 and K_6 , albeit at 100η . The magnitude of this bump was as large as the scatter and may have evaded detection in experiments. We are only able to find another instance of the appearance of this bump at approximately 150η in the measurement of Siebert et al. (2010) in the turbulent region of stratocumulus clouds at $R_\lambda \approx 5000$. We note that the scale at which the bump occurs approximately coincides with the Taylor scales, $\lambda = 15^{1/4} R_\lambda^{1/2} \eta$ (see e.g. Pope (2000), page 200, for a derivation of λ), which were 40η , 60η , and 140η for $R_\lambda = 480$, 934 , and 5000 , respectively. From the numerical experiments of Donzis and Sreenivasan (2010), we infer that the second order structure functions at $R_\lambda = 140 - 1000$ reach a plateau at around the Taylor scales $\lambda = 20 \eta - 60 \eta$. Thus, we speculate that the reason for the occurrence of this bump may be due to transition range dynamics.

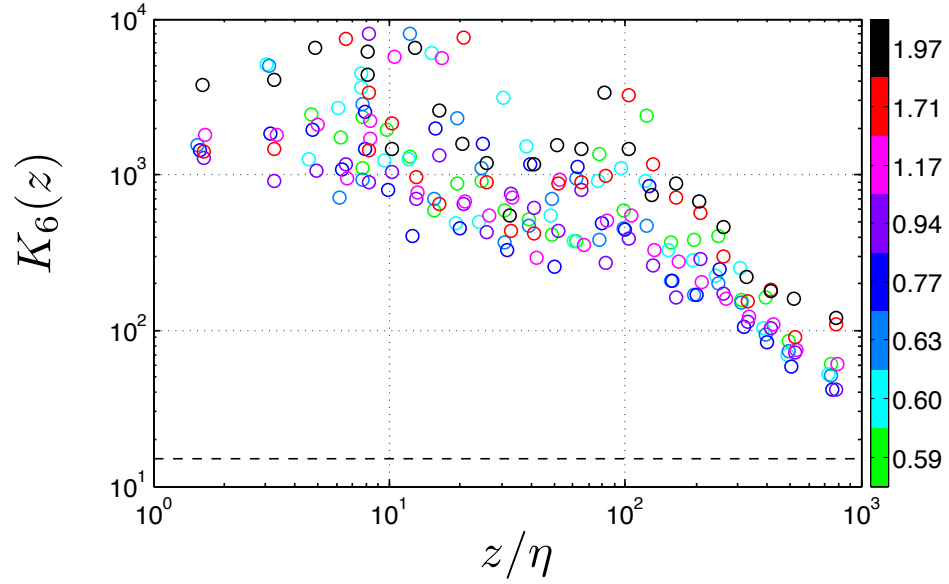


(a)

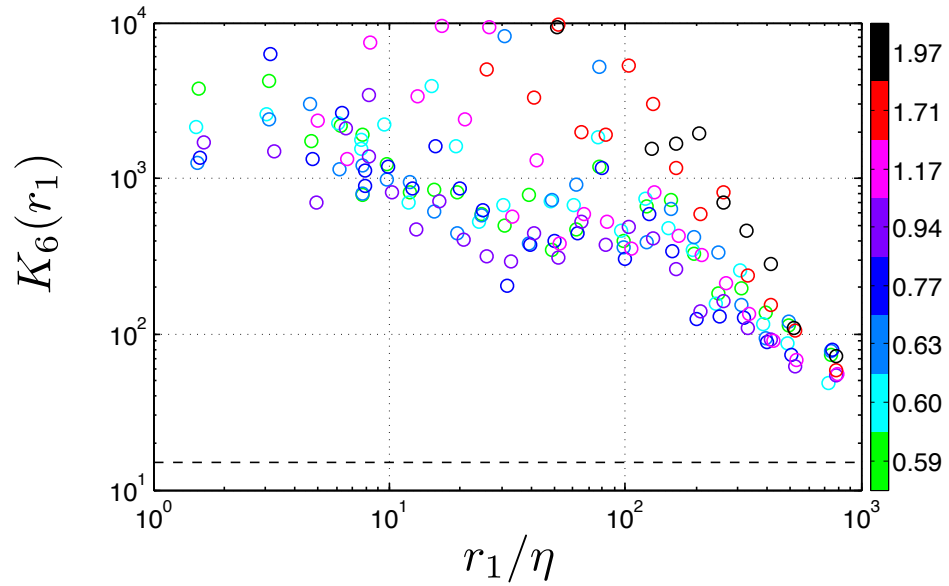


(b)

Figure 6.6: The kurtoses as a function of separations. (a) The axial kurtoses, $K_4(z) = \langle |\delta u_{r_2}(z)|^4 \rangle / \langle |\delta u_{r_2}(z)|^2 \rangle^2$, and (b) the radial kurtoses $K_4(r_1) = \langle |\delta u_z(r_1)|^4 \rangle / \langle |\delta u_z(r_1)|^2 \rangle^2$. The dashed lines are at the gaussian value of 3. The values in the color bar are the anisotropy measured at the center of the soccer ball. Error bars (not shown) are smaller than the symbols.



(a)



(b)

Figure 6.7: The hyper-kurtoses as a function of separations. (a) shows $K_6(z) = \langle |\delta u_{r_2}(z)|^6 \rangle / \langle |\delta u_{r_2}(z)|^2 \rangle^3$ and (b) shows $K_6(r_1) = \langle |\delta u_z(r_1)|^6 \rangle / \langle |\delta u_z(r_1)|^2 \rangle^3$. The dashed lines are at the gaussian value of 15. The values in the color bar are the anisotropy measured at the center of the soccer ball. Error bars (not shown) are smaller than the symbols.

6.3 Higher order scaling exponents

Here, we document the inertial range scaling exponents of higher order structure functions. The method for obtaining the higher order scaling exponents is the same as in section 5.2. We calculated the slopes obtained from straight-line fits, $\log\langle|\delta u(x)|^n\rangle \sim \log\langle|\delta u(x)|^3\rangle$, to the data shown in figures 6.1, 6.2, and 6.3. Tables 6.3, 6.4, and 6.5 list the values for the axial and radial scaling exponents, $\zeta_p^{(z)}$ and $\zeta_p^{(r)}$, for $p = 4, 5$, and 6. The radial structure functions for $u'_z/u'_r = 1.71$ and 1.98 were very noisy and the scatter in these two data sets might have been due to a residual shear in the turbulence or an insufficiently developed turbulent region. The errors in all the exponents were estimated with the standard error of the slopes in the straight-line fits (see appendix B). Within the experimental error, we found that the values of the exponents are in fair agreement with those found in the literature (see section 6.4).

We now examine the ratio of radial to axial exponents for order 4 and 5. In figures 6.8 and 6.9, we plot $\zeta_4^{(r)}/\zeta_4^{(z)}$ and $\zeta_5^{(r)}/\zeta_5^{(z)}$ against anisotropy, u'_z/u'_r . Because the majority of the ratios between radial and axial exponents are close to one, we conjecture that $\zeta_p^{(r)}$ and $\zeta_p^{(z)}$ are equal in anisotropic turbulence. We note that Ouellette (2006) measured the Lagrangian scaling exponents up to the tenth order in a von Kármán counter-rotating flow and found that the axial and radial exponents are the same to within experimental accuracy. Thus, our investigation here concerning the equality of Eulerian scaling exponents forms an extension to the above work.

u'_z/u'_r	$\zeta_4^{(r)}$	$\zeta_4^{(z)}$	$\zeta_4^{(r)}/\zeta_4^{(z)}$
0.59 ± 0.03	1.186 ± 0.021	1.220 ± 0.017	0.972 ± 0.031
0.60 ± 0.02	1.189 ± 0.027	1.184 ± 0.020	1.005 ± 0.040
0.63 ± 0.03	1.223 ± 0.023	1.173 ± 0.038	1.043 ± 0.053
0.77 ± 0.03	1.213 ± 0.012	1.216 ± 0.013	0.998 ± 0.021
0.94 ± 0.04	1.227 ± 0.011	1.215 ± 0.015	1.010 ± 0.021
1.16 ± 0.05	1.098 ± 0.049	1.199 ± 0.013	0.916 ± 0.051
1.71 ± 0.10	0.923 ± 0.486	1.231 ± 0.022	0.750 ± 0.400
1.98 ± 0.10	0.989 ± 0.629	1.199 ± 0.016	0.824 ± 0.535

Table 6.3: The values of the fourth order radial and axial scaling exponents, $\zeta_4^{(r)}$ and $\zeta_4^{(z)}$, measured in our experiment using ESS. The last column shows the ratio between the two.

u'_z/u'_r	$\zeta_5^{(r)}$	$\zeta_5^{(z)}$	$\zeta_5^{(r)}/\zeta_5^{(z)}$
0.59 ± 0.03	1.338 ± 0.052	1.407 ± 0.043	0.951 ± 0.066
0.60 ± 0.02	1.327 ± 0.072	1.312 ± 0.049	1.011 ± 0.092
0.63 ± 0.03	1.441 ± 0.061	1.290 ± 0.082	1.117 ± 0.118
0.77 ± 0.03	1.394 ± 0.032	1.403 ± 0.036	0.993 ± 0.048
0.94 ± 0.04	1.429 ± 0.029	1.396 ± 0.039	1.023 ± 0.050
1.16 ± 0.05	1.118 ± 0.099	1.355 ± 0.036	0.825 ± 0.095
1.71 ± 0.10	0.923 ± 0.852	1.458 ± 0.054	0.633 ± 0.608
1.98 ± 0.10	0.989 ± 1.102	1.373 ± 0.038	0.720 ± 0.822

Table 6.4: The numerical data for the fifth order radial and axial scaling exponents, $\zeta_5^{(r)}$, $\zeta_5^{(z)}$, and the ratio between the two.

6.4 Anomalous scaling

We now turn to the issue of how the transverse scaling exponents, ζ_p , vary with order, p . In the absence of intermittency, Kolmogorov scaling predicts a linear relationship between ζ_p and p , see equation 1.49. Figure 6.10 and table 6.6 show the mean of ζ_p in tables 5.1, 6.3, 6.4, and 6.5 as a function of p . The error bars were

u'_z/u'_r	$\zeta_6^{(r)}$	$\zeta_6^{(z)}$	$\zeta_6^{(r)}/\zeta_6^{(z)}$
0.59 ± 0.03	1.490 ± 0.085	1.584 ± 0.076	0.941 ± 0.099
0.60 ± 0.02	1.447 ± 0.120	1.424 ± 0.082	1.017 ± 0.143
0.63 ± 0.03	1.668 ± 0.104	1.395 ± 0.127	1.196 ± 0.183
0.77 ± 0.03	1.562 ± 0.055	1.584 ± 0.067	0.986 ± 0.076
0.94 ± 0.04	1.630 ± 0.051	1.570 ± 0.069	1.038 ± 0.078
1.16 ± 0.05	1.131 ± 0.144	1.499 ± 0.063	0.754 ± 0.128
1.71 ± 0.10	0.583 ± 0.170	1.696 ± 0.090	0.344 ± 0.119
1.98 ± 0.10	0.426 ± 0.175	1.544 ± 0.062	0.276 ± 0.124

Table 6.5: The numerical data for the sixth order radial and axial scaling exponents, $\zeta_6^{(r)}$, $\zeta_6^{(z)}$, and the ratio between the two.

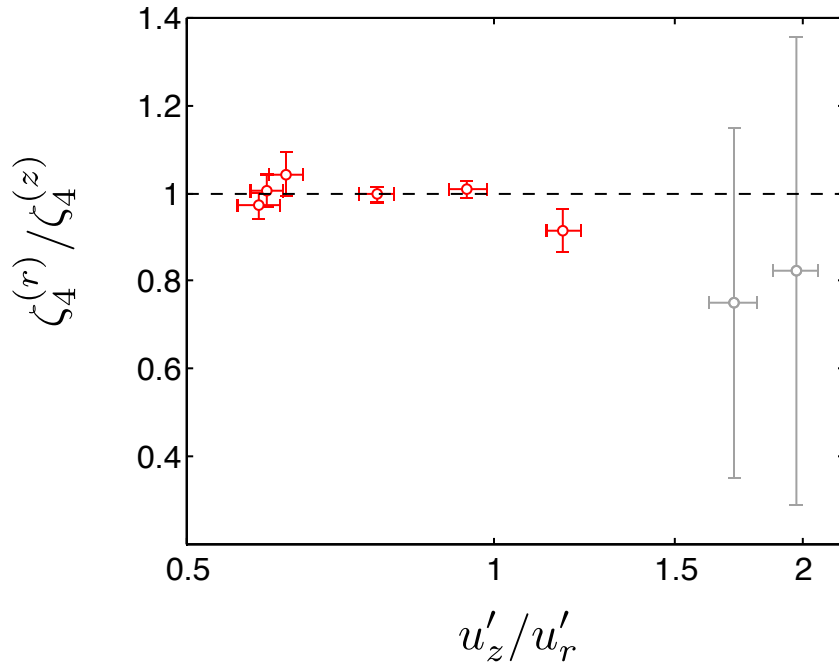


Figure 6.8: The figure shows $\zeta_4^{(r)}/\zeta_4^{(z)}$, the ratio between the fourth-order scaling exponents of the radial structure functions and those of the axial structure functions. The last two points with large uncertainties due to spatial resolution are marked in gray.

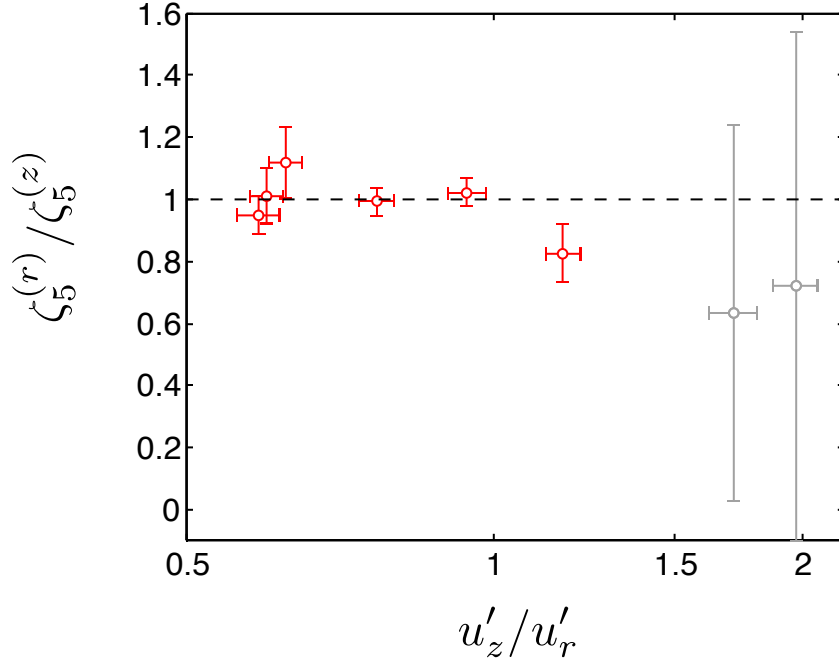


Figure 6.9: The figure shows $\zeta_5^{(r)} / \zeta_5^{(z)}$, the ratio between the fifth-order scaling exponents of the radial structure functions and those of the axial structure functions. The last two points with large uncertainties due to spatial resolution are marked in gray.

the standard deviation of the values of ζ_p in each table. Our observation is that, within this error, the exponents show an anomalous scaling (departure from Kolmogorov prediction), similar to what is observed for the scaling exponents measured in a nonsheared wind tunnel homogeneous and isotropic turbulent flow at an R_λ of 134 (Shen and Warhaft, 2002). The values of both sets of exponents are below the values obtained by Shen and Warhaft (2002) at an R_λ of 863. The difference is less than 6% at the fourth order and increases monotonically up to about 13% at the sixth order. We suspect that the reason for the difference is a combination of Reynolds number and large scale anisotropy effects. We believe that if we could achieve higher Reynolds numbers, the values of the scaling exponents would increase.

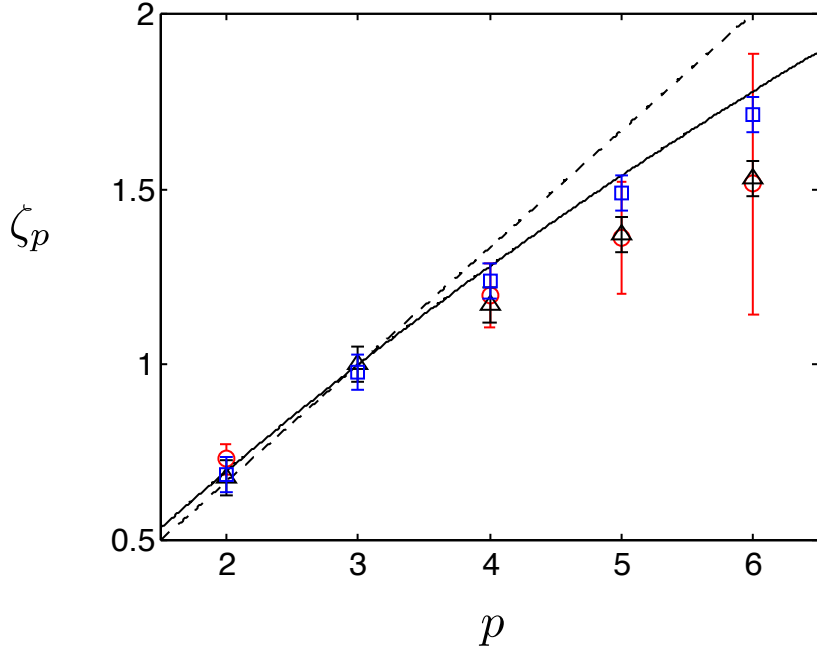


Figure 6.10: The circular symbols (\circ) are our measurements of the inertial range scaling exponents, ζ_p , of the transverse structure functions using ESS method. The triangular symbols (\triangle) are the exponents measured by Shen and Warhaft (2002) in an unsheared wind tunnel homogeneous and isotropic turbulent flow at an R_λ of 134, and the square symbols (\square) are those measured by them at an R_λ of 863. The dashed line is the Kolmogorov prediction (equation 1.49). The solid line is the She-Leveque prediction (equation 1.54).

6.5 Conclusions

We studied the influence of the large scale anisotropy on the structure functions of order 4, 5, and 6. We found indications that anisotropy in the velocity field intensifies the asymmetry of the probability density of the velocity increments. We have shown that the small scales of the flows are highly intermittent, as indicated by the measurements of the kurtosis and hyper-kurtosis, and that both kurtosis and hyper-kurtosis asymptote to their gaussian limits at the large scales. Within the experimental uncertainty, we found evidence that the scal-

Order p	R_λ		
	480 Present work	134 S&W (2002)	863 S&W (2002)
2	0.731 ± 0.017	0.68 ± 0.05	0.69 ± 0.05
3	1	1.00 ± 0.05	0.98 ± 0.05
4	1.198 ± 0.088	1.17 ± 0.05	1.24 ± 0.05
5	1.360 ± 0.167	1.37 ± 0.05	1.49 ± 0.05
6	1.516 ± 0.096	1.53 ± 0.05	1.71 ± 0.05

Table 6.6: The inertial range transverse scaling exponents, ζ_p , measured in the current experiment using the ESS method and those measured by Shen and Warhaft (2002), denoted as S&W (2002) above, in an unsheared wind tunnel homogeneous and isotropic turbulent flow at two different R_λ of 134 and 863.

ing exponents measured using the ESS method are independent of anisotropy. The exponents showed a departure from the Kolmogorov prediction and their values were below those measured in a nonsheared wind tunnel homogeneous turbulent flow at an R_λ of 863 (Shen and Warhaft, 2002). This is a subtle difference and we believe the difference would become smaller if we increase the Reynolds number.

CHAPTER 7

THE INTEGRAL SCALES OF TURBULENCE

Recently, there is increasing evidence to suggest that macroscopic properties of a turbulent flow are linked to the turbulence energy spectrum. Some of the macroscopic properties considered include the cross-sectional mean velocity of gravity-driven open channel flows (Gioia and Bombardelli, 2001), the depth of turbulent cauldron (Gioia and Bombardelli, 2005), the friction factor (Gioia and Chakraborty, 2006; Guttenberg and Goldenfeld, 2009; Tran et al., 2010), and the mean-velocity profile of pipe flows (Gioia et al., 2010). The authors established their findings based on the assumption that Kolmogorov's theory for homogeneous and isotropic turbulence is also applicable to anisotropic and inhomogeneous flows (Knight and Sirovich, 1990; Moser, 1994; Lundgren, 2003). They explain their findings in terms of the varying habits of momentum transfer with varying sizes of turbulent eddies. Here, we study the physical space equivalent of the spectrum – the correlation of velocity fluctuations separated in space. Our results highlight the interesting feature that correlation functions measured in different flow directions collapse onto one self-similar curve when appropriately scaled with the anisotropy that drives the turbulence at the large scale. The scaling form allows us to express the integral length, which is representative of the length scale of the most energetic eddies (Batchelor (1956), chapter 6), as a power law of its characteristic velocity, with an exponent related to the inertial range scaling exponent. Our work complements the existing studies and suggests that self-similarity and Kolmogorov theory are relevant to the

phenomenological description of the large scale of anisotropic turbulent flows.

7.1 The integral scale and correlation function

We begin with a brief introduction to the integral length of the correlation function in order to facilitate the discussion that follows.

As described in the introductory chapter, an important tenet in the Richardson picture of the turbulence energy cascade is that the energy dissipation rate per unit mass in a turbulent flow is finite (see e.g. Frisch (1995), 5.2). This is summarized in the following empirical law (Taylor, 1935)

$$\epsilon = \frac{A u'^3}{L}. \quad (7.1)$$

Here, A is a number of order unity, u' is a velocity scale characteristic of the most energetic eddies, and L their characteristic length scales. This order of magnitude assumption has found support from a theoretical consideration by Lohse (1994). Starting from an energy balance equation derived from the Navier-Stokes equation with a mean field approach, Lohse (1994) showed that $A \approx (a/C_2)^{3/2}$, where C_2 is the Kolmogorov constant for the second-order structure function (see equations 1.19 and 1.20) and $a \approx 1.25$. Recent updates on the empirical law of energy dissipation rate can be found in Sreenivasan (1984) and Pearson et al. (2002). A simple interpretation of the above empirical law is that the decay time of the turbulence is a few characteristic periods of the most energetic eddies (Batchelor (1956), 6.1). Identifying u' with the RMS velocity fluctuation, u'^2/ϵ can be regarded as the time scale of the decay of energy, and L/u' can be regarded as the characteristic period of the most energetic eddies.

The above empirical relation has found wide use in estimating the energy

dissipation rate of turbulent flows. Measuring u' is relatively simple. Single-point measurements of the turbulent velocity fluctuation suffice to yield u' . In contrast to u' , measuring L is not so straightforward because it is not directly accessible (see e.g. Batchelor (1956), appendix to 6.1). If we consider the three-dimensional energy spectrum, $\Phi(k)$, it is permissible to think of the part of the function around the maximum, at wavenumber κ_0 , as responsible for supplying energy into the flow (the most energetic eddies). The reciprocal of the wavenumber at which this maximum occurs, $L_E = 1/\kappa_0$, then characterizes the principal energy bearing part of the spectrum (the most energetic eddies). On the other hand, if the contribution from higher wavenumbers is negligible, we may approximate L with the transverse integral length (see e.g. Batchelor (1956))

$$L_g = \frac{3\pi}{8} \frac{\int_0^\infty \kappa^{-1} \Phi(\kappa) d\kappa}{\int_0^\infty \Phi(\kappa) d\kappa}, \quad (7.2)$$

which, for isotropic turbulence, is related to the one-dimensional transverse correlation function in the following way

$$L_g = \int_0^\infty g(r) dr. \quad (7.3)$$

Here, $g(r)$ is the diagonal element of the much more general correlation tensor

$$g_{ij}(\mathbf{r}) = \frac{\langle u'_i(\mathbf{r}) u'_j(0) \rangle}{\sqrt{\langle u_i'^2(\mathbf{r}) \rangle \langle u_j'^2(0) \rangle}}, \quad (7.4)$$

which is the velocity correlation tensor introduced in section 1.1 normalized by the fluctuations. The careful reader may note that, in general, the velocity fluctuations are functions of space and time. The time dependence of the fluctuations, and consequently $g_{ij}(\mathbf{r})$, has been suppressed for the simplicity of discussion. If the velocity field satisfies the homogeneity and isotropy conditions, then the correlation tensor can be expressed in terms of two scalar functions (Batchelor

(1956), 3.4). With reference to experimental work, we usually make the choice $\mathbf{r} = r\mathbf{e}_1$ and introduce the longitudinal correlation function

$$f(r) = g_{11}(r), \quad (7.5)$$

and the transverse correlation functions

$$g(r) = g_{22}(r) = g_{33}(r). \quad (7.6)$$

In this way, we obtain the form for the correlation tensor first derived by Kármán and Howarth (1938) and systematically formulated by Robertson (1940)

$$g_{ij}(\mathbf{r}) = g(r) \delta_{ij} + [f(r) - g(r)] \frac{r_i r_j}{r^2}. \quad (7.7)$$

$f(r)$ and $g(r)$ are related by the continuity equation in much the same way as the longitudinal and transverse structure functions are (e.g. Pope, 2000). Relevant to our experiments are the following two transverse correlation functions

$$g_{r_2 r_2}(0, 0, z) = \frac{\langle u'_{r_2}(0, 0, z) u'_{r_2}(0, 0, 0) \rangle}{\sqrt{\langle u'^2_{r_2}(0, 0, z) \rangle \langle u'^2_{r_2}(0, 0, 0) \rangle}}, \quad (7.8)$$

$$g_{zz}(r_1, 0, 0) = \frac{\langle u'_z(r_1, 0, 0) u'_z(0, 0, 0) \rangle}{\sqrt{\langle u'^2_z(r_1, 0, 0) \rangle \langle u'^2_z(0, 0, 0) \rangle}}. \quad (7.9)$$

They are related simply to the structure functions by expanding the product in equation 1.30

$$g(x) = \frac{1}{2} \left[\sqrt{\frac{\langle u'^2(x) \rangle}{\langle u'^2(0) \rangle}} + \sqrt{\frac{\langle u'^2(0) \rangle}{\langle u'^2(x) \rangle}} - \frac{D(x)}{\sqrt{\langle u'^2(x) \rangle \langle u'^2(0) \rangle}} \right], \quad (7.10)$$

which, under the assumption of homogeneity $\langle u'^2(x) \rangle = \langle u'^2(0) \rangle = u'^2$, reduces to

$$g(x) = 1 - \frac{D(x)}{2u'^2}. \quad (7.11)$$

Here, x is understood to represent z or r_1 . Given that L_g is an important control parameter in aerodynamic stability analyses of bridges with sharp edges (e.g.

Fransos and Bruno, 2010), as well as being a key parameter in the design of gas turbine engines (e.g. Van Fossen and Ching, 1994; Van Fossen et al., 1995; Barrett and Hollingsworth, 2001; Carullo et al., 2011), a more fundamental understanding of L_g , and thus of $g(r)$, is needed.

7.2 Scaling and self-similarity

There is no rigorous theory that yields the shape for the longitudinal and transverse correlation functions in fully developed turbulence, but we have a rough picture of how these curves should look like from experiments (e.g. Comte-Bellot and Corrsin, 1971) and numerical simulations (e.g. Kim et al., 1987). Batchelor and Townsend (1948) studied the decay of turbulence and showed that in the final period of decay of the turbulence, when the effects of inertial forces are negligible, the longitudinal correlation function asymptotes to a self-similar function

$$f(r, t) = \exp\left(-\frac{r^2}{8\nu t}\right), \quad (7.12)$$

corroborating the hypothesis made by Kármán and Howarth (1938) (for more details on the self-preservation hypothesis, see e.g. Monin and Yaglom (1975), 16). Temporally self-similar correlation functions were also derived analytically in decay problems of Burgers turbulence (Gurbatov et al., 1997) and passive scalar in Kraichnan's model (Eyink and Xin, 2000). Ewing et al. (2007) examined the correlation function of streamwise velocity component in the far field of an axisymmetric jet and showed that the similarity solutions of the governing equations for the correlation functions depend only on the separation distance between the points in the streamwise similarity coordinate, namely $\psi' - \psi$, where the similarity coordinate $\psi = \ln x$ is measured from a virtual origin in

space x . The spatial self-similarity of correlation functions in anisotropic turbulence considered here complements the existing works.

The similarity argument to be presented here is a special case of Widom's scaling (see e.g. Huang (1987), 16.5) with the dimension of homogeneity d equals zero (Eyink, 2011), and is in the same vein as Goldenfeld (2006). Two notable features of this approach are the universal scaling function that governs the correlation function and the reduction of the number of variables in the function. The scaling form we propose for the transverse correlation function is

$$g(x, u') = \mathcal{G}(x u'^{\beta}), \quad (7.13)$$

where $\mathcal{G}(\xi)$ is a universal scaling function of a single variable ξ , and β is an exponent to be determined. To determine β , we connect the scaling function $\mathcal{G}(\xi)$ to that in the inertial range. We note that $g(x, u')$ scales as

$$g(x, u') \propto \frac{x^{\zeta}}{u'^2}, \quad (7.14)$$

in the inertial range. This can be seen by substituting the inertial range scaling of the structure function, $D(x) \propto x^{\zeta}$, into equation 7.11. This requires that $\mathcal{G}(\xi) \propto \xi^{\zeta}$, in the inertial range, and therefore $\beta = -2/\zeta$. Thus, the scaling form for the correlation function is

$$g(x, u') = \mathcal{G}(x u'^{-2/\zeta}). \quad (7.15)$$

The scaling form predicts that correlation functions will collapse onto a single curve when plotted as g against $x u'^{-2/\zeta}$.

The scaling form in 7.15 implies a relationship between the integral length and the large scale velocity fluctuation. By changing the variable of integration to $\xi = x u'^{-2/\zeta}$, we obtain

$$L = u'^{2/\zeta} \mathcal{J}, \quad (7.16)$$

where $\mathcal{I} = \int_0^\infty \mathcal{G}(\xi) d\xi$ is a constant which may depend on some other parameters of the flow, e.g. R_λ or ζ . This dependence can be eliminated if we form the ratio of two integral scales obtained from two different correlation functions

$$\frac{L_1}{L_2} = \left(\frac{u'_1}{u'_2} \right)^{2/\zeta}. \quad (7.17)$$

We cannot test these predictions in isotropic turbulence because the correlation functions and RMS velocity fluctuation are isotropic by definition. If we can drive the flow away from isotropy, as we can in our flow generator, we can test these predictions.

7.3 Integral length scaling

Figure 7.1 shows 8 pairs of correlation functions, $g_{r_2 r_2}(z)$ and $g_{zz}(r_1)$, obtained in 8 different flows with different large scale anisotropies, but with approximately the same energy dissipation rate and Reynolds number. We found that correlation functions measured in different directions in anisotropic flows were different when plotted against separation. Note that we normalized the correlation functions by the velocity fluctuations at both points, 0 and r_1 (or z), although homogeneity would allow us to set them equal, because it compensated for the small inhomogeneity of our flow. In addition, we divided the correlation functions by their values at zero separation, that is, when the distance between probe volumes was zero. The values of the correlations at zero separation were not equal to one because of noise in the signals, but were approximately equal to 0.98, for all correlation functions.

In order to test equation 7.17, we need to estimate the integral scale. Batchelor (1948) observed that transverse correlation functions cross zero before they

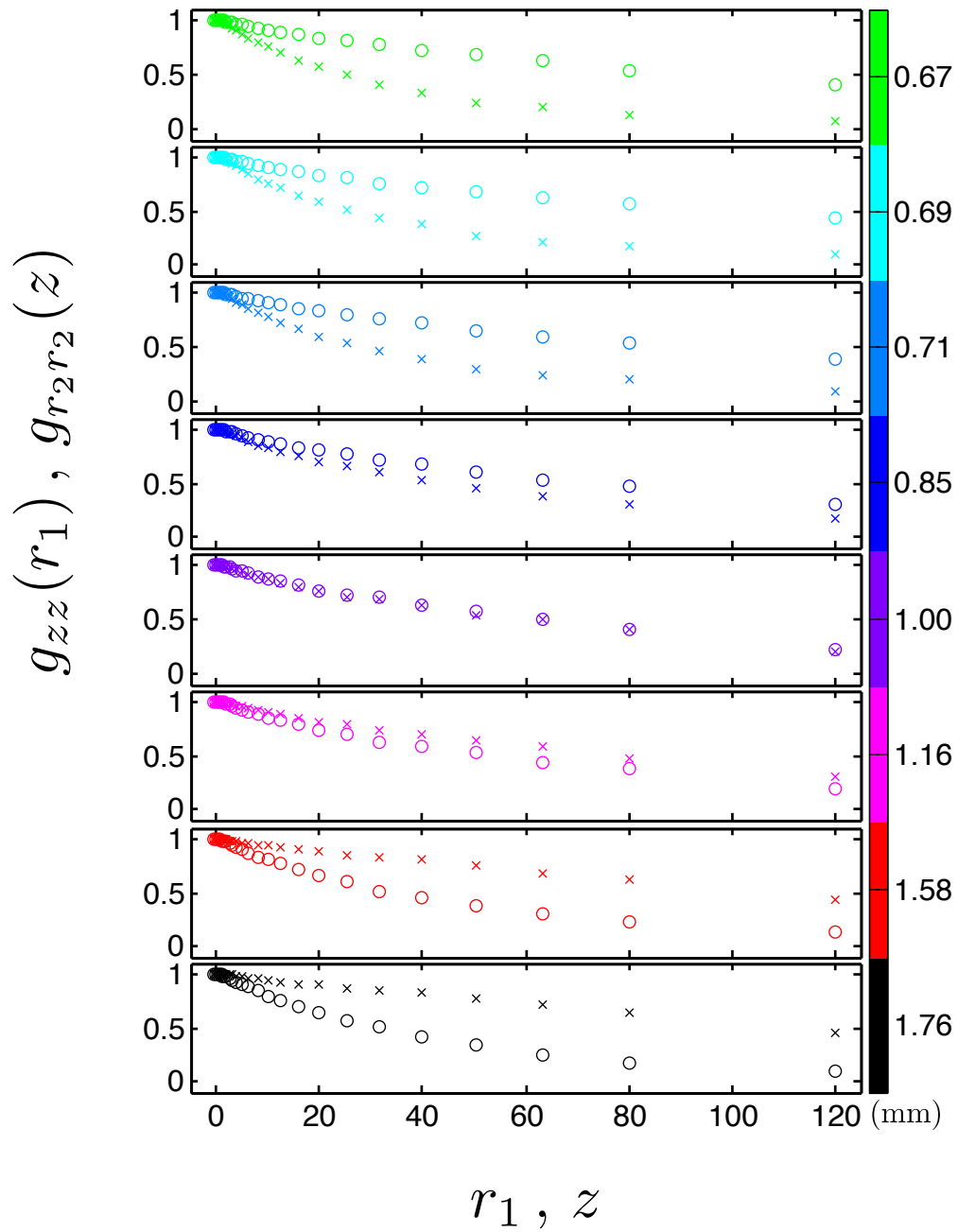


Figure 7.1: The figure shows the 8 pairs of transverse correlation functions obtained in 8 different flows with varying degree of large scale anisotropy. Circles (\circ) are for $g_{r_2r_2}(z)$ and crosses (\times) are $g_{zz}(r_1)$. The error bars are smaller than the symbols. The values in the color bar are the fluctuations anisotropy measured at the center of the soccer ball for various values of the anisotropy of the forcing.

return to zero asymptotically, but it is not unusual that experimental measurements do not resolve this limit because of the finite size of experiments (e.g. Hwang and Eaton, 2004; de Jong et al., 2009; Siebert et al., 2010). In fact, the first zero crossing would occur outside the region of our flow that is approximately homogeneous. On the other hand, Comte-Bellot and Corrsin (1971) argued that integral scales in finite flows should strictly be zero, if data could be collected that extended far enough. This can be seen by considering the case $k = 0$ in the Wiener-Khinchin relation between the one-dimensional transverse spectrum, $E_{22}(k)$, and its correlation function, $R_{22}(r)$ (see equations 1.27 and 1.28), which yields

$$L_g = \frac{\pi E_{22}(0)}{2 \langle u'^2 \rangle}. \quad (7.18)$$

If we consider, however, the spectrum given by $E_{22}(k) = \tilde{u}(k) \tilde{u}^*(k)$, where the Fourier coefficients of the velocity field averaged over a distance L in physical space are $\tilde{u}(k) = \frac{1}{L} \int_0^L u'(r) e^{-ikr} dr$, given that the mean velocity $\frac{1}{L} \int_0^L u'(r) dr$ is zero, it follows that the coefficient of the zeroth Fourier mode is zero, $\tilde{u}(0) = 0$. It can be immediately seen that $E_{22}(0) = 0$, and thus $L_g = 0$. Only hypothetical infinite flows could have nonzero integral scales. Comte-Bellot and Corrsin (1971) note that the only way to construct a nonzero integral scale from real data is to make ‘simple extrapolations’ of partially measured correlation functions in a reasonable way. We chose to extrapolate the correlation functions with exponential functions (e.g. Van Fossen and Ching, 1994; Van Fossen et al., 1994; de Jong et al., 2009). We are aware that physically plausible extrapolations of the transverse correlation functions must include zero crossing, but Lenschow and Stankov (1986) found that, following the suggestion of Comte-Bellot and Corrsin (1971), approximating the one-dimensional longitudinal spectrum (see equation 1.29) with a downward parabola with zero slope at zero wavenum-

ber gives a correlation function with oscillatory tail. Integrating this correlation function up to its first zero-crossing yields a value that overestimates the integral length by no more than 5%. We found empirically that using more elaborate functions, such as the modified Bessel function, for the extrapolations did not alter our results for the integral length scaling exponent. The difference between the exponents calculated using different fitting functions is less than 10%. We suggest that this is because we only consider ratios of integral scales, not the integral scales themselves, and the influence of the two neglected negative parts of the correlation functions cancel each other. Figure 7.2 shows how a typical extrapolation is done. For each correlation function, we fit an exponential using a least squares algorithm (e.g. Draper and Smith, 1998) to the last 15 data points collected between $0 \leq x \leq x_{\max}$, where the maximum separation, x_{\max} , ranged from 8 mm to 120 mm. We then chose the value of the maximum separation, x_{\max} , that minimized χ^2 , the sum of squares of the vertical differences between the experimental, $g(x_i)$, and the fitted values of the correlation function $\tilde{g}(x_i)$

$$\chi^2 = \sum_{i=1}^N (g(x_i) - \tilde{g}(x_i))^2, \quad (7.19)$$

where N is the total number of samples used in the fit. Figure 7.3 shows the variation of χ^2 with x_{\max} . It can be inferred that $x_{\max} = 13$ mm yields the fit with the smallest sum of squares of residuals. Data for separations $x > x_{\max}$ were extrapolated with exponential tails, whose integral we added to the numerical integration of the data, to yield the integral length. The values of the integral scales did depend on x_{\max} , leading to a variation in the value of the exponent (see figure 7.4). We then used the standard error (see appendix B) of value of the integral scale calculated with different x_{\max} to estimate the error of our integral scale measurement.

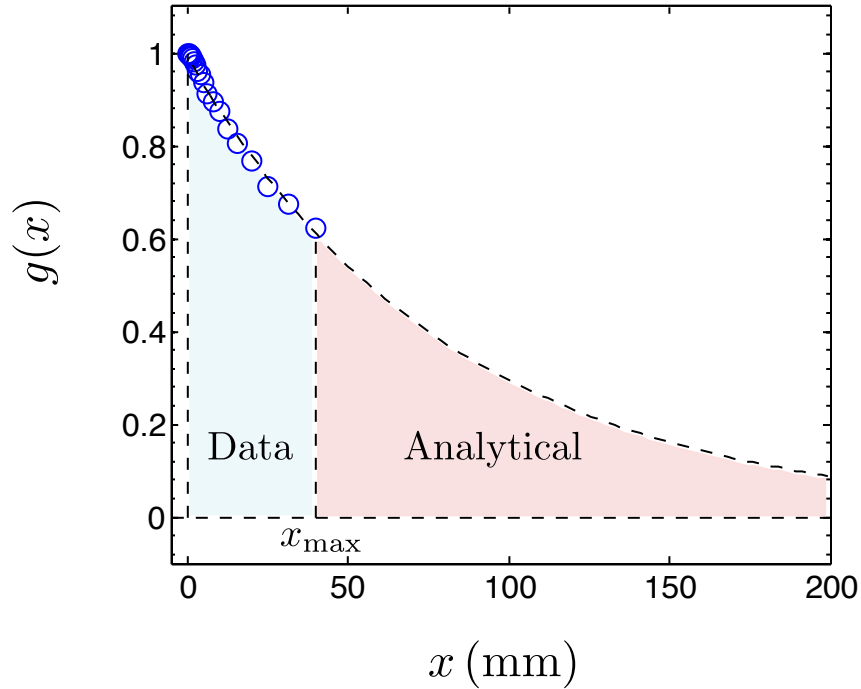


Figure 7.2: The extrapolation of the partially measured correlation function. The blue circular symbols (\circ) are the experimental data. The dashed line is the exponential extrapolated from the data. The area in the region shaded in blue is numerically integrated and the area in the region shaded in pink is analytically calculated. The sum of the two yields the integral length.

We note that, since u'_i is a transverse velocity, the subscript in u'_i indicates the direction of the velocity and the subscript in L_i indicates the direction of the separation over which the integral length is calculated. Therefore, the expected scaling is a power law with a negative exponent

$$\frac{L_z}{L_r} = \left(\frac{u'_z}{u'_r} \right)^{-2/\zeta}, \quad (7.20)$$

in conformity with our definition of axial and radial directions. We test this relationship in figure 7.5. Note that we have used the definition given in equation 4.2 for u'_z/u'_r , in compliance with the definition of u' in 7.17. The integral

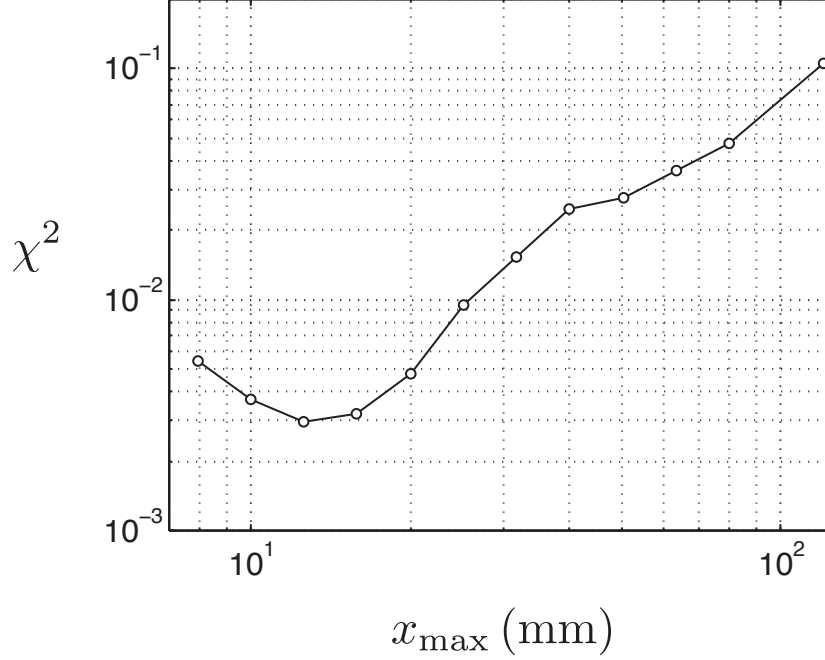


Figure 7.3: The sum of squares of residuals in the determination of x_{\max} that yields the exponential from a least squares fit of an exponential tail to the correlation function data.

length scaling exponent obtained from a least squares straight-line fit

$$\frac{L_z}{L_r} = \left(\frac{u'_z}{u'_r} \right)^\beta, \quad (7.21)$$

to the data is $\beta = -2.56 \pm 0.07$, for which the uncertainty was estimated with the standard error of the slope in the straight-line fit (see appendix B). To check for consistency, we calculated the value for β with the mean value of the inertial range scaling exponents measured using ESS method, ζ_2 (see section 5.2), for which we find $\beta_2 = -2/\zeta_2 = -2.74 \pm 0.06$, assuming that the percentage error remains the same ($\Delta\beta_2/\beta_2 = \Delta\zeta_2/\zeta_2$). The value for β_2 is no more than 7% greater than β . Minor differences between the two scaling exponents may arise from the difference between the exponential and the real correlation curve, which is at present unknown. A function that takes into account the transition

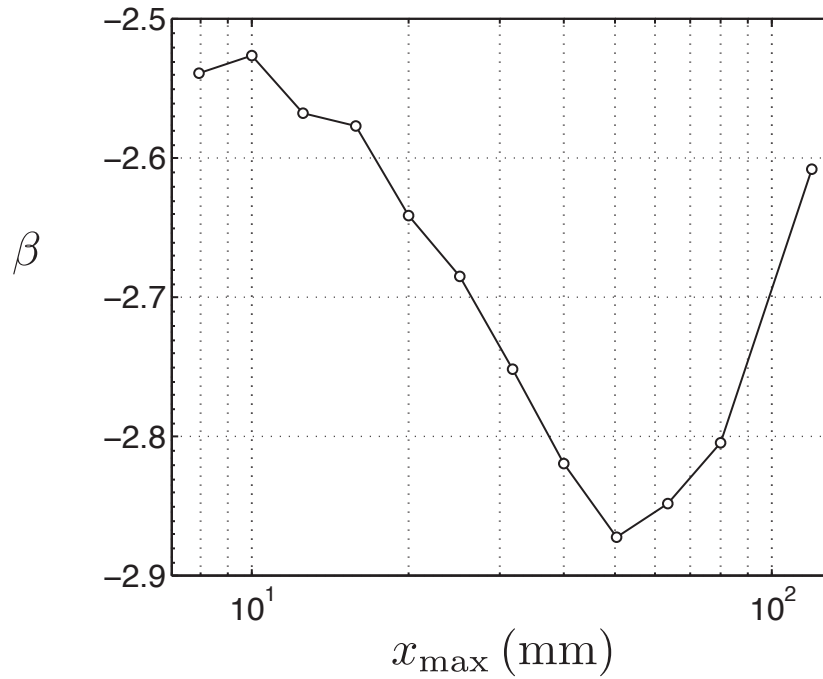


Figure 7.4: The variation in the value of the exponent with the maximum separation in the least squares fit of exponential tails to the data.

range between the inertial scales and the large scales will be able to account for the difference. Nevertheless, even with these simple methods, we find excellent agreement between the two exponents.

In addition, we note that the value of the exponent showed a departure from the Kolmogorov prediction, which has a value of -3 for β if the value of ζ is $2/3$. The difference is very likely due to a Reynolds number effect. We suspect that the difference would become smaller if we increase the Reynolds number.

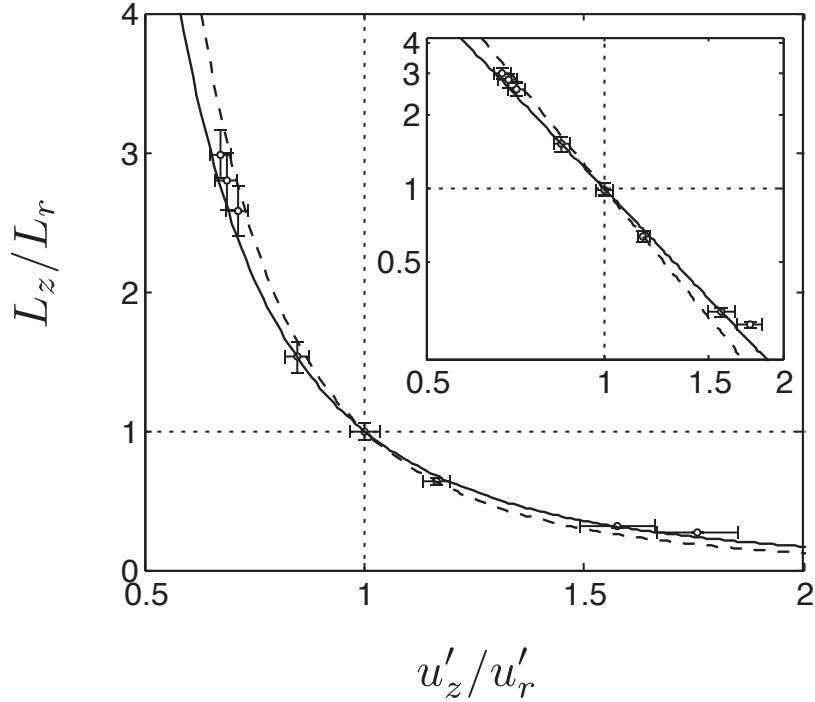


Figure 7.5: The main figure shows the ratio of integral scales, L_z/L_r , as a function of the anisotropy in the fluctuating velocities, u'_z/u'_r . The solid line is the least squares fit to the data and the dashed line is the power law with exponent -3 predicted by the Kolmogorov inertial range scaling argument. The inset shows the same data on a logarithmic scale. The straight line in the inset has a slope of -2.56 .

u'_z/u'_r	L_z (mm)	L_r (mm)	L_z/L_r
0.67 ± 0.03	100 ± 4.3	33.5 ± 0.6	2.99 ± 0.18
0.69 ± 0.03	95.6 ± 4.8	34.2 ± 0.9	2.80 ± 0.21
0.71 ± 0.03	93.0 ± 4.1	36.1 ± 1.0	2.58 ± 0.18
0.84 ± 0.03	76.9 ± 3.3	50.2 ± 1.9	1.53 ± 0.12
1.00 ± 0.04	67.5 ± 2.5	68.0 ± 2.1	0.99 ± 0.07
1.16 ± 0.03	61.0 ± 1.9	95.4 ± 2.6	0.64 ± 0.04
1.58 ± 0.09	45.1 ± 1.0	144 ± 3.9	0.31 ± 0.02
1.76 ± 0.09	42.6 ± 0.5	155 ± 4.5	0.28 ± 0.01

Table 7.1: The numerical data for axial integral lengths (L_z), radial integral lengths (L_r), and the ratio between the two.

7.4 Correlation functions collapse

The test of data collapse is shown in figure 7.6, The value for the inertial range scaling exponent is $\zeta = 0.73$, obtained using the ESS method (see section 5.2). It can be seen that correlation functions stretching out in different directions on the plane in figure 7.1 collapse onto one single curve. Small deviations from the data collapse are visible, especially at large separations, which may be a reflection of the inhomogeneity occurring outside the turbulent boundary, where the effects of individual jets are felt.

7.5 Conclusions

We have presented, in the foregoing pages, a similarity argument applicable to the correlation functions whose main predictions is the power-law scaling of the ratio of integral lengths with the large scale anisotropy ratio, with an exponent governed by the inertial range scaling exponent. Within experimental accuracy, the scaling exponent determined by direct measurement of the ratio of integral lengths and the large scale anisotropy ratio was found to be in excellent agreement with the value derived from the inertial range scaling exponent determined with ESS method. Further, we presented evidence to support the claim that correlation functions can be made to collapse when separations were rescaled with a scaling factor derived from the similarity hypothesis.

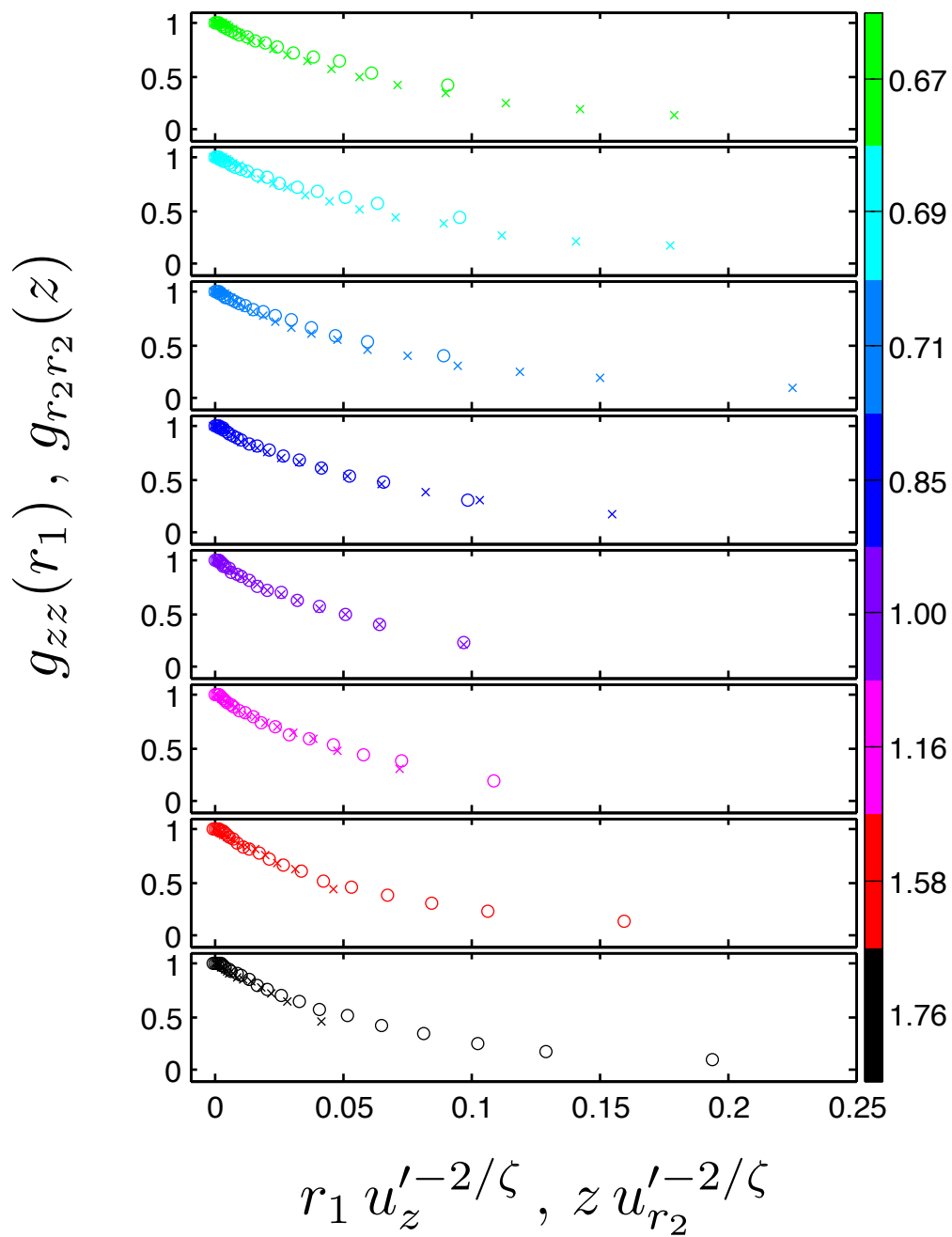


Figure 7.6: The figure shows the same correlation functions from figure 7.1 plotted against the reduced variables, $r_1 u_z'^{-2/\zeta}$ and $z u_{r_2}'^{-2/\zeta}$. Here, $\zeta = 0.73$. Circles (\circ) are for $g_{r_2 r_2}(z)$ and crosses (\times) are for $g_{zz}(r_1)$. The values in the color bar are the fluctuations anisotropy measured at the center of the soccer ball.

CHAPTER 8

SUMMARY AND OUTLOOK

In this dissertation, we have succeeded in isolating the effect of shear from the large scale anisotropy. We saw that anisotropy in the velocity field has difference effects on the inertial and integral scales of turbulence.

In chapter 4 we demonstrated that asymmetry of forcing leads to asymmetry of turbulence in a controllable way. We saw that the flows are approximately homogeneous and axisymmetric, have negligible mean and shear.

In chapter 5, we investigated second-order moments of velocity increments measured in different directions in anisotropic turbulent flows. We ruled out the possibility that the scaling exponent and the Kolmogorov constant might depend on the direction in which the structure function is measured. This is in contrast with previously published results and suggests that the anisotropy produced by shear may be inherently different from that produced only in the fluctuations.

In chapter 6, we examined moments of the velocity increments up to the sixth order. We found evidence that the asymmetry in the probability density of the velocity increments is enhanced when the large scale anisotropy is present. In addition, we found indications that the inertial range scaling exponents are very likely to be independent of anisotropy.

In chapter 7, we presented a scaling argument to describe the anisotropy observed at the large scale. We saw that correlation functions measured in different directions of the flow collapse onto a single curve when appropriately scaled. The scaling implies a power-law relationship between the ratio of in-

tegral lengths and velocity fluctuation anisotropy, whose exponent is closely linked to the inertial range scaling exponent. We found that the exponent measured from the power-law relationship is consistent with the value estimated from the inertial range scaling exponent with extended-self-similarity method. This power-law relationship suggests that self-similarity and Kolmogorov theory are relevant to the large-scale phenomenology of turbulence.

It is important that the reader is aware of some of the difficulties and shortcomings of the scaling argument presented. A point of vagueness is the complete neglect of the dissipation range; correlation function in this range has been shown to follow an analytic scaling law. The second point is the observed anomaly and intermittency in the inertial range scaling exponent. These questions will not be settled by the present measurements, but these measurements will provide more information on which to base a future study.

Further insight into these questions may be provided with tools like the particle image velocimetry (e.g. Raffel et al., 2007) and the Lagrangian particle tracking (e.g. Ouellette, 2006). These measurement systems would allow us to probe the small scales with even higher precision at higher data rate. If further experiments were to be conducted, then we should investigate the angular dependence of the longitudinal structure functions and correlation functions. Do they follow the same scaling law? Or are they intrinsically different from transverse functions, as measurements in shear flows suggest? In addition, we should examine the angular dependence of higher-order structure functions with longer measurement time, derivative structure functions, and the Lagrangian structure functions in our system.

To conclude, let us discuss a fascinating extension of the present work to turbulence in dimensions other than three. A well-founded scientific proof must explore and exhaust all the parameter space in the problem. A parameter we have not been able to vary is the inertial range scaling exponent, ζ_2 , because our system is inherently three-dimensional and it obeys the three-dimensional forced Navier-Stokes equation. Two-dimensional turbulence (e.g. Kraichnan and Montgomery, 1980) has captured the fascination of the researchers because many geophysical and magneto-hydrodynamical phenomena can be formulated as a two-dimensional problem. In the inertial range of two-dimensional turbulence, Kolmogorov-type dimensional reasoning gave r^2 scaling for the second-order velocity structure functions (e.g. Kellay and Goldburg, 2002). The question would then be, does the ratio of integral lengths scale with the fluctuations anisotropy ratio following a power-law with a different inertial range scaling exponent? Measurements in thin layers of conducting fluid (e.g. Xia et al., 2011) and in soap films (e.g. Kellay and Goldburg, 2002) will provide the answer to this question.

We have presented in this thesis a flow apparatus that permits a systematic exploration of turbulence away from isotropy and described some unique features of this system through measurements of structure functions and correlation functions. We believe that understanding the large scale phenomenology of turbulence may elucidate the underlying mechanism of turbulent motions at the small scales. Any useful theory of turbulence must incorporate some degree of anisotropy, and the purpose of our system is to provide a test bed.

APPENDIX A

EVALUATING THE DIMENSIONLESS INTEGRAL A_γ

The integral

$$A_\gamma = \int_{-\infty}^{\infty} (1 - e^{ix})|x|^{-(\gamma+1)} dx \quad , \quad (0 < \gamma < 2), \quad (\text{A.1})$$

may be written as a sum of two integrals

$$A_\gamma = \int_{-\infty}^0 (1 - e^{ix})|x|^{-(\gamma+1)} dx + \int_0^{\infty} (1 - e^{ix})|x|^{-(\gamma+1)} dx. \quad (\text{A.2})$$

By making a substitution of variables $y = -x$ in the first integral and employing the trigonometric identity $\cos(x) = \frac{1}{2}(e^{ix} + e^{-ix})$, we can combine the two integrals to obtain

$$A_\gamma = 2 \int_0^{\infty} (1 - \cos(x)) x^{-(\gamma+1)} dx, \quad (\text{A.3})$$

Integrating the above integral by parts, the resulting boundary term can be shown to vanish at the boundary and we are left with

$$A_\gamma = \frac{2}{\gamma} \int_0^{\infty} x^{-\gamma} \sin(x) dx. \quad (\text{A.4})$$

This integral can be evaluated by considering a complex integral of the form

$$\mathfrak{A} = \oint z^{-\gamma} e^{iz} dz, \quad (\text{A.5})$$

and by applying Cauchy's theorem to the closed curve consisting of two line segments along positive $\text{Re } z$ and $\text{Im } z$ axes and two quadrants in the upper half plane; one very large with radius R and one very small with radius δ , as shown in figure A.1. The point $z = 0$ has to be avoided; we do this by following the small circular quadrant of radius δ . The integral over the big circular quadrant C_2 tends to 0 as $R \rightarrow \infty$. The integral over the small circular quadrant near the

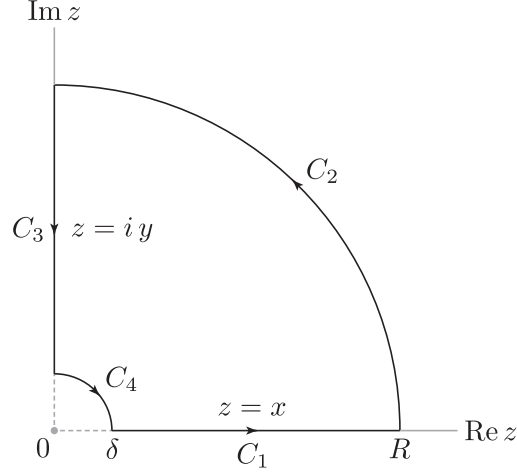


Figure A.1: Contour for the integral A.5. The pole at zero has been avoided by following the small circular quadrant near the origin. The integrals over the two circular quadrants tend to zero as $R \rightarrow \infty$ and $\delta \rightarrow 0$. Only the integrals over the line segments contribute to the integral A.5.

origin C_4 can also be seen to approach 0 as $\delta \rightarrow 0$. Only the integrals over the line segments remain and the complex integral reduces to

$$\mathfrak{A} = \int_0^\infty x^{-\gamma} e^{ix} dx - e^{i(1-\gamma)\pi/2} \int_0^\infty y^{-\gamma} e^{-y} dy. \quad (\text{A.6})$$

Because we have avoided the pole at the origin, the integral \mathfrak{A} equals 0 by Cauchy's theorem. After a substitution of $\Gamma(1 - \gamma) = \int_0^\infty y^{-\gamma} e^{-y} dy$, the imaginary part of \mathfrak{A} yields

$$\int_0^\infty x^{-\gamma} \sin(x) dx = \Gamma(1 - \gamma) \cos\left(\frac{\gamma\pi}{2}\right). \quad (\text{A.7})$$

From Euler's reflection formula, $\Gamma(1 - \gamma)\Gamma(\gamma) = \pi/\sin(\gamma\pi)$, and the double-angle formula, $\sin(2\theta) = 2 \sin \theta \cos \theta$, the above integral can be written in the form

$$\int_0^\infty x^{-\gamma} \sin(x) dx = \frac{\pi}{2\Gamma(\gamma) \sin(\gamma\pi/2)}. \quad (\text{A.8})$$

Finally, with a substitution of the above in equation A.4 and an explicit use of the recurrence relation $\Gamma(\gamma + 1) = \gamma \Gamma(\gamma)$, we find

$$A_\gamma = \frac{\pi}{\Gamma(\gamma + 1) \sin(\gamma \pi/2)}. \quad (\text{A.9})$$

Gradshteyn and Ryzhik (2007) (3.761, equation 4) give

$$\int_0^\infty x^{\mu-1} \sin(ax) dx = \frac{\Gamma(\mu)}{a^\mu} \sin\left(\frac{\mu \pi}{2}\right) \quad [a > 0; \quad 0 < |\text{Re } \mu| < 1]. \quad (\text{A.10})$$

The integral in equation A.4 is a special case of that found in Gradshteyn and Ryzhik (2007) with $a = 1$ and $\mu = 1 - \gamma$.

APPENDIX B
STATISTICAL TOOLS

In this thesis, unless otherwise stated, the following statistical estimators are used. For a sample (data set) with sample size N and observed values x_1, x_2, \dots, x_N , the sample mean, $\langle x \rangle$, is the sum of the observations divided by the sample size

$$\langle x \rangle = \frac{1}{N} \sum_{i=1}^N x_i. \quad (\text{B.1})$$

The measure of spread, or variability, in the sample is the sample standard deviation

$$\sigma_x = \left[\frac{1}{N-1} \sum_{i=1}^N (x_i - \langle x \rangle)^2 \right]^{1/2}. \quad (\text{B.2})$$

The measure of spread, or variability, in the sample mean is the standard error (the central limit theorem)

$$\text{SE} = \frac{\sigma_x}{\sqrt{N}}. \quad (\text{B.3})$$

For a sample with N pairs of independent (x_i) and dependent variables (y_i), if a straight line, $\tilde{y}_i = a + b x_i$, is appropriate for the range of values studied, the linear regression coefficients, a and b , are those for which the sum of squared residuals, $\sum_i^N (y_i - \tilde{y}_i)^2$, is minimized. Defining the following sums of squares

$$S_{xx} = \sum_{i=1}^N (x_i - \langle x \rangle)^2, \quad (\text{B.4})$$

$$S_{yy} = \sum_{i=1}^N (y_i - \langle y \rangle)^2, \quad (\text{B.5})$$

$$S_{xy} = \sum_{i=1}^N (x_i - \langle x \rangle)(y_i - \langle y \rangle), \quad (\text{B.6})$$

the slope, b , and intercept, a , are given by

$$b = \frac{S_{xy}}{S_{xx}}, \quad (\text{B.7})$$

$$a = \langle y \rangle - b \langle x \rangle. \quad (\text{B.8})$$

Let $\tilde{y}_i = a + b x_i$ be the value predicted by the least-squares fit, then the difference between the original value and the predicted value is given by $\xi_i = y_i - \tilde{y}_i$. The measure for the spread in ξ_i is the sum of squares of residuals

$$s_\xi = \left[\frac{1}{N-2} \sum_{i=1}^N \xi_i^2 \right]^{1/2}, \quad (\text{B.9})$$

or it can be rewritten in terms of the sums of squares

$$s_\xi = \left[\frac{S_{xx} S_{yy} - S_{xy}^2}{(N-2) S_{xx}} \right]^{1/2}. \quad (\text{B.10})$$

The standard errors for the intercept, a , and the slope, b , are

$$\text{SE}(a) = s_\xi \left[\frac{1}{N} + \frac{\langle x \rangle^2}{S_{xx}} \right]^{1/2}, \quad (\text{B.11})$$

$$\text{SE}(b) = \frac{s_\xi}{\sqrt{S_{xx}}}. \quad (\text{B.12})$$

For a reference on linear regression, see e.g. Acton (1966).

APPENDIX C

GENERATING EXPONENTIALLY CORRELATED COLORED NOISE

```
1 %%%%%%%%%%%%%%%%%%%%%%%%%%%%%%%%%%%%%%%%%%%%%%%%%%%%%%%%%%%%%%%%%%%%%%%%%%
2 % This Matlab script calculates the exponentially %
3 % correlated colored noise using the algorithm by %
4 % Fox et al. (PRA, 38, 5938-5940, 1988). %
5 %%%%%%%%%%%%%%%%%%%%%%%%%%%%%%%%%%%%%%%%%%%%%%%%%%%%%%%%%%%%%%%%%%%%%%%%%%
6
7 % Setting parameters for the algorithm
8 a = 0; % Initializing random number
9 b = 0; % Initializing random number
10 lambda = 1./(0.1); % 1/Correlation time (1/seconds)
11 D = 1./lambda; % Correlation time (seconds), D*lambda = 1
12 N = 2.^17; % Number of samples
13 f = 50; % Carrier frequency (Hz)
14 Fs = 3000; % Sampling frequency
15 dt = 1./Fs; % Sample time
16 t = dt.*[0:1:(N-1)]'; % Time array
17 E = exp(-lambda.*dt);
18
19 % Here begins the algorithm
20 e = zeros(N,1); % Initializing noise array
21 for i=1:(N-1)
22     a = rand(1);
23     b = rand(1);
24     h = sqrt(-2.*D.*lambda.*(1-E.^2).*log(a)).*cos(2.*pi.*b);
25     e(i+1) = e(i).*E + h;
26 end
27
```

```

28 % Modulate the amplitude of the carrier wave
29 amp = e.*sin(2.*pi.*f.*t);
30
31 % Display the signal
32 figure;
33 plot(t, amp, 'k-');
34 xlabel('Time (s)');
35 ylabel('Voltage (V)');
36
37 % Take the Fourier transform of the signal
38 Nfft = 2^nextpow2(N);
39 famp = fft(amp,Nfft)/N;
40 freq = (Fs./2).*linspace(0,1,Nfft/2+1);
41 y     = abs(famp(1:Nfft/2+1)).^2;
42
43 % Display the spectrum
44 figure;
45 loglog(freq, y, 'ko');
46 xlabel('Frequency (Hz)');
47 ylabel('|Amplitude|^2 (A.U.)');
48
49 % Get rid of noise in the spectrum
50 windowsize = 30;
51 yf = filter(ones(1,windowsize)/windowsize,1,y);
52
53 % Display the filtered spectrum
54 figure;
55 loglog(freq, yf, 'ko');
56 xlabel('Frequency (Hz)');
57 ylabel('|Amplitude|^2 (A.U.)');

```

APPENDIX D

CALCULATING STATISTICS WITH INTER-ARRIVAL TIME WEIGHTING

```
1 %%%%%%%%%%%%%%%%%%%%%%%%%%%%%%%%%%%%%%%%%%%%%%%%%%%%%%%%%%%%%%%%%%%%%%%%%%
2 % This Matlab function calculates statistics                               %
3 % according to inter-arrival time weighting                             %
4 %                                                                       %
5 % [out, sigma, num] = InterArrival(t, v);                               %
6 %                                                                       %
7 % Each vector is weighted by the time past since previous            %
8 % measurement.                                                         %
9 % Measurements made after 5 times of the mean arrival time            %
10 % are rejected.                                                        %
11 %%%%%%%%%%%%%%%%%%%%%%%%%%%%%%%%%%%%%%%%%%%%%%%%%%%%%%%%%%%%%%%%%%%%%%%%%%
12
13 function [out, varargout] = InterArrival(t, v)
14
15 % Check for error in input arguments
16 error(nargchk(1,2,nargin));
17 if (nargin < 2) || isempty(v)
18     error('Input argument must contain two vectors');
19 end
20
21 if length(t) ≠ length(v)
22     error('Vectors must have the same length');
23 end
24
25 % Specify the criterion for rejection
26 limit = 5;
27
```

```

28 % Calculate the inter-arrival time
29 dt    = diff(t);
30 v     = v(2:length(v));
31
32 % Reject measurements with dt > 5*mean(dt)
33 accept = logical(dt < limit*mean(dt, 1));
34
35 dt = dt(accept);
36 v  = v(accept);
37
38 % Calculate the weighted sum
39 out = sum(v.*dt) / sum(dt);
40
41 % Provide the standard deviation and the number of statistics
42 if (nargout > 1)
43     varargout(1) = {std(v)};
44 end
45 if (nargout == 3)
46     varargout(2) = {length(v)};
47 end

```

APPENDIX E
RESAMPLING LDV VELOCITY SIGNALS

```
1 %%%%%%%%%%%%%%%%%%%%%%%%%%%%%%%%%%%%%%%%%%%%%%%%%%%%%%%%%%%%%%%%%%%%%%%%%%
2 %   This Matlab function resamples LDV velocity signal           %
3 %   tin will be rounded up to the nearest multiples             %
4 %   of tsep.                                                    %
5 %   If there are more than one velocity within a particular    %
6 %   tin, an average of the velocities is calculated.          %
7 %                                                                 %
8 %   syntax:                                                     %
9 %       [vout, tout, nout] = LDVResample(vin, tin, tsep);      %
10 %   inputs:                                                     %
11 %       vin  -- velocity vector                                 %
12 %       tin  -- time vector                                    %
13 %       tsep -- separation time                                %
14 %   outputs:                                                    %
15 %       vout -- resampled velocity vector                     %
16 %       tout -- resampled time vector in multiples of tsep    %
17 %       nout -- number of elements within a bin               %
18 %%%%%%%%%%%%%%%%%%%%%%%%%%%%%%%%%%%%%%%%%%%%%%%%%%%%%%%%%%%%%%%%%%%%%%%%%%
19
20 function [vout, tout, nout] = LDVResample(vin, tin, tsep)
21
22 % Check for error in input arguments
23 error(nargchk(1,3,nargin));
24 if nargin < 2 || isempty(tin)
25     error('Time array is missing!');
26 end
27
```

```

28 if nargin < 3 || isempty(tsep)
29     error('Specify separation time.');
```

30 end

31

```

32 if ischar(vin) || ischar(tin) || ischar(tsep)
33     error('Input arguments must be numeric.');
```

34 end

35

```

36 % Initialize vectors
37 vout = zeros(1+round(max(tin)/tsep), 1);
38 nout = vout;
```

39

```

40 % Take the sum of velocities within a bin
41 for i = 1:length(tin)
42     j      = 1 + round(tin(i)/tsep);
43     vout(j) = vout(j) + vin(i);
44     nout(j) = nout(j) + 1;
```

45 end

46

```

47 % Calculate average
48 nout = nout + (nout==0);
49 vout = vout ./ nout;
```

50 tout = tsep*[0:round(max(tin)/tsep)]';

APPENDIX F

CALCULATING VELOCITY AUTOCORRELATION

```

1 %%%%%%%%%%%%%%%%%%%%%%%%%%%%%%%%%%%%%%%%%%%%%%%%%%%%%%%%%%%%%%%%%%%%%%%%%
2 % This Matlab function calculates velocity correlation           %
3 % for equally spaced data                                     %
4 %                                                             %
5 %   syntax:                                                  %
6 %       [fout, stat] = LDVCorr(v1, v2, t1, t2);              %
7 %   inputs:                                                  %
8 %       v1, v2  -- velocity vectors                          %
9 %       t1, t2  -- time vectors, equally spaced              %
10 %   outputs:                                                 %
11 %       fout    -- velocity correlation function              %
12 %       stat    -- [v1_RMS, v2_RMS, v1_mean, v2_mean,        %
13 %                  nfout, nv1_mean, nv2_mean]                %
14 %       RMS     -- RMS of coincident velocities              %
15 %       mean    -- mean of nonzero velocities.               %
16 %       n's     -- number of statistics                       %
17 %%%%%%%%%%%%%%%%%%%%%%%%%%%%%%%%%%%%%%%%%%%%%%%%%%%%%%%%%%%%%%%%%%%%%%%%%
18
19 function [fout, varargout] = LDVCorr(v1, v2, t1, t2)
20
21 % Check for error in input arguments
22 error(nargchk(1,4,nargin));
23 if nargin < 2 || isempty(v2)
24     error('v2 is missing!');
25 end
26 if nargin < 3 || isempty(t1)
27     error('t1 for v1 is missing!');

```

```

28 end
29 if nargin < 4 || isempty(t2)
30     error('t2 for v2 is missing!');
31 end
32
33 % Locate nonzero elements
34 cutoff = min([length(t1) length(t2)]);
35 nonzero = find(v1(1:cutoff).*v2(1:cutoff));
36
37 % Calculate the correlation
38 foo = (v1(nonzero)-mean(v1(find(v1)))).*(v2(nonzero)-mean(v2(find(v2)))) / ...
39     (std(v1(nonzero)-mean(v1(find(v1))))*std(v2(nonzero)-mean(v2(find(v2)))));
40 fout = sum(foo)/length(nonzero);
41
42 % Provide the RMS, the mean and the number of statistics
43 if (nargout > 1)
44     stat    = zeros(1,7);
45     RMS1    = std(v1(nonzero)-mean(v1(find(v1)))));
46     RMS2    = std(v2(nonzero)-mean(v2(find(v2)))));
47     MEAN1   = mean(v1(find(v1)));
48     MEAN2   = mean(v2(find(v2)));
49     NFOUT   = length(nonzero);
50     NMEAN1  = length(find(v1));
51     NMEAN2  = length(find(v2));
52     stat(:) = [RMS1 RMS2 MEAN1 MEAN2 NFOUT NMEAN1 NMEAN2];
53     varargout(1) = {stat};
54 end

```

APPENDIX G

CALCULATING LEAST-SQUARES FIT COEFFICIENTS

For an introduction to the theory of linear regression, the reader could consult Draper and Smith (1998).

```

1 %%%%%%%%%%%%%%%%%%%%%%%%%%%%%%%%%%%%%%%%%%%%%%%%%%%%%%%%%%%%%%%%%%%%%%%%%
2 % This Matlab function calculates the least square fit coefficients
3 % square fit coefficients
4 % Usage:
5 % [B] = LinearMultiVarFit(Y, X1, X2, ..., XN, flag);
6 % Input:
7 % Y - fit function
8 % X1, X2, ... XN - variables (2D arrays)
9 % flag - 'zero' for regression through the origin.
10 % default is no crossing at origin.
11 % Output:
12 % B - an array of fit coefficients
13 %
14 % LinearMultiVarFit calculates the fit coefficients of
15 % the multivariate function
16 %  $Y = B_0 + B_1 \cdot X_1 + B_2 \cdot X_2 + \dots + B_N \cdot X_N$ 
17 % with matrix left division in the least square sense.
18 % If X's and Y are M by N matrices, B(:,j) is a
19 % column vector [B0 B1 B2 ... BN] of fit coefficients
20 % for each set of Y(:,j), X1(:,j), X2(:,j), ... XN(:,j)
21 %%%%%%%%%%%%%%%%%%%%%%%%%%%%%%%%%%%%%%%%%%%%%%%%%%%%%%%%%%%%%%%%%%%%%%%%%
22
23 function B = LinearMultiVarFit(varargin)
24

```

```

25 % Check for error in input argument
26 if (nargin < 2)
27     error('Input argument must contain at least two arrays');
28 end
29
30 % Check for the number of input arrays
31 if isstr(varargin{end})
32     nin      = nargin-1;
33     zeroflag = varargin{end};
34 else
35     nin      = nargin;
36     zeroflag = 'boobs';
37 end
38
39 % Form an ND array
40 for i=1:nin
41     X(:, :, i) = varargin{i};
42 end
43
44 [M, N, P] = size(X);
45
46 % Initialize array
47 if (M==1)
48     X = permute(X, [2 1 3]);
49     [NX, NY, NZ] = size(X);
50     B = zeros(NZ,1);
51 else
52     if (N==1)
53         [NX, NY, NZ] = size(X);
54         B = zeros(NZ,1);
55     else
56         [NX, NY, NZ] = size(X);

```

```

57         B = zeros (NZ,NY);
58     end
59 end
60
61 % Compute fit coefficients
62 if (strcmpi(zeroflag,'zero'))
63     B(1,:) = 0;
64     Mat = zeros(NX,NZ-1);
65     for i=1:NY
66         Mat(:,i) = X(:,i,2:end);
67         out      = Mat\X(:,i,1);
68         B(2:end,i) = out;
69         clear out
70     end
71 else
72     Mat = zeros(NX,NZ);
73     Mat(:,1) = ones(NX,1);
74     for i=1:NY
75         Mat(:,2:end) = X(:,i,2:end);
76         out          = Mat\X(:,i,1);
77         B(:,i)      = out;
78         clear out
79     end
80 end

```

BIBLIOGRAPHY

- F. S. Acton. *Analysis of Straight-Line Data*. Dover, New York, 1966.
- R. J. Adrian and C. S. Yao. Power spectra of fluid velocities measured by laser doppler velocimetry. *Experiments in Fluids*, 5:17–28, 1987.
- H.-E. Albrecht, M. Borys, N. Damaschke, and C. Tropea. *Laser Doppler and phase Doppler measurement techniques*. Springer-Verlag, Berlin Heidelberg New York, 2003.
- D. Anfossi, G. Degrazia, E. Ferrero, S. E. Gryning, M. G. Morselli, and S. T. Castelli. Estimation of the Lagrangian structure function constant C_0 from surface-layer wind data. *Boundary-Layer Meteorology*, 95:249–270, 2000.
- F. Anselmet, Y. Gagne, E. J. Hopfinger, and R. A. Antonia. High-order velocity structure functions in turbulent shear flows. *Journal of Fluid Mechanics*, 140: 63–89, 1984.
- R. A. Antonia and B. R. Pearson. Low-order velocity structure functions in relatively high Reynolds number turbulence. *Europhysics Letters*, 48(2):163–169, 1999.
- R. A. Antonia, T. Zhou, and G. P. Romano. Small-scale turbulence characteristics of two-dimensional bluff body wakes. *Journal of Fluid Mechanics*, 459:67–92, 2002.
- I. Arad, B. Dhruva, S. Kurien, V. S. L’vov, I. Procaccia, and K. R. Sreenivasan. The extraction of anisotropic contributions in turbulent flows. *Physical Review Letters*, 81(24):5330–5333, 1998.

- I. Arad, L. Biferale, I. Mzzitelli, and I. Procaccia. Disentangling scaling properties in anisotropic and inhomogeneous turbulence. *Physical Review Letters*, 82 (25):5040–5043, 1999.
- G. I. Barenblatt and N. Goldenfeld. Does fully developed turbulence exist? Reynolds number independence versus asymptotic covariance. *Physics of Fluids*, 7:3078–3082, 1995.
- M. J. Barrett and D. K. Hollingsworth. On the calculation of length scales for turbulent heat transfer correlation. *Journal of Heat Transfer*, 123:878–883, 2001.
- G. K. Batchelor. The Theory of Axisymmetric Turbulence. *Proc. R. Soc. Lond. A*, 186(1007):480–502, 1946a.
- G. K. Batchelor. Double velocity correlation function in turbulent motion. *Nature*, 158:883–884, 1946b.
- G. K. Batchelor. Kolmogoroff’s theory of locally isotropic turbulence. *Proc. Camb. Phil. Soc.*, 43:533–559, 1947.
- G. K. Batchelor. Decay of isotropic turbulence in the initial period. *Proc. R. Soc. Lond. A*, 193:539–558, 1948.
- G. K. Batchelor. Pressure fluctuations in isotropic turbulence. *Mathematical Proceedings of the Cambridge Philosophical Society*, 47:359–374, 1951.
- G. K. Batchelor. Diffusion in a field of homogeneous turbulence. ii. The relative motion of particles. *Proc. Camb. Phil. Soc.*, 48:345–362, 1952.
- G. K. Batchelor. *The theory of homogeneous turbulence*. Cambridge University Press, Cambridge, U. K., 1956.

- G. K. Batchelor and A. A. Townsend. Decay of turbulence in the final period. *Proc. R. Soc. Lond. A*, 194(1039):527–543, 1948.
- R. Benzi, S. Ciliberto, R. Tripicciono, C. Baudet, F. Massaioli, and S. Succi. Extended self-similarity in turbulent flows. *Physical Review E*, 48:R29–R32, 1993.
- R. Benzi, L. Biferale, S. Ciliberto, M. V. Struglia, and R. Tripicciono. Generalized scaling in fully developed turbulence. *Physica D*, 96:162–181, 1996.
- A. Bershadskii. Near-dissipation range in nonlocal turbulence. *Physics of Fluids*, 20(8):085103, 2008.
- G. P. Bewley, K. R. Sreenivasan, and D. P. Lathrop. Particles for tracing turbulent liquid helium. *Experiments in Fluids*, 44:887–896, 2008.
- L. Biferale and I. Procaccia. Anisotropy in turbulent flows and in turbulent transport. *Physics Reports*, 414:43–164, 2005.
- L. Biferale and F. Toschi. Anisotropic homogeneous turbulence: hierarchy and intermittency of scaling exponents in the anisotropic sectors. *Physical Review Letters*, 86(21):4831–4834, 2001.
- O. N. Boratav and R. B. Pelz. Structures and structure functions in the inertial range of turbulence. *Physics of Fluids*, 9:1400–1415, 1997.
- M. S. Borgas and B. L. Sawford. The small-scale structure of acceleration correlations and its role in the statistical theory of turbulent dispersion. *Journal of Fluid Mechanics*, 228:69–99, 1991.
- P. Buchhave. Biasing errors in individual particle measurements. In *Proc. LDA Symp. Copenhagen*, pages 258–278, Tonsbakken 16-18, 2740 Skovlunde, Denmark, 1975.

- P. Buchhave, W. K. Jr. George, and J. L. Lumley. The measurement of turbulence with the laser-dopper anemometer. *Annu. Rev. Fluid Mech.*, 11:443–504, 1979.
- R. Camussi and R. Benzi. Hierarchy of transverse structure functions. *Physics of Fluids*, 9:257–259, 1997.
- R. Camussi, D. Barbagallo, G. Guj, and F. Stella. Transverse and longitudinal scaling laws in non-homogeneous low Re turbulence. *Physics of Fluids*, 8:1181–1191, 1996.
- J. S. Carullo, S. Nasir, R. D. Cress, W. F. Ng, K. A. Thole, L. J. Zhang, and H. K. Moon. The effects of freestream turbulence, turbulence length scale, and exit Reynolds number on turbine blade heat transfer in a transonic cascade. *Journal of Turbomachinery*, 133(011030):1–11, 2011.
- S. Chakraborty, U. Frisch, and S. S. Ray. Extended self-similarity works for the Burgers equation and why. *Journal of Fluid Mechanics*, 649:275–285, 2010.
- S. Chandrasekhar. The Theory of Axisymmetric Turbulence. *Phil. Trans. R. Soc. Lond. A*, 242:557–577, 1950.
- S. Chen, K. R. Sreenivasan, M. Nelkin, and N. Cao. A refined similarity hypothesis for transverse structure functions. *Physical Review Letters*, 79:2253–2256, 1997.
- G. Comte-Bellot and S. Corrsin. The use of a contraction to improve the isotropy of grid-generated turbulence. *Journal of Fluid Mechanics*, 25:657–682, 1966.
- G. Comte-Bellot and S. Corrsin. Simple Eulerian time correlation of full- and narrow-band velocity signals in grid-generated, ‘isotropic’ turbulence. *Journal of Fluid Mechanics*, 48 part 2:273–337, 1971.

- S. Corrsin. On the spectrum of isotropic temperature fluctuations in isotropic turbulence. *J. Appl. Phys.*, 22:469–473, 1951.
- S. Corrsin. Estimates of the relations between Eulerian and Lagrangian scales in large Reynolds number turbulence. *Journal of the Atmospheric Sciences*, 20: 115–119, 1963a.
- S. Corrsin. *Turbulence: Experimental Methods*, in *Handbuch der Physik*, volume VIII/2, chapter 4, pages 524–590. Springer-Verlag, 1963b.
- S. Corrsin and J. L. Lumley. On the equation of motion for a particle in turbulent fluid. *Applied Scientific Research*, 6A:114–116, 1956.
- J. Counihan. Adiabatic atmospheric boundary layers: a review and analysis of data from the period 1880-1972. *Atmos. Environ.*, 19:871–905, 1975.
- H. E. Cramer. Measurements of turbulence structure near the ground within the frequency range from 0.5 to 0.01 cycles sec^{-1} . *Adv. Geophys.*, 6:75–96, 1959.
- J. de Jong, L. Cao, S. H. Woodward, J. P. L. C. Salazar, L. R. Collins, and H. Meng. Dissipation rate estimation from PIV in zero-mean isotropic turbulence. *Experiments in Fluids*, 46:499–515, 2009.
- G. A. Degrazia, G. S. Welter, A. R. Wittwer, J. C. Carvalho, D. R. Roberti, O. C. Acevedo, O. L. L. Moraes, and H. F. C. Velho. Estimation of the Lagrangian Kolmogorov constant from Eulerian measurements for distinct Reynolds number with application to pollution dispersion model. *Atmospheric Environment*, 42:2415–2423, 2008.
- J. del Álamo and J. Jiménez. Estimation of turbulent convection velocities and corrections to Taylor’s approximation. *Journal of Fluid Mechanics*, 640:5–26, 2009.

- B. Dhruva, Y. Tsuji, and K. R. Sreenivasan. Transverse structure functions in high-Reynolds-number turbulence. *Physical Review E*, 56(5):R4928–R4930, 1997.
- W. Dobler, N. E. L. Haugen, T. A. Yousef, and A. Brandenburg. Bottleneck effect in three-dimensional turbulence simulations. *Physical Review E*, 68(2):026304, 2003.
- D. A. Donzis and K. R. Sreenivasan. The bottleneck effect and the Kolmogorov constant in isotropic turbulence. *Journal of Fluid Mechanics*, 657:171–188, 2010.
- N. R. Draper and H. Smith. *Applied regression analysis*. Wiley-Interscience, New York, 1998.
- H. L. Dryden, G. B. Schubauer, W. C. Mock, and H. K. Skramstad. Measurements of intensity and scale of wind tunnel turbulence and their relation to the critical Reynolds number of spheres. Technical Report 581, Nat. Adv. Com. Aeronaut., 1937.
- N. Ducet, P. Y. Le-Traon, and G. Reverdin. Global high-resolution mapping of ocean circulation from TOPEX/Poseidon and ERS-1 and -2. *Journal of Geophysical Research*, 105(C8):19477–19498, 2000.
- S. Elghobashi. On predicting particle-laden turbulent flows. *Applied Scientific Research*, 52:309–329, 1994.
- S. Elghobashi and G. C. Truesdell. On the two-way interaction between homogeneous turbulence and dispersed solid particles. I: Turbulence modification. *Physics of Fluids A*, 5(7):1790–1801, 1993.
- D. Ewing, B. Frohnepfel, W. K. George, J. M. Pedersen, and J. Westerweel. Two-point similarity in the round jet. *Journal of Fluid Mechanics*, 577:309–330, 2007.

- G. Eyink. Personal communication, 15 March 2011.
- G. L. Eyink and J. Xin. Self-similar decay in the Kraichnan model of a passive scalar. *Journal of Statistical Physics*, 100(3/4):679–741, 2000.
- A. L. Fairhall, O. Gat, V. L'vov, and I. Procaccia. Anomalous scaling in a model of passive scalar advection: Exact results. *Physical Review E*, 53(4):3518–3535, 1996.
- G. Falkovich. Bottleneck phenomenon in developed turbulence. *Physics of Fluids*, 6:1411–1414, 1994.
- G. Falkovich and V. S. L'vov. Isotropic and anisotropic turbulence in Clebsch variables. *Chaos, Solitons & Fractals*, 5:1855–1869, 1995.
- R. P. Feynman, R. B. Leighton, and M. Sands. *The Feynman Lectures on Physics*, volume 1. Addison-Wesley, Reading MA, 1963.
- J. Finnigan. Turbulence in plant canopies. *Annu. Rev. Fluid Mech.*, 32:519–571, 2000.
- R. F. Fox, I. R. Gatland, R. Roy, and G. Vemuri. Fast, accurate algorithm for numerical simulation of exponentially correlated colored noise. *Physical Review A*, 38(11):5938–5940, 1988.
- D. Fransos and L. Bruno. Edge degree-of-sharpness and free-stream turbulence scale effects on the aerodynamics of a bridge deck. *Journal of Wind Engineering and Industrial Aerodynamics*, 98:661–671, 2010.
- P. Franzese and M. Cassiani. A statistical theory of turbulent relative dispersion. *Journal of Fluid Mechanics*, 571:391–417, 2007.

- C. A. Friehe, W. J. Shaw, D. P. Rogers, K. L. Davidson, W. G. Large, S. A. Stage, G. H. Crescenti, S. J. S. Khalsa, G. K. Greenhut, and F. Li. Air-sea fluxes and surface layer turbulence around a sea surface temperature front. *Journal of Geophysical Research*, 96(C5):8593–8609, 1991.
- U. Frisch. *Turbulence: The Legacy of A. N. Kolmogorov*. Cambridge University Press, Cambridge, U. K., 1995.
- U. Frisch, S. Kurien, R. Pandit, W. Pauls, S. S. Ray, A. Wirth, and J. Zhu. Hyperviscosity, Galerkin truncation, and bottlenecks in turbulence. *Physical Review Letters*, 101(14):144501, 2008.
- S. Garg and Z. Warhaft. On the small scale structure of simple shear flow. *Physics of Fluids*, 10(3):662–673, 1998.
- G. Gioia and F. A. Bombardelli. Scaling and similarity in rough channel flows. *Physical Review Letters*, 88(014501), 2001.
- G. Gioia and F. A. Bombardelli. Localized turbulent flows on scouring granular beds. *Physical Review Letters*, 95(014501), 2005.
- G. Gioia and P. Chakraborty. Turbulent friction in rough pipes and the energy spectrum of the phenomenological theory. *Physical Review Letters*, 96(044502), 2006.
- G. Gioia, N. Guttenberg, N. Goldenfeld, and P. Chakraborty. Spectral theory of the turbulent mean-velocity profile. *Physical Review Letters*, 105(184501), 2010.
- E. Gledzer, E. Villermaux, H. Kahalerras, and Y. Gagne. On the log-Poisson statistics of the energy dissipation field and related problems of developed turbulence. *Physics of Fluids*, 8(12):3367–3378, 1996.

- A. Glezer and M. Amitay. Synthetic jets. *Annu. Rev. Fluid Mech.*, 34:503–529, 2002.
- K. Gödecke. Messungen der atmosphärischen Turbulenz in Bodennähe mit einer Hitzdrahtmethode. *Ann. Hydrogr.*, – (10):400–410, 1935.
- C. Goepfert, J.-L. Marié, D. Chareyron, and M. Lance. Characterization fo a system generating a homogeneous isotropic turbulence field by free synthetic jets. *Experiments in Fluids*, 48:809–822, 2010.
- N. Goldenfeld. Roughness-induced critical phenomena in a turbulent flow. *Physical Review Letters*, 96(044503), 2006.
- G. Gotoh, D. Fukayama, and T. Nakano. Velocity field statistics in homogeneous steady turbulence obtained using a high-resolution direct numerical simulation. *Physics of Fluids*, 14(3):1065–1081, 2002.
- I. S. Gradshteyn and I. M. Ryzhik. *Table of integrals, series, and products*. Academic Press, 7th edition edition, 2007.
- H. L. Grant, R. W. Stewart, and A. Moilliet. Turbulence spectra from a tidal channel. *Journal of Fluid Mechanics*, 12:241–268, 1962.
- S. Grossmann, D. Lohse, V. L’vov, and I. Procaccia. Finite size corrections to scaling in high Reynolds number turbulence. *Physical Review Letters*, 73(3): 432–435, 1994.
- S. Grossmann, D. Lohse, and A. Reeh. Different intermittency for longitudinal and transversal turbulent fluctuations. *Physics of Fluids*, 9(12):3817–3825, 1997.
- S. N. Gurbatov, S. I. Simdyankin, E. Aurell, U. Frisch, and G. Tóth. On the decay of Burgers turbulence. *Journal of Fluid Mechanics*, 344:339–374, 1997.

- N. Guttenberg and N. Goldenfeld. Friction factor of two-dimensional rough-boundary turbulent soap film flows. *Physical Review E*, 79(065306), 2009.
- Z. Hao, T. Zhou, Y. Zhou, and J. Mi. Reynolds number dependence of the inertial range scaling of energy dissipation rate and enstrophy in a cylinder wake. *Experiments in Fluids*, 44:279–289, 2008.
- G. He, G. D. Doolen, and S. Chen. Calculations of longitudinal and transverse velocity structure functions using a vortex model of isotropic turbulence. *Physics of Fluids*, 11(12):3743–3748, 1999.
- W. Heisenberg. Zur statistischen Theorie der Turbulenz. *Zeit. f. Phys.*, 124:628–657, 1948.
- J. A. Herweijer and W. Van de Water. Transverse structure functions of turbulence. In *Advances in Turbulence V*, pages 210–216. Kluwer, 1995.
- G. Hestroni. Particles turbulence interaction. *International Journal of Multiphase Flow*, 15:735–746, 1989.
- K. Huang. *Statistical Mechanics*. John Wiley & Sons, 1987.
- W. Hwang and J. K. Eaton. Creating homogeneous and isotropic turbulence without a mean flow. *Experiments in Fluids*, 36:444–454, 2004.
- E. Inoue. On the Lagrangian correlation coefficient for the turbulent diffusion and its application to the atmospheric diffusion phenomena. Unpublished report, Geophys. Inst., Univ. of Tokyo, 1951.
- J. C. Isaza, Z. Warhaft, and L. R. Collins. Experimental investigation of the large-scale velocity statistics in homogeneous turbulent shear flow. *Physics of Fluids*, 21(065105), 2009.

- V. N. Ivanov and R. L. Stratonovich. On the Lagrange characteristics of turbulence. *Izv. Akad. Nauk. SSSR, Ser. Geofiz.*, – (10):1581–1593, 1963.
- H. Kahalerras, Y. Malecot, and Y. Gagne. Transverse velocity structure functions in developed turbulence. In *Advances in Turbulence VI*, pages 235–238, Dordrecht, 1996. Kluwer.
- H. Kahalerras, Y. Malécot, Y. Gagne, and B. Castaing. Intermittency and Reynolds number. *Physics of Fluids*, 10(4):910–921, 1998.
- Y. Kaneda, T. Ishihara, M. Yokokawa, K. Itakura, and A. Uno. Energy dissipation rate and energy spectrum in high resolution direct numerical simulations of turbulence in a periodic box. *Physics of Fluids*, 15(2):L21–L24, 2003.
- T. Kármán and L. Howarth. On the statistical theory of isotropic turbulence. *Proc. R. Soc. Lond. A*, 164:192–215, 1938.
- H. Kellay and W. I. Goldberg. Two-dimensional turbulence: a review of some recent experiments. *Rep. Prog. Phys.*, 65:845–894, 2002.
- J. Kim, P. Moin, and R. Moser. Turbulence statistics in fully developed channel flow at low Reynolds number. *Journal of Fluid Mechanics*, 177:133–166, 1987.
- A. L. Kistler and T. Vrebalovich. Grid turbulence at large Reynolds numbers. *Journal of Fluid Mechanics*, 26:37–47, 1966.
- B. Knight and L. Sirovich. Kolmogorov inertial range for inhomogeneous turbulent flows. *Physical Review Letters*, 65(11):1356–1359, 1990.
- A. N. Kolmogorov. Curves in Hilbert space which are invariant with respect to one-parameter group motion. *Dokl. Akad. Nauk. SSSR*, 26(1):6–9, 1940a.

- A. N. Kolmogorov. Wiener's spiral and some interesting curves in Hilbert space. *Dokl. Akad. Nauk. SSSR*, 26(2):115–118, 1940b.
- A. N. Kolmogorov. The local structure of turbulence in incompressible viscous fluid for very large Reynolds numbers. *Dokl. Akad. Nauk. SSSR*, 30:299–303, 1941a.
- A. N. Kolmogorov. Dissipation of energy in locally isotropic turbulence. *Dokl. Akad. Nauk. SSSR*, 32:19–21, 1941b.
- A. N. Kolmogorov. Dissipation of energy in locally isotropic turbulence. *Proc. R. Soc. Lond. A*, 434:15–17, 1991.
- R. H. Kraichnan. Isotropic turbulence and inertial-range structure. *Physics of Fluids*, 9:1728–1752, 1966.
- R. H. Kraichnan and D. Montgomery. Two-dimensional turbulence. *Rep. Prog. Phys.*, 43:547–619, 1980.
- S. Kurien and K. R. Sreenivasan. Anisotropic scaling contributions to high-order structure functions in high-Reynolds-number turbulence. *Physical Review E*, 62(2):2206–2212, 2000.
- S. Kurien, V. S. L'vov, I. Procaccia, and K. R. Sreenivasan. Scaling structure of the velocity statistics in atmospheric boundary layers. *Physical Review E*, 61(1):407–421, 2000.
- S. Kurien, M. A. Taylor, and T. Matsumoto. Cascade time scales for energy and helicity in homogeneous isotropic turbulence. *Physical Review E*, 69(6):066313, 2004.

- A. La Porta, G. A. Voth, A. M. Crawford, J. Alexander, and E. Bodenschatz. Fluid particle accelerations in fully developed turbulence. *Nature*, 409:1017–1019, 2000.
- L. D. Landau and E. M. Lifshitz. *Fluid Mechanics*. Addison-Wesley, Reading MA, 1959.
- D. H. Lenschow and B. B. Stankov. Length scales in the convective boundary layer. *Journal of the Atmospheric Sciences*, 43(12):1198–1209, 1986.
- J. Lighthill. Acoustic streaming. *Journal of Sound and Vibration*, 61(3):391–418, 1978.
- C. C. Lin. On Taylor’s hypothesis and the acceleration terms in the Navier-Stokes equations. *Quarterly of Applied Mathematics*, 10(4):295–306, 1953.
- C. C. Lin. On a theory of dispersion by continuous movements. *Proc. Natl. Acad. Sci. USA*, 46:566–570, 1960.
- E. Lindborg. Kinematics of homogeneous axisymmetric turbulence. *Journal of Fluid Mechanics*, 302:179–201, 1995.
- D. Lohse. Cross-over from high to low reynolds number turbulence. *Physical Review Letters*, 73(24):3223–3226, 1994.
- D. Lohse and A. Müller-Groeling. Bottleneck effects in turbulence-scaling phenomena in r -space versus p -space. *Physical Review Letters*, 74(10):1747–1750, 1995.
- J. Lu, J. P. Fugal, H. Nordsiek, E. W. Saw, R. A. Shaw, and W. Yang. Lagrangian particle tracking in three dimensions via single-camera in-line digital holography. *New Journal of Physics*, 10(125013), 2008.

- J. L. Lumley. *Some problems connected with the motion of small particles in turbulent fluid*. PhD thesis, The Johns Hopkins University, Baltimore, Maryland, 1957.
- J. L. Lumley. An approach to the Eulerian-Lagrangian problem. *J. Math. Phys.*, 3:309–312, 1962.
- J. L. Lumley. Similarity and the turbulent energy spectrum. *Physics of Fluids*, 10(4):855–858, 1967.
- J. L. Lumley. *Two phase and non-Newtonian flows*. In *Topics in Applied Physics: Turbulence*, volume 12, pages 290–324. Springer-Verlag, Berlin, 1976.
- J. L. Lumley and A. M. Yaglom. A Century of Turbulence. *Flow, Turbulence and Combustion*, 66:241–286, 2001.
- T. S. Lundgren. Kolmogorov turbulence by matched asymptotic expansions. *Physics of Fluids*, 15(4):1074–1081, 2003.
- V. L'vov and I. Procaccia. The universal scaling exponents of anisotropy in turbulence and their measurement. *Physics of Fluids*, 8(10):2565–2567, 1996.
- P. B. MacCready. Atmospheric turbulence measurements and analysis. *J. Meteor.*, 10(4):325–337, 1953.
- M. J. Manton. The equation of motion for a small aerosol in a continuum. *Pure and Applied Geophysics*, 115:547–559, 1977.
- D. O. Martinez, S. Chen, G. D. Doolen, R. H. Kraichnan, L. P. Wang, and Y. Zhou. Energy spectrum in the dissipation range of fluid turbulence. *Journal of Plasma Physics*, 57:195–201, 1997.
- M. R. Maxey and J. J. Riley. Equation of motion for a small rigid sphere in a nonuniform flow. *Physics of Fluids*, 26:883–889, 1983.

- W. T. J. Mayo, M. T. Shay, and S. Ritter. Digital estimation of turbulence power spectra from burst counter ldv data. In *Proceedings of 2nd International Workshop on Laser Velocimetry*, pages 16–26, Purdue University, 1974.
- T. J. McDougall. Bias correction for individual realisation of lda measurements. *Journal of Physics E: Scientific Instruments*, 13:53–60, 1980.
- D. K. McLaughlin and W. G. Tiederman. Biasing correction for individual realisation of laser anemometer measurements in turbulent flows. *Physics of Fluids*, 15:2082–2088, 1973.
- R. Mei. Velocity fidelity of flow tracer particles. *Experiments in Fluids*, 22:1–13, 1996.
- P. D. Mininni, A. Alexakis, and A. Pouquet. Nonlocal interactions in hydrodynamic turbulence at high Reynolds numbers: the slow emergence of scaling laws. *Physical Review E*, 77:036306, 2008.
- A. S. Monin and A. M. Yaglom. *Statistical Fluid Mechanics*, volume 2. MIT Press, Cambridge MA, USA, 1975.
- R. D. Moser. Kolmogorov inertial range spectra for inhomogeneous turbulence. *Physics of Fluids*, 6(2):794–801, 1994.
- L. Mydlarski and Z. Warhaft. Passive scalar statistics in high-Péclet-number grid turbulence. *Journal of Fluid Mechanics*, 358:135–175, 1998.
- M. Nelkin. In What Sense Is Turbulence an Unsolved Problem? *Science*, 255: 566–570, 1992.
- M. Nelkin. Universality and scaling in fully developed turbulence. *Advances in Physics*, 43(2):143–181, 1994.

- A. Noullez, G. Wallace, W. Lempert, R. B. Miles, and U. Frisch. Transverse velocity increments in turbulent flow using the RELIEF technique. *Journal of Fluid Mechanics*, 339:287–307, 1997.
- E. A. Novikov. Random force method in turbulence theory. *Sov. Phys., J. Exp. Theor. Phys.*, 17:1449–1454, 1963.
- A. M. Obukhov. On the distribution of energy in the spectrum of turbulent flow. *Dokl. Akad. Nauk. SSSR*, 32(1):22–24, 1941a.
- A. M. Obukhov. Spectral energy distribution in a turbulent flow. *Izv. Akad. Nauk. SSSR, Ser. Geogr. Geofiz.*, 5(4-5):453–466, 1941b.
- A. M. Obukhov. On the theory of atmospheric turbulence. *Izv. Akad. Nauk. SSSR, Ser. Fiz.*, 6(1-2):59–63, 1942.
- A. M. Obukhov. Local structure of atmospheric turbulence. *Dokl. Akad. Nauk. SSSR*, 67(4):643–646, 1949a.
- A. M. Obukhov. Structure of the temperature field in turbulent flows. *Izv. Akad. Nauk. SSSR, Ser. Geogr. Geofiz.*, 13:58–69, 1949b.
- L. Onsager. Statistical hydrodynamics. *Nuovo Cimento*, 6(2):279–287, 1949.
- S. Ott and J. Mann. An experimental investigation of the relative diffusion of particle pairs in three-dimensional turbulent flow. *Journal of Fluid Mechanics*, 422:207–223, 2000.
- N. T. Ouellette. *Probing the statistical structure of turbulence with measurements of tracer particle tracks*. PhD thesis, Cornell University, Ithaca, New York, 2006.
- N. T. Ouellette, H. Xu, M. Bourgoin, and E. Bodenschatz. Experimental study of turbulent relative dispersion models. *New Journal of Physics*, 8(109), 2006.

- D. M. Paul and D. A. Jackson. Rapid velocity sensor using astatic confocal fabry-perot interferometer and a single argon laser. *Journal of Physics E: Scientific Instruments*, 4:170–172, 1971.
- B. R. Pearson and R. A. Antonia. Reynolds-number dependence of turbulent velocity and pressure increments. *Journal of Fluid Mechanics*, 444:343–382, 2001.
- B. R. Pearson, P. Å. Krogstad, and W. Van de Water. Measurements of the turbulent energy dissipation. *Physics of Fluids*, 14(3):1288–1290, 2002.
- D. Poggi, G. G. Katul, and M. Cassiani. On the anomalous behavior fo the Lagrangian structure function similarity constant inside dense canopies. *Atmospheric Environment*, 42(4212-4231), 2008.
- S. B. Pope. *Turbulent Flows*. Cambridge University Press, Cambridge, U. K., 2000.
- L. Prandtl. Über die Rolle der Zähigkeit im Mechanismus der ausgebildete Turbulenz. GOAR 3712, DLR Archive, 1945.
- A. Praskovsky and S. Oncley. Measurements of the Kolmogorov constant and intermittency exponent at very high Reynolds numbers. *Physics of Fluids*, 6(9):2886–2888, 1994.
- W. H. Press, S. A. Teukolsky, W. T. Vetterling, and B. P. Flannery. *Numerical Recipes*. Cambridge University Press, Cambridge, U. K., 2007.
- J. Qian. Universal equilibrium range of turbulence. *Physics of Fluids*, 27:2229–2233, 1984.
- M. Raffel, C. E. Willert, S. T. Wereley, and J. Kompenhans. *Particle Image Velocimetry*. Springer-Verlag, 2nd edition, 2007.

- L. F. Richardson. *Weather Prediction by Numerical Process*. Cambridge University Press, Cambridge, U. K., 1922.
- L. F. Richardson. Atmospheric diffusion shown on a distance-neighbour graph. *Proc. R. Soc. Lond. A*, 110:709–737, 1926.
- P. E. Roach. The generation of nearly isotropic turbulence by means of grids. *International Journal of Heat and Fluid Flow*, 8:82–92, 1987.
- H. P. Robertson. The invariant theory of isotropic turbulence. *Proc. Camb. Phil. Soc.*, 36:209–223, 1940.
- H. C. Rodean. The universal constant for the Lagrangian structure function. *Physics of Fluids A*, 3(6):1479–1480, 1991.
- G. P. Romano and R. A. Antonia. Longitudinal and transverse structure functions in a turbulent round jet: effect of initial conditions and Reynolds number. *Journal of Fluid Mechanics*, 436:231–248, 2001.
- M. Roth. Review of atmospheric turbulence over cities. *Q. J. R. Meteorol. Soc.*, 126:941–990, 2000.
- S. G. Saddoughi and S. V. Veeravalli. Local isotropy in turbulent boundary layers at high Reynolds number. *J. Fluid Mech.*, 268:333–372, 1994.
- P. L. C. Salazar and L. R. Collins. Two-particle dispersion in isotropic turbulent flows. *Annu. Rev. Fluid Mech.*, 41:405–432, 2009.
- B. L. Sawford. Reynolds number effects in Lagrangian stochastic models of turbulent dispersion. *Physics of Fluids A*, 3(6):1577–1586, 1991.
- Z. S. She and E. Leveque. Universal scaling laws in fully developed turbulence. *Physical Review Letters*, 72:336–339, 1994.

- X. Shen and Z. Warhaft. The anisotropy of the small scale structure in high Reynolds number ($R_\lambda \sim 1000$) turbulent shear flow. *Physics of Fluids*, 12(11): 2976–2989, 2000.
- X. Shen and Z. Warhaft. Longitudinal and transverse structure functions in sheared and unsheared wind-tunnel turbulence. *Physics of Fluids*, 14(1):370–381, 2002.
- M. Shiotani. On the fluctuation of the temperature and turbulent structure near the ground. *J. Meteor. Soc. Japan*, 33(3):117–123, 1955.
- S. S. Shy, C. Y. Tang, and S. Y. Fann. A nearly isotropic turbulence generated by a pair of vibrating grids. *Experimental Thermal and Fluid Science*, 14:251–262, 1997.
- H. Siebert, R. A. Shaw, and Z. Warhaft. Statistics of small-scale velocity fluctuations and internal intermittency in marine stratocumulus clouds. *Journal of the Atmospheric Sciences*, 67:262–273, 2010.
- K. R. Sreenivasan. On the scaling of the turbulence energy dissipation rate. *Physics of Fluids*, 27(5):1048–1051, 1984.
- K. R. Sreenivasan. On the universality of the Kolmogorov constant. *Physics of Fluids*, 7:2778–2784, 1995.
- K. R. Sreenivasan. The passive scalar spectrum and the Obukhov-Corrsin constant. *Physics of Fluids*, 8(1):189–196, 1996.
- K. R. Sreenivasan and B. Dhruva. Is there scaling in high-Reynolds-number turbulence? *Progress of Theoretical Physics Supplement*, -(130):103–120, 1998.

- K. R. Sreenivasan and R. Narasimha. Rapid distortion of axisymmetric turbulence. *Journal of Fluid Mechanics*, 84:497–516, 1978.
- K. R. Sreenivasan, S. I. Vainshtein, R. Bhiladvala, I. San Gil, S. Chen, and N. Cao. Asymmetry of velocity increments in fully developed turbulence and the scaling of low-order moments. *Physical Review Letters*, 77(8):1488–1491, 1996.
- A. Staicu and W. Van de Water. Small scale velocity jumps in shear turbulence. *Physical Review Letters*, 90(094501):1–4, 2003.
- A. Staicu, B. Vorselaars, and W. Van der Water. Turbulence anisotropy and the SO(3) description. *Physical Review E*, 68:046303, 2003.
- S. Stolovitzky and K. R. Sreenivasan. Scaling of structure functions. *Physical Review E*, 48:R33–R36, 1993.
- R. Sullivan, R. Greeley, M. Kraft, G. Wilson, M. Golombek, K. Herkenhoff, J. Murphy, and P. Smith. Results of the Imager for Mars Pathfinder windssock experiment. *Journal of Geophysical Research*, 105(E10):24547–24562, 2000.
- G. I. Taylor. Statistical theory of turbulence. *Proc. R. Soc. Lond. A*, 151:421–478, 1935.
- G. I. Taylor. The spectrum of turbulence. *Proc. R. Soc. Lond. A*, 164(919):476–490, 1938.
- R. J. Taylor. Some observations of wind velocity autocorrelations in the lowest layers of the atmosphere. *Austr. J. Phys.*, 8(4):535–544, 1955.
- D. J. Thomson. The second-order moment structure of dispersing plumes and puffs. *Journal of Fluid Mechanics*, 320:305–329, 1996.

- F. Toschi and E. Bodenschatz. Lagrangian properties of particles in turbulence. *Annu. Rev. Fluid Mech.*, 41:375–404, 2009.
- A. A. Townsend. Experimental evidence for the theory of local isotropy. *Proc. Camb. Phil. Soc.*, 44(4):560–565, 1948.
- T. Tran, P. Chakraborty, N. Guttenberg, A. Prescott, H. Kellay, W. Goldburg, N. Goldenfeld, and G. Gioia. Macroscopic effects of the spectral structure in turbulent flows. *Nature Physics*, 6:438–441, 2010.
- S. I. Vainshtein, K. R. Sreenivasan, R. T. Pierrehumbert, V. Kashyap, and A. Juneja. Scaling exponents for turbulence and other random processes and their relationships with multifractal structure. *Physical Review E*, 50(3):1823–1835, 1994.
- C. W. Van Atta and W. Y. Chen. Structure functions of turbulence in the atmospheric boundary layer over the ocean. *Journal of Fluid Mechanics*, 44(1):145–159, 1970.
- W. Van de Water and J. A. Herweijer. High-order structure functions of turbulence. *Journal of Fluid Mechanics*, 387:3–37, 1999.
- G. J. Van Fossen and C. Y. Ching. Measurements of the influence of integral length scale on stagnation region heat transfer. Technical Memorandum 106503, NASA, 1994.
- G. J. Van Fossen, R. J. Simoneau, and C. Y. Ching. Influence of turbulence parameters, Reynolds number, and body shape on stagnation-region heat transfer. Technical Paper 3487, NASA, 1994.

- G. J. Van Fossen, R. J. Simoneau, and C. Y. Ching. Influence of turbulence parameters, Reynolds number, and body shape on stagnation-region heat transfer. *Journal of Heat Transfer*, 117:597–603, 1995.
- M. K. Verma and D. Donzis. Energy transfer and bottleneck effect in turbulence. *J. Phys. A*, 40(16):4401–4412, 2007.
- G. A. Voth, A. La Porta, A. M. Crawford, J. Alexander, and E. Bodenschatz. Measurement of particle accelerations in fully developed turbulence. *Journal of Fluid Mechanics*, 469:121–160, 2002.
- Z. Warhaft. Turbulence in nature and in the laboratory. *Proceedings of the National Academy of Science*, 99(1):2481–2486, 2002.
- Z. Warhaft and X. Shen. On the higher order mixed structure functions in laboratory shear flow. *Physics of Fluids*, 14(7):2432–2438, 2002.
- T. A. Warnaars, M. Hondzo, and M. A. Carper. A desktop apparatus for studying interactions between microorganisms and small-scale fluid motion. *Hydrobiologia*, 563:431–443, 2006.
- D. R. Webster, A. Brathwaite, and J. Yen. A novel laboratory apparatus for simulating isotropic oceanic turbulence at low reynolds number. *Limnology and Oceanography: Methods*, 2:1–12, 2004.
- K. A. Weinman and A. Y. Klimenko. Estimation of the Kolmogorov constant C_0 by direct numerical simulation of a continuous scalar. *Physics of Fluids*, 12(12):3205–3220, 2000.
- C. F. v. Weizsäcker. Das Spektrum der Turbulenz bei großen Reynoldschen Zahlen. *Zeit. f. Phys.*, 124:614–627, 1948.

- G. S. Welter, A. R. Wittwer, G. A. Degrazia, O. C. Acevedo, O. L. Leal de Moraes, and D. Anfossi. Measurements of the Kolmogorov constant from laboratory and geophysical wind data. *Physica A*, 388(18):3745–3751, 2009.
- H. Xia, D. Byrne, G. Falkovich, and M. Shats. Upscale energy transfer in thick turbulent fluid layers. *Nature Physics*, 7:321–324, 2011.
- V. Yakhot and V. Zakharov. Hidden conservation-laws in hydrodynamics energy and dissipation rate fluctuation spectra in strong turbulence. *Physica D*, 64(4):379–394, 1993.
- P. K. Yeung and J. G. Brasseur. The response of isotropic turbulence to isotropic and anisotropic forcing at the large scales. *Physics of Fluids A*, 3:884–897, 1991.
- P. K. Yeung and Y. Zhou. Universality of the Kolmogorov constant in numerical simulations of turbulence. *Physical Review E*, 56:1746–1752, 1997.
- M. V. Zagarola and A. J. Smits. Mean-flow scaling of turbulent pipe flow. *Journal of Fluid Mechanics*, 373:33–79, 1998.
- T. Zhou and R. A. Antonia. Reynolds number dependence of the small-scale structure of grid turbulence. *Journal of Fluid Mechanics*, 406:81–107, 2000.
- T. Zhou, B. R. Pearson, and R. A. Antonia. Comparison between temporal and spatial transverse velocity increments in a turbulent plane jet. *Fluid Dynamics Research*, 28:127–138, 2001.
- T. Zhou, Z. Hao, L. P. Chua, and S. C. M. Yu. Scaling of longitudinal and transverse velocity increments in a cylinder wake. *Physical Review E*, 71:066307, 2005.

R. Zimmermann, H. Xu, Y. Gasteuil, M. Bourgoïn, R. Volk, J.-F. Pinton, and E. Bodenschatz. The lagrangian exploration module: An apparatus for the study of statistically homogeneous and isotropic turbulence. *Review of Scientific Instruments*, 81(055112), 2010.